AB 4348

Interaction of Ultrashort Intense Laser Pulses with Metallic Surfaces

Nektarios A. Papadogiannis

Institute of Electronic Structure & Laser, Foundation For Research and Technology-Hellas
Department of Physics, University of Crete

(August 1996)

ND: 7425

Interaction of Ultrashort Intense Laser Pulses with Metallic Surfaces

Nektarios A. Papadogiannis

Submitted to
the Graduate School of Physics Department
of the University of Crete
for the Requirements of the Degree
Doctor of Philosophy
(Physics)

Institute of Electronic Structure & Laser, Foundation For Research and Technology-Hellas
Department of Physics, University of Crete

(August 1996)

"Κι αν πτωχική την βρεις η Ιθάκη δεν σε γέλασε.
Έτσι σοφός που έγινες με τόση πείρα,
ήδη θα κατάλαβες Ιθάκες τι σημαίνουν.

Η Ιθάκη σ'έδωσε τ'ωραίο ταξίδι.
Χωρίς αυτήν δεν θάβγαινες στον δρόμο.
Άλλα δεν έχει να σε δώσει πιά."

Καβάφης

Contents

Abstract

Interaction of Ultrashort Intense Laser Pulses with Metallic Surfaces

(Ph.D Thesis)

Nektarios A. Papadogiannis

Institute of Electronic Structure & Laser, Foundation For Research and Technology-Hellas.
Department of Physics, University of Crete.

(1992-1996)

The objective of this thesis is to study the interaction of ultrafast and strong laser pulses with metallic surfaces. Mainly three processes take place in the above interaction. The first one is the single- or multi-photon photoelectron emission. The second is the multiple harmonic generation and the third is the non-radiative relaxation processes of the electrons excited by the laser pulse. Initially, the first two phenomena are studied separately and then their interplay with the third one is studied in various metals.

Principally, the tested metal was gold because of its oxygen free surface even in atmospheric conditions. Also, gold can be described reasonably well by the Sommerfeld model, which is used in most of the theories in the field. Other tested metals were copper, tungsten, aluminium and iron.

Various pulsed laser types are used in order to excite the electrons of the metallic surface. Their characteristics are; a fast KrF excimer system at 248 nm with 450 femtoseconds pulse duration, a fast excimer pumped dye system at 496 nm with 450 femtosecond pulse duration, for a mode-locked Nd-YAG laser at 1064 nm with 35 picoseconds pulse duration, a mode-locked Nd-Glass laser at 1050 nm with 2 picoseconds pulse duration, a fast Ti:sapphire solid state laser system at 800 nm with 100 femtoseconds pulse duration and a KrF excimer laser at 248 nm and 17 nanosecond pulse duration. The reason for the use of various laser pulses is that each laser pulse gives optimal conditions to study certain phenomena occurred by its interaction with the metallic surface,i.e., the wavelength defines the order of multiphoton effect, the pulse duration is responsible for the kind of interaction between the laser electric field and the metallic surface. Other critical parameters is the polarization and the intensity of the laser beam. The laser intensities per pulse are of the order of 10^7-10^{11} W/cm^2. The upper limit depends on the critical intensity for plasma creation in various metallic surfaces. In any case, the laser intensity is kept below the plasma creation threshold. This is checked by time resolved autocorrelation measurements of the photoelectrons.

In the case of photoelectron emission experiments, the laser polarization phenomena, the efficiency of the phenomenon comparing the various orders of multiphoton photoemission, and also the best conditions to extract high density electron beams without destroying the metallic surface by plasma creation, are reported. The electron photoemission data are compared with the outcome of several theories. It is deduced that only theories that take in account the electron relaxation phenomena can explain the experimental observations.

The observation of multiple harmonic generation from the metallic surfaces has also been investigated. Studies of laser beam polarization effects, harmonic tunability and finally spatial coherence effects between the laser pulses and the electrons on the metallic surface clarifies the way of production of multiple harmonic generation and suggest the optimal conditions in order to achieve higher efficiency. A method for measuring the pulse duration of subpicosecond laser pulses as well as the asymmetry and the phase variations is proposed, using the second and third harmonic generation produced on the metallic surface. The experimental results are in satisfactory agreement with some quantum mechanical theories and especially in the case of second harmonic generation experiments, the results agree well even with early semiclassical theories. In the study of harmonic generation spectroscopy an influence of the interband transitions on harmonic generation is found when the fundamental absorbed photon is able to induce transitions from the top of the d-band of noble metals to the Fermi-level.

The electron-phonon energy and collision relaxation time are studied in the range of high laser intensities but always below the plasma creation threshold. An extra non-linearity even at single-photon electron photoemission is observed. This non-linearity is attributed to the thermal non-equilibrium between the electrons and the lattice produced by sub-picosecond laser pulses in the metallic surface, and is related to the dynamics of energy relaxation between the electron and the lattice. Also, a time resolved autocorrelation technique is proposed for the direct measurements of electron relaxation time by single-photon electron emission processes. In order to explain the experimental data and to evaluate the electron-phonon scattering time for various metals a phenomenological model is proposed based on Anisimov's coupled thermal equations and Fowler-DuBridge theory. The case of non-thermal electrons is discussed. Similar extra non-linear phenomena are observed in second harmonic generation from an Au surface, using intensity dependence measurements, time-resolved autocorrelation measurements and energy resolved measurements. A simple theory based on the Pauli's law can explain the magnitude of the mentioned thermally assisted extra non-linearities. A comparison between the physics of the thermal non-linearities on harmonic generation with that in the electron photoemission is made.

To my wife Ioanna and my parents Andrea and Katerini

Acknowledgements

I would like to thank my supervisor **Professor Costas Fotakis**, for allowing me join the laser laboratory at FORTH, for his guidance, financial and moral support during all the period that I was working for my PhD thesis. I should also thank him for his critical reading this manuscript.

I am grateful to my advisor **Dr. Stavros Moustaizis**, for his constant advisory, guidance and support on the experiments. He has contributed to several ideas presented in this thesis and he introduced me with patience and kindness to the experimental techniques I used. I also thank him for help me with editing.

I would like to thank **Professor Anastasios Georges** for his theoretical advisory in the area of multi-photon phenomena and for many valuable discussions on his theoretical calculations. I must thank him for critical reading of my thesis and for correcting my English in the text. I also acknowledge his hospitality during my visit at the University of Patras in April 1995.

I am deeply indebted to **Professor Jean-Pierre Girardeau-Montaut** for many valuable discussions and advice in the area of electron photoemission and thermal phenomena. I also thank him for his useful suggestions, for carefully reading this manuscript and for his valuable comments on it. I grateful acknowledge his hospitality during my visit at the University Bernard Lyon I in France in the Winter of 1994-1995.

I am grateful to the other three members of my examination committee **Professors Peter Lambropoulos**, **Dimitri Charalambidis** and **Panos Tzanetakis** for their useful comments on my thesis and useful discussions. I also thank them for teaching me fundamental principles related to the physics area I worked, following the courses that they offer in the University of Crete.

I grateful acknowledge **Professor Gyozo Farkas** and **Dr. Csaba Toth** for the experience that I got working with them for the harmonic generation experiments either in Crete

(FORTH) or in Budapest (KFKI). I should thank them for their kindness and hospitality during my visit at KFKI in Budapest in the April of 1992.

I am grateful to the Physics Department of the University of Crete and to the Institute of Electronic Structure and Laser at FORTH for financial support during my studies there.

Many thanks go to **Dr. Costas Kalpouzos** for critical reading some parts of my text and for fruitful discussions and to **Dr. Antonios Adriotis** for useful discussions on relaxation phenomena. **Mr. Apostolos Englezis** should be thanked for his expert technical assistance during most of the experiments sometimes even weekends. I would like to thank my friends **Dr. Georgios Kavoulakis, Mr. Panagiotis Loukakos and Ms. Kiki Chrysopoulou** for helping me with editing, for useful discussions and one of them (P.L.) for his valuable help in the experiments that I performed during the last year.

I am grateful to technical staff, the secretaries, the researchers, the students of the Laser lab at FORTH/IESL and the postgraduate students of the Physics Department for their kindness and support.

I express my deep feelings to my wife **Ioanna** and our parents **Andrea** and **Katerini** for their love, patience and support during all these difficult years that I prepared my thesis. I dedicate this book to them.

Last but not least, I thank God for His guidance in my life.

List of Figures

List of Tables

Chapter 1

Introduction

1.1 General Considerations

Since a reasonable elementary model for a metal is that of an isotropic free electron gas, which is a highly linear system when excited by electromagnetic waves, the non-linear mechanisms are very weak. Thus, experimental investigations require very high optical power laser sources and are performed very close to the damage threshold of the metal surfaces. The damage takes place when the lattice temperature exceeds the melting point of the metal. The only way to apply very intense electromagnetic fields on a metallic surface, without destroying it, is to use ultrashort laser pulses. When the laser pulse is shorter than the electron-phonon energy relaxation time, the electrons are rapidly thermalized in a high temperature Fermi-Dirac distribution but the lattice remains at a low temperature due to high specific heat [Ani74, Kag57]. After a few picoseconds (or faster), electron relaxation occurs in the lattice [Fuj84, Els87, Sch87, Bro87, Els91, Gir95].

Multi-photon phenomena were first observed in atoms. Multi-photon processes may take place when an intense laser beam interacts with an atom and ionization may occur as a result of multiphoton absorption, which is termed as multiphoton ionization [Vor66, Ago68, Lam72, Ebe78, Lam84, Lam87]. Also, a high number of odd harmonics up to as high as 135 [Hui93], have been observed. The harmonics have a wide plateau region, terminated with a sharp cutoff.

One of the aims of this work is to examine if these phenomena have analogues in solid surfaces characterized by the rectangular-well model potential. Above all, the experiments try to clarify the main parameters that a theory has to take in account in order to explain the observations. Another main parameter is to gain insight into the dynamics of the electronic non-radiative decay processes, which are the main processes after the act of an intense laser beam on a metallic surface. The experimental study of electron relaxation phenomena plays a main role in the understanding of multiphoton phenomena from metallic surfaces.

Therefore, it seemed reasonable to perform experiments for the potential analogy between the multiple harmonic generation and multi-photon electron emission in gas atoms and metallic surfaces.

1.2 Metals

The penetration depth of a laser beam in a metal, is of the order of few 10 nm for the wavelength range of the lasers used in our experiments. In fact, the thickness of a metallic surface that participates in the above mentioned phenomena is of the order of a few 10 nm.

Both harmonic generation and electron photoemission, as shown in the next chapters, have a strong p-polarization dependence, i.e., the yield of each phenomenon is much higher in the case that the electric field of the lasers are perpendicular to the metal surface. This observation proves that only the electrons which are very close to the surface contribute to the effects. The reason is that the surface electrons are free to move in the plane of the surface, but in the direction perpendicular to the surface they are bound by the surface potential, and the work function corresponds to the ionization energy.

In the Sommerfeld theory, a metal is described quantum mechanically by a step potential model as shown in Fig 1.1. The electrons are free to move in the left part of the step potential. The electronic energy states can be calculated quantum mechanically [Ash76]. Pauli exclusion principle requires a Fermi-Dirac distribution for the electrons. The electron occupation probability of a state with energy E is given by the expression:

$$f(E) = \frac{1}{e^{(E-E_F)/k_B T} + 1} \tag{1.1}$$

where E_F is the Fermi energy of the metal, k_B is the Boltsmann constant and T is the electrons temperature. The Fermi energy is written in the form:

$$E_F = \frac{e^2 a_o}{2}(3\pi^2 n_V)^{2/3} \tag{1.2}$$

where a_o is Bohr radius ($= 0.529 \times 10^{-10}$ m) and n_V is the electronic density. The above equation predicts a range of Fermi energies, for the densities of metallic elements, between 1.5 and 15 eV [Ash76].

The thick metal can be described by the one-dimensional step potential. This dimension is the one perpendicular to the surface, because in the plain of the metal surface the electrons are free particles and can not absorb any photons.

If z is the axis perpendicular to the metal surface which lies at z=0, the one-dimensional potential step is $V(z) = -V_o$ for $z < 0$ and $V(z) = 0$ for $z > 0$. Solving the unperturbated Schrondinger equation:

$$[-\frac{p^2}{2m} + V(z)]\phi(z) = E\phi(z) \tag{1.3}$$

the unperturbed energy eigenstates are:

$$\phi(z) = \frac{1}{\sqrt{L_z}}\{ \begin{array}{ll} e^{ik_z z} + re^{-ik_z z} & \text{if } z < 0 \\ (1+r)e^{iq_z z} & \text{if } z > 0 \end{array} \tag{1.4}$$

where L_z is the normalization length and $k_z, q_z = (k_z^2 - 2mV_o/h^2)^{1/2}$ are the z component of the electron wavevector inside and outside the metal, respectively. The parameter r is the reflection coefficient and by taking in account the continuation of the wavefunctions and its derivatives at $z = 0$, r is equal with $(k_z - q_z)/(k_z + q_z)$.

The previous analysis is valid for the electrons located in the vicinity of Fermi energy; the conduction electrons. In fact, an electron in a crystal moves due to periodic charge distribution of the ion cores situated at the lattice sites, plus the contribution from the other electrons of the crystal. In a one-dimension model the periodic potential of the ions may be represented by an infinite set of rectangular potential wells. Thus, the potential energy in the Schrondinger equation, $V(x)$, has the periodicity of the lattice. Then the solution of the Schrondinger equation is known as Bloch function and it can be shown that:

$$\psi(x) = e^{ikx}u(x) \tag{1.5}$$

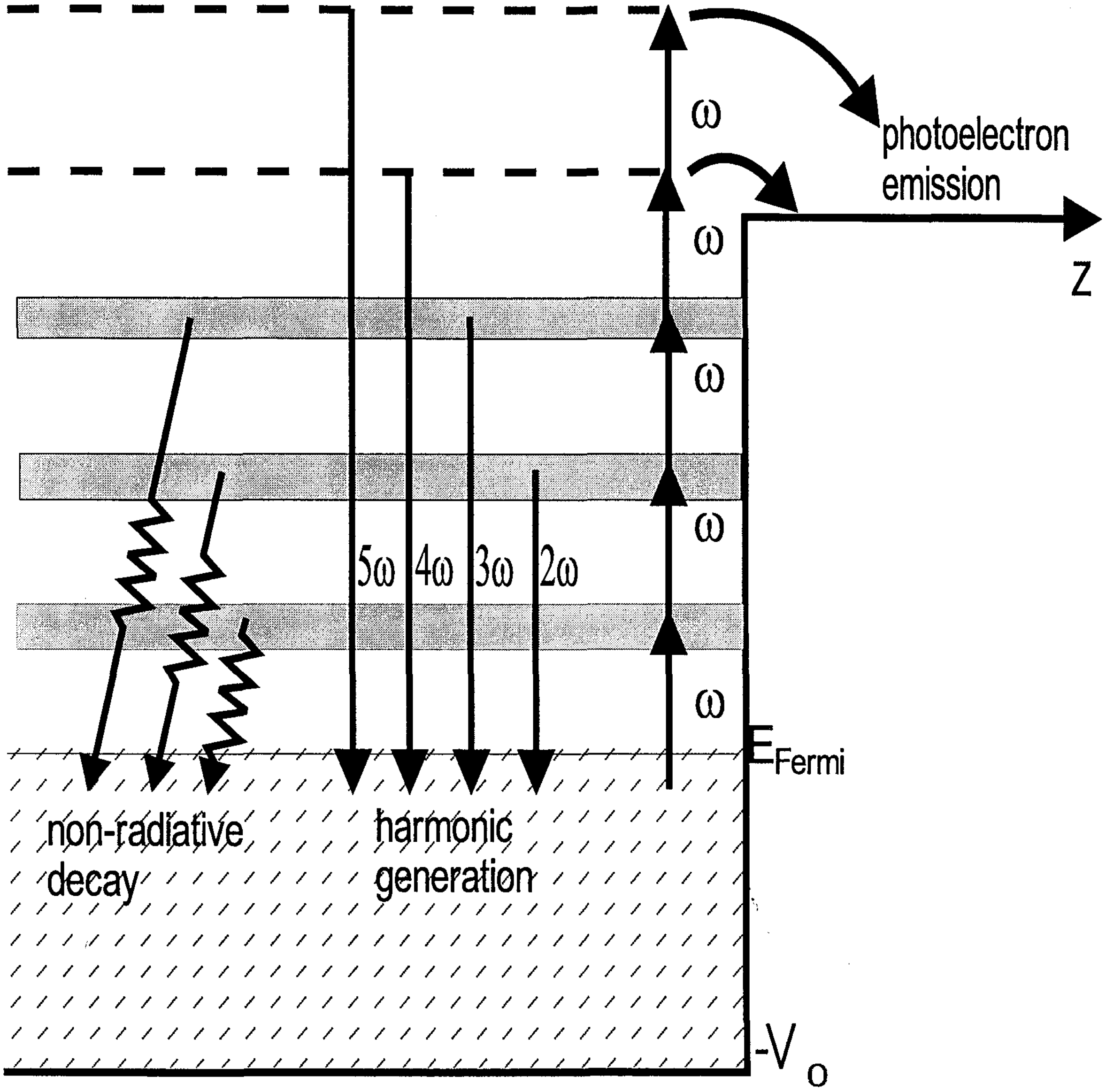

Figure 1.1: The electrons on a metallic surface are attracted by the bulk positive ions and the potential of this attraction can be described by a step potential. When an external electromagnetic field excites the electrons of the metal three phenomena may occur; Multiphoton absorption, harmonic generation and non-radiative energy decay by electron-electron and electron-phonon scattering. In the above feature the external fields are assumed to be unable to change the profile of the surface potential -perturbation region- but at the same time are intense enough to produce multiphoton phenomena.

where the function $u(x)$ has also the lattice periodicity. Let us put the zero of x-axis in the left side of a certain potential well and at $x = -b$ is the right side of the previous well and at $x = a$ the right side of the next and so on. Now, two wave equations must be solved, one for the region where the potential is zero, $0 < x < b$, and another one where the potential is V_o, $b < x < a + b$:

$$\frac{\partial^2 \psi(x)}{\partial x^2} + \frac{2m}{\hbar^2} E\psi(x) = 0 \quad \text{for } 0 < x < a \tag{1.6}$$

$$\frac{\partial^2 \psi(x)}{\partial x^2} + \frac{2m(E - V(x))}{\hbar^2} \psi(x) = 0 \quad \text{for } -b < x < 0 \tag{1.7}$$

Imposing the Bloch functions as solutions-type to the above equation we have:

$$\frac{\partial^2 u}{\partial x^2} + 2ik\frac{\partial u}{\partial x} + (s^2 - k^2)u = 0 \quad \text{for } 0 < x < a \tag{1.8}$$

$$\frac{\partial^2 u}{\partial x^2} + 2ik\frac{\partial u}{\partial x} - (q^2 + k^2)u = 0 \quad \text{for } -b < x < 0 \tag{1.9}$$

where $s^2 = \frac{2mE}{\hbar^2}$ and $q^2 = \frac{2m(E-V_o)}{\hbar^2}$

The general solutions of the above equations are:

$$u_1(x) = Ce^{i(s-k)x} + De^{-i(s+k)x} \quad \text{for } 0 < x < a \tag{1.10}$$

$$u_2(x) = Pe^{i(q-k)x} + Le^{-i(q-k)x} \quad \text{for } -b < x < 0 \tag{1.11}$$

The values of constants C, D, P and L can be calculated by the boundary conditions;

$$u_1(0) = u_2(0) \tag{1.12}$$

$$u_1(a) = u_2(-b) \tag{1.13}$$

$$(\frac{\partial u_1}{\partial x})_{x=0} = (\frac{\partial u_2}{\partial x})_{x=0} \tag{1.14}$$

$$(\frac{\partial u_1}{\partial x})_{x=a} = (\frac{\partial u_2}{\partial x})_{x=-b} \tag{1.15}$$

and the algebraic equations for C, D, P and L are:

$$C + D = P + L \tag{1.16}$$

$$i(s-k)C - i(s+k)D = i(q-k)P - i(q+k)L \tag{1.17}$$

$$Ce^{i(s-k)a} + De^{-i(s-k)a} = Pe^{-i(q-k)b} + Le^{i(q+k)b} \tag{1.18}$$

$$\begin{aligned} Ci(s-k)e^{i(s-k)a} - Di(s-k)e^{-i(s+k)a} = \\ Pi(q-k)e^{-i(q-k)b} - Li(q+k)e^{(q+k)b} \end{aligned} \tag{1.19}$$

The above equations have non-zero solution if :

$$cosas\ cosqb - \frac{s^2+q^2}{2qs} sinsa\ sinbq = cosk(a+b) \tag{1.20}$$

The latter equation gives real solutions for the parameters s and q only if the left hand side takes values in the range ±1. Consequently, we conclude that one electron model implies allowed bands of energy corresponding to the real solutions separated by forbidden bands of energy corresponding to imaginary solutions.

Since, we know the values where the discontinuities occur in the energy spectrum, we can calculate the corresponding values of k to be $k_n = l\pi/a$ (for b=0), where l=0,1,2.... The range of allowed energies are called Brillouin zones and l=1,2,3... defines the limit of the zones.

The band theory is the basis of the distinction between metallic conductors, semiconductors and insulators. In the case of insulators, all the lower bands are full, the first empty band being separated by a relatively large band gap ($E_{gap} >> k_B T$, $T \approx 300$ K) from the upper empty one. In the case of semi-conductors, thermal excitation of electrons across the band gap occurs, leaving a few empty states in the lower band and a few filled states at the bottom of the almost empty band. In the case of metals having a partially filled upper band (conduction band), all the states are filled to within a few $k_B T$ of the Fermi level. For some cases a crystal has metallic behavior due to overlapping of the two upper bands, one with few empty states and another one with few filled states.

In most of the works presented in this thesis the free electron Sommerfeld model is valid. In the case that the band theory is taken into account, this will be noted clearly.

Even the conduction electrons of a metal are not completely free particles. The electrons interact predominantly with the phonons (lattice vibrations) and in special situations with other electrons.

1.2.1 Electron-Phonon Interaction

The number of photons in any normal mode is given by the Bose statistics and it is expressed by the equation:

$$n_q = \frac{1}{e^{(E_{phon}/k_B T_L)} - 1} \tag{1.21}$$

where E_{phon} is the energy of the phonons and T_L is the lattice temperature. In the electron-phonon interaction creation or destruction of one phonon may occur. Assuming a constant density of states, the electron phonon scattering time depends on the total probability for a phonon scattering event. The phonon creation probability is proportional to n_q+1 and the destruction one is proportional to n_q [Spi72]. Since n_q is temperature dependent, the electron-photon relaxation rate depends on the lattice temperature [Ash76a, Har80].

In the limit, where the lattice temperature is higher than the Debye temperature, T_D, n_q in Eq. (1.21) is equal to $k_b T/E_{phon}$. This happens because T_D is the respective temperature of the most energetic phonons. In this situation, the electron-phonon relaxation collision time, τ_{e-ph}, i.e., the time between two scatterings of an electron by phonons, is inversely proportional to the lattice temperature. Note that, in each electron- phonon scattering, only a few percent of the electron energy is transferred for the phonon creation, which, typically, have energy several meV. Thus, an electron with an energy of a few eV, above the Fermi level, requires more than one thousand scatterings in order to transfer its energy to the lattice. The statistical average time, which an excited part of the electron gas above the E_F requires to relax giving its energy to the lattice is the electron-phonon energy relaxation time. The energy relaxation is one or two (or more) orders of magnitude longer than the electron-phonon scattering time.

1.2.2 Electron-Electron Interaction

According to the Fermi liquid theory, i.e., consequences of the exclusion principle on electron-electron scattering near the Fermi energy, an electron can not be scattered by another electron, if the first one is less or equal to the Fermi-energy [Ash76c]. Suppose, for example, that the N-electron state consists of a filled Fermi-sphere (T_e = 0), plus an excited electron of energy E_1 slightly higher than E_F. In order for this electron to be scattered, it must interact with another electron of energy E_2. In our case, E_2 is less than E_F, since only the states with energy lower than E_F are occupied. The Pauli exclusion principle requires that the two electrons must scatter into unoccupied levels, effectively greater than E_F. Thus, $E_1 > E_F$, $E_2 < E_F$, $E_{3,4} > E_F$. Additionally, energy conservation requires: $E_1 + E_2 = E_3 + E_4$.

The above conditions are not satisfied together, except in the limited case where $E_1 = E_2 = E_3 = E_4 = E_F$. Thus, the allowed wave vectors for electrons 2,3,4 occupy a region of k-space of zero volume,(i.e., the Fermi surface), and therefore give a vanishingly small contribution to the cross-section of the process. Consequently, the lifetime of an electron at the Fermi-surface at T =0 is infinite.

In the case where E_1 is larger than E_F, the available phase-space for the scattering process is a shell of thickness of order $(E_1 - E_F)$. This leads to a scattering rate of order $(E_1 - E_F)^2$. The quantity appears squared rather than cubed, because once E_2 and E_3 have been chosen within the shell of allowed energies, energy conservation allows no further choice for E_4. In fact, in our experiments the electron Fermi-Dirac temperature has a minimum value equal to the room one, i.e., $\approx 0.025\ eV$. This provides an additional range of choice of the order of k_BT because there will be partially occupied levels in a shell of width K_BT around the E_F. Combining the above considerations, we can express the electron-electron scattering rate as [Ash76c, Abe72]:

$$\frac{1}{\tau_{e-e}} = s_1(E_1 - E_F)^2 + s_2(k_BT)^2 \tag{1.22}$$

Where the coefficients s_1, s_2 are independent of E_1 and T.

1.3 Single-, Multi-Photon Photoelectric Emission (MPE)

In electron photoemission from a metallic surface, the optically excited electrons must travel through a finite thickness of the solid before they can reach the surface. When the electrons reach the surface they must escape over the potential barrier of the solid before they can appear in vacuum as free electrons [Spi72a]. This means, that there are electrons that absorb the required number of the photons in order to leave the metal ($n\hbar\omega > W$) but due to scattering with the other electrons or with the lattice can not reach the metal surface.

The main feature of the photoelectron emission is the following : when an electron absorbs one or more laser photons and acquires more energy that the work function, then it leaves the metal. The n-photon photoelectron current density, $J_{n\omega}$, is expressed in the transient perturbation theory as [Smi62, Bun65, Sil71, Geo95]:

$$J_{n\omega} = \sigma_n \times I_\omega^n \tag{1.23}$$

where $n =< 1 + W/\hbar\omega >$, (the $< x >$ denotes the integral part of the number x), σ_n is the total n-photon photoelectron cross-section and I_ω is the intensity of the laser beam.

Another important parameter in the photoelectron emission is Keldysh parameter [Kel65, Ani77], γ_K, which is defined as:

$$\gamma_K = \frac{\omega}{eE_o\sqrt{2mV_o}} \tag{1.24}$$

where ω is the laser frequency, E_o is the slowly varying part of the laser electric field and V_o is the depth of the potential well of the metal. The parameter γ_K can be understood as the ratio of the light frequency and the tunneling frequency ($= \sqrt{2mV_o}/eE_o$). The last frequency reproduces the mean time required by an electron to leave the metal by tunneling effect. Consequently, $\gamma_K << 1$ reproduces the situation where the tunnelling effect happens many times in a field period. In this limit, the perturbation theory fails and the photocurrent density is expressed as (Fowler-Nordeim equation):

$$J = \frac{e^2}{16\pi^2}\frac{I}{\hbar W}e^{-\frac{4}{3}\frac{\sqrt{2m}}{\hbar eE_o}W^{3/2}} \tag{1.25}$$

Note that for laser intensities higher than a few GW/cm^2, temperature effects in the metal cathode set in before the purely high intensity photoelectron emission, and are the dominant process involving laser intensities for which the tunneling effect may occur [Fuj84, Ani77, Yen80, Yen82, Gir93, Gir95]. Temperature effects arise from the n-photon absorption by electrons as deep as $n\hbar\omega$ below the Fermi energy, which do not exceed the threshold of n-photon absorption, see Fig. 1.2. The relaxation of these excited electrons by non-radiative processes produce heating of the metallic cathode. More discussion on these phenomena is presented in chapter 4.

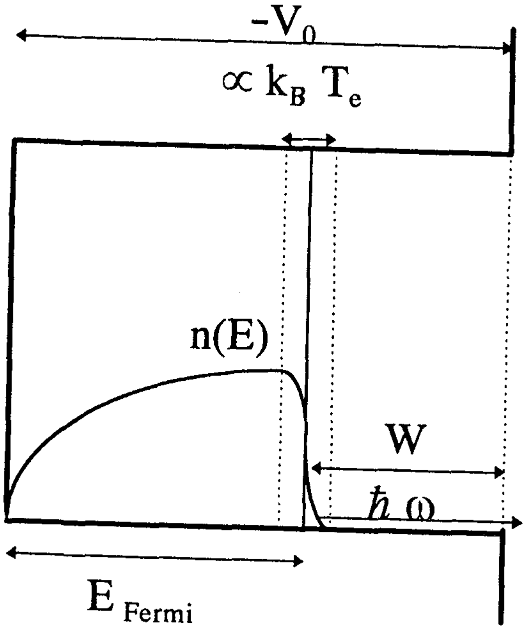

Figure 1.2: Metal surface potential well. $n(E)$ is the product of Fermi-Dirac distribution function (probability of occupation of a state of energy E) and the density of states function which is proportional to $E^{\frac{1}{2}}$ for electrons in a potential free space. Electrons of energy $n(E)$ may absorb a photon of energy $\hbar\omega$ only if at energy state $E+\hbar\omega$ exist free position. If this excitation occurs the excited electrons have a high probability to relax by electron-electron scatterings. The latter mechanism increases the electron temperature and the result is to have enough electrons above the Fermi-Level. At this time the laser photons have a higher probability to be absorbed by the electrons of the hot tail of the Fermi-Dirac distribution and escape the metal.

1.4 Multiple Harmonic Generation(MHG)

In a non-linear medium irradiated by an intense optical beam, i.e., laser pulses, the spectrum of the field can be modified and harmonic radiation may be observed. Thus, when a laser beam illuminates a metallic surface, simultaneously with the multi-photon photoelectric emission, photon production with frequency n times the laser photon one, may occur. Effectively, the electrons in the metal surface may absorb n photons with $\hbar\omega$ energy and relax to the initial state -or near to the initial state- after emitting one photon with energy equal to $n\hbar\omega$. Such phenomena are observed in atoms (mainly in rare gases) and in dielectric crystals [Blo65].

The main difference between metallic surface harmonic generation and atomic harmonic generation is that at the surfaces the inversion symmetry is broken and the nonlinear susceptibility is not vanishing in contradiction with the gaseous atoms which are centrosymmetric media and so there is no even-order optical response in the dipole approximation. Thus, in metallic harmonic generation, one can expect both odd and even harmonics.

Another difference between harmonic generation from metal surfaces and from atoms is the sharp discontinuity of dielectric constant ϵ at the surface of the metal. This discontinuity requires the n-harmonic generation wavevector to be parallel with the reflected fundamental one. Fig. 1.3 shows the configuration of the harmonic generation from a metal surface. Assume that, the incident laser beam illuminates the metallic surface under an angle of incidence equal to θ, and the produced n-harmonic beam, in the space 1, is emitted in random angle $\theta_{R,n}$. Also, assume that the electric field of the incident laser beam is equal to $\vec{E_1} = \vec{E_1^o} e^{i\omega t - i\vec{k}_{out}\vec{r}} + c.c.$ and is linearly polarized in the plane of incidence, $\vec{k}_{out}$ is the wavevector of the incidence beam outside of the metal. Inside the metal, there exist, the fundamental electric field, $\vec{E_2}$, (angle θ_t) and the produced n-harmonic electric fields, $\vec{E}_{2,n}$ (angle $\theta_{t,n}$). In the reflected direction, there exist, the reflected fundamental beam with electric field equal to $\vec{E_2}$, and the n-harmonic beams with electric field $\vec{E}_{1,n}$. Since the n-harmonic electric field is proportional to n-th power of the fundamental electric field, the electric fields are expressed as:

$$\vec{E}_{2,n} = \vec{E^o}_{2,n} e^{in\omega t - ink\vec{n}_{in}\vec{r}} + c.c. \tag{1.26}$$

$$\vec{E}_{1,n} = \vec{E^o}_{1,n} e^{in\omega t - ink\vec{n}_{out}\vec{r}} + c.c. \tag{1.27}$$

$$\vec{E}_1 = \vec{E^o}_1 e^{i\omega t - i\vec{k}_{out}\vec{r}} + c.c. \tag{1.28}$$

$$\vec{E}_r = r_o \vec{E^o}_1 e^{i\omega t - ik\vec{n}_{out}\vec{r}} + c.c. \tag{1.29}$$

where $\vec{k}_{in}$ is the electric field wavevector of the fundamental beam in the metal surface, and r_o is the reflection coefficient of the fundamental electric field. For good conductors like the metallic surfaces, the light absorption is very strong. Thus, using the continuity conditions of the tangential component of the fundamental electric field in the interface metal-air, it is derived that the absolute square of the reflection coefficient r_o (for the geometry that the fields are parallel to the reflection plane) is expressed as [Mat75]:

$$R_{par} = r_o r_o^* = \frac{(n - \frac{1}{cos\theta})^2 + k^2}{(n + \frac{1}{cos\theta})^2 + k^2} \tag{1.30}$$

where n, k is the real and imaginary part of the complex refractive index of the metal, for example in Fig. 1.4

Also, the refractive index of a metal is the square root of the dielectric constant. The dielectric constant of a free electron gas is $\epsilon(\omega) = \epsilon_o[1 - \omega_p^2/\omega(\omega + i\zeta)]$, where ω_p is the plasma frequency of the free electron gas of the metal and ζ is the dumping constant.

The vertical to the surface component of the wavevector in a metal is written as: $k_z = (\omega/c)[\epsilon(\omega)/\epsilon o - sin^2\theta]^{1/2}$, where the inverse of the imaginary part of k_z is the penetration depth of the electric field in to the metallic surface. Now, using the continuity condition of every n-order harmonic field, i.e. the continuity of the tangential components of the electric field it is easy to derive for every n-harmonic that: $k_{in} sin\theta_{t,n} = k_{out} sin\theta_{R,n}$ where $k_{in}^n = k_{in}$ and $k_{out}^n = k_{out}$ and compare to the Fresnel law : $k_{in} sin\theta_{t,n} = k_{out} sin\theta$, it is derived that $\theta_{R,n} = \theta$, i.e., the reflected harmonics are all collinear and also, collinear to the reflected fundamental beam.

Another feature of the metallic harmonic generation is the surface character of the effect. The first experiments on harmonic generation [Bro65, Bro66] reported the second

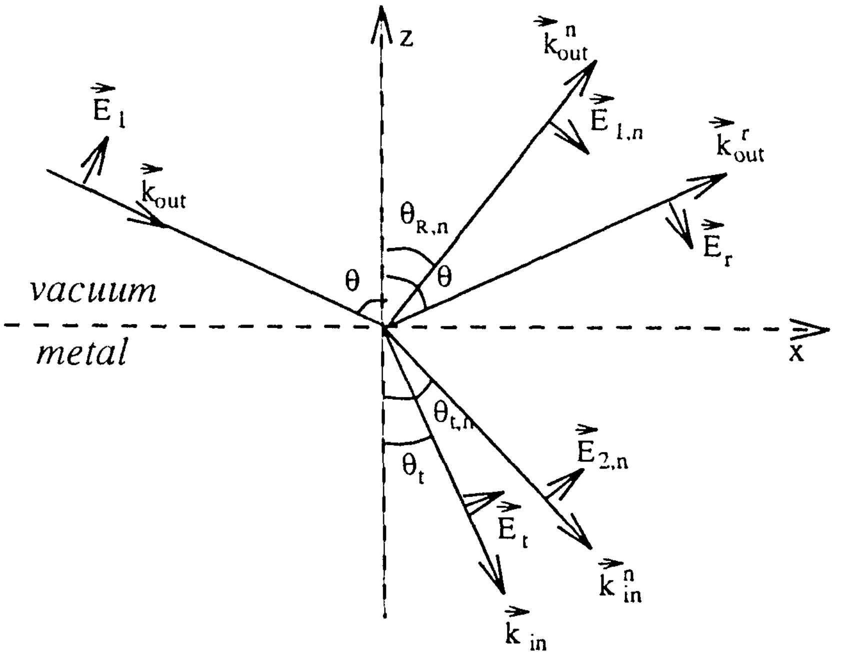

Figure 1.3: Geometrical optics in the case of surface harmonic generation using p-polarized laser beam. The continuity conditions impose the reflected harmonics to be collinear with the reflected fundamental laser beam.

harmonic generation in reflection from a silver mirror. This paper established the existence of the $\vec{E}(\nabla\vec{E})$ nonlinear surface term in the harmonic generation, which is non-zero only at the surface of the metal due the discontinuity there of the metal dielectric constant. Consequently, the surface harmonic generation is predominantly depended on the p-polarized component of the electric field. Only the electric field perpendicular to the surface may produced harmonic photons.

A simple classical but realistic model to describe the second order non-linearities of the free electrons of a metallic surface is to handle it as plasma. As it is reported in ref.[Jac75], two equations, the equation of motion and the continuity equation are necessary to describe an electron plasma:

$$\frac{\partial\vec{v}}{\partial t} = -\frac{\vec{\nabla}P}{m\varrho} - \frac{e}{m}(\vec{E} + \frac{1}{c}\vec{v}\times\vec{B}) \tag{1.31}$$

$$\frac{\partial\varrho}{\partial t} + \vec{\nabla}(\varrho\vec{v}) = 0 \tag{1.32}$$

where ϱ is the electron density, $\vec{v}$ the electron velocity P is the pressure (electric or magnetic), $\vec{E}$ is the electric field and $\vec{B}$ is the magnetic field.

Following the analysis of Y. R. Shen [She84], we may assume $\vec{\nabla}P=0$ for simplicity. Then,

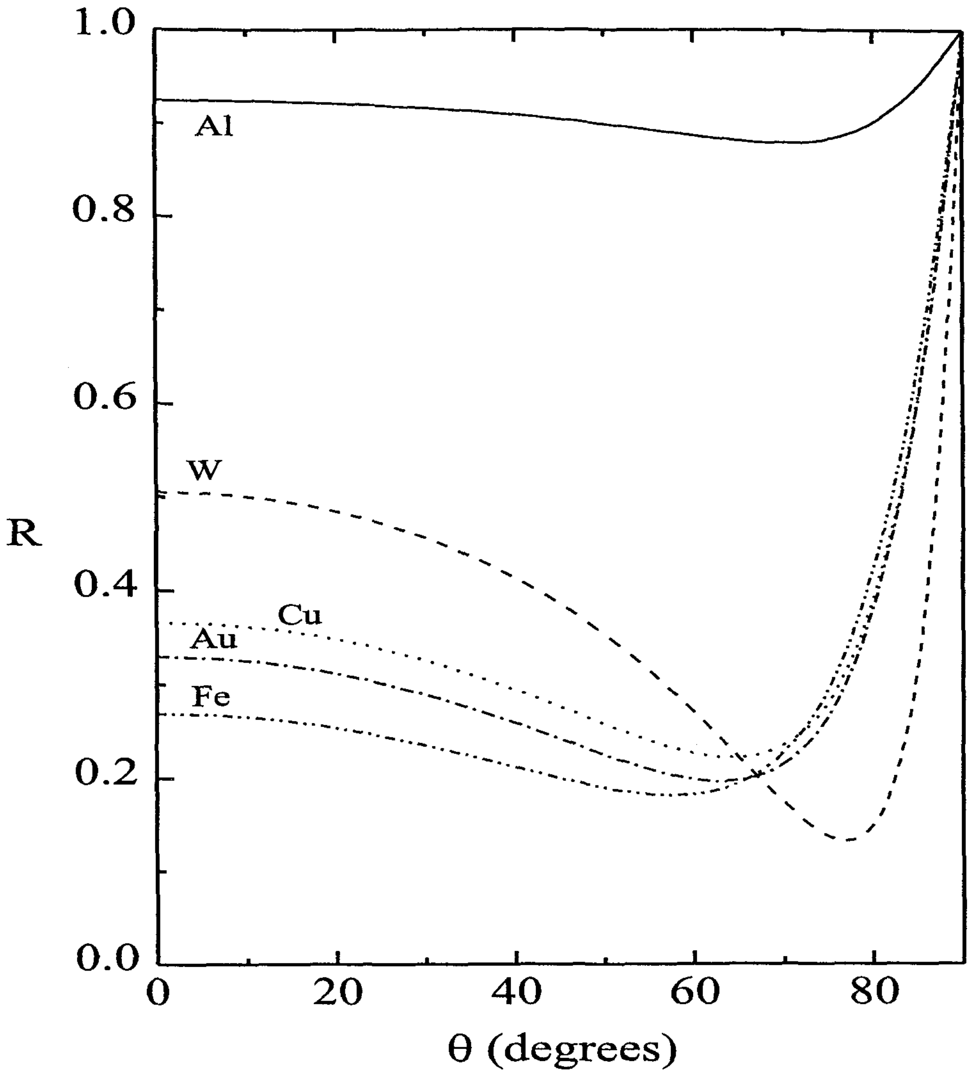

Figure 1.4: Reflectivity coefficient for various metals at 248 nm wavelength p-polarized incident laser beam versus the angle of incidence, θ.

equations (1.31), (1.32) are coupled to the Maxwell equations:

$$\vec{\nabla} \times \vec{E} = -\frac{1}{c}\frac{\partial \vec{B}}{\partial t}$$

$$\vec{\nabla}\vec{E} = 4\pi(\varrho - \varrho^{(0)}) \tag{1.33}$$

$$\vec{\nabla} \times B = \frac{1}{c}\frac{\partial \vec{E}}{\partial t} + \frac{4\pi\varrho\vec{v}}{c}$$

$$\vec{\nabla}\vec{B} = 0 \tag{1.34}$$

where it is assumed that there is a fixed positive charge influence in the electron plasma in order to assure charge neutrality in the absence of external perturbations. Now let us put:

$$\varrho = \varrho^{(0)} + \varrho^{(1)} + \varrho^{(2)} + \dots$$
$$\vec{v} = \vec{v}^{(1)} + \vec{v}^{(2)} + \vec{v}^{(3)} + \dots$$

and

$$\vec{j} = \vec{j}^{(1)} + \vec{j}^{(2)} + \vec{j}^{(3)} + \dots \tag{1.35}$$

with

$$\vec{j}^{(1)} = \varrho^{(0)}\vec{v}^{(1)} \tag{1.36}$$
$$\vec{j}^{(2)} = \varrho^{(0)}\vec{v}^{(2)} + \varrho^{(1)}\vec{v}^{(1)}. \tag{1.37}$$

Assuming an external electric field $\vec{E} = \vec{\varepsilon} e^{i\vec{k}\vec{r}-i\omega t}$ and substituting equation (1.35) into 1.31, 1.32, and 1.34, we get

$$\frac{\partial \vec{v}^{(1)}(\omega)}{\partial t} = -i\omega\vec{v}^{(1)} = -\frac{e}{m}\vec{E} \tag{1.38}$$
$$\frac{\partial \varrho^{(1)}(\omega)}{\partial t} = -i\omega\varrho^{(1)} = -\vec{\nabla}(\varrho^{(0)}\vec{v}^{(1)}) \tag{1.39}$$
$$\vec{\nabla}\vec{E} = 4\pi\varrho^{(1)}(\omega) \tag{1.40}$$
$$\frac{\partial \vec{v}^{(2)}(2\omega)}{\partial t} = -i2\omega\vec{v}^{(2)} = -(\vec{v}^{(1)}\vec{\nabla})\vec{v}^{(1)} - \frac{e}{mc}\vec{v}^{(1)} \times \vec{B}. \tag{1.41}$$

Then, the second order current density is given by:

$$\vec{j}^{(2)}(2\omega) = \frac{i\varrho^{(0)}}{2\omega}\left[\frac{e^2}{m^2\omega^2}(\vec{E}\vec{\nabla})\vec{E} + \frac{ie^2}{m^2\omega c}\vec{E} \times \vec{B}\right] + \frac{e}{i4\pi m\omega}(\vec{\nabla}\vec{E})\vec{E}. \tag{1.42}$$

The term $(\vec{E}\vec{\nabla})\vec{E}$ as well as $(\vec{\nabla}\vec{E})\vec{E}$ are called surface terms because they are related to the spatial variations of the electric field. Spatial variations of the $\vec{E}$ occur only in the surface of a metal and only in the vertical to the surface component of the electric field. The other term, $\vec{E} \times \vec{B}$, is the Lorrentz term which is a bulk term. Note here, that the surface terms, as in the second harmonic generation on metallic surfaces, must exhibit a strong polarization dependence.

1.5 Experimental Considerations for MPE and MHG

The metallic surfaces must be prepared in a special way in order to ensure that there is no pollution or oxidation on them, that may affect MPE and MHG. A metallic surface, that is inert in air with most reagents, is gold. This is one of the main reasons that gold is chosen for the experiments. Experience in studying many materials shows that the procedure necessary to provide a sufficiently clean surface, as well as the vacuum conditions necessary to retain this surface during measurements, vary considerably depending to the material. Thus, without studying a material, it is impossible to say what are the sufficient conditions necessary to have successful experiment.

In the experiments presented here, the metallic surfaces are cleaned in a special way before use, and special care is taken to maintain the surface clean during the experiments. Initially, the massif metal is prepared to form a mirror-like surface, treated by 1 μm thick diamond compound for many hours, then it is cleaned in an ultrasonic bath for 2 hours and finally dried in an oven at $\approx 200^oC$. In most of the experiments, the metallic surfaces are kept in vacuum chambers under $10^{-8} - 10^{-4}$ mbar. Particularly in the electron photoemission experiments it is necessary to study the metal in a high vacuum, in order to collect the electrons by the high collecting voltage without any electrical breakdown. The vacuum system consists of a rotary pump and turbo pump and in most of the cases an ionic pump. The whole system is able keep the metal in a vacuum of the order of $10^{-8} mbar$. The required time to form a monolayer of certain gases on a surface, assuming unity sticking coefficient, is shown in Fig. 1.5 [Spi72b]. During the sixties there were many experimental works on surface cleaning [All66].

A clean surface in a 10^{-8} mbar vacuum, requires few minutes to form a monolayer of the atmosphere gas on it. The laser intensities at the focal point used in the experiments of this thesis, have intensities of the order of few GW/cm^2. Thus, the laser is able to clean the metallic surface by photodynamic way. Particularly, when the metallic surface was irradiated in situ by 248 nm UV laser pulses of a few GW/cm^2 laser intensity. The 5 eV photon of the above laser can destroy the chemical bond of the absorbed gas from the metallic surface and

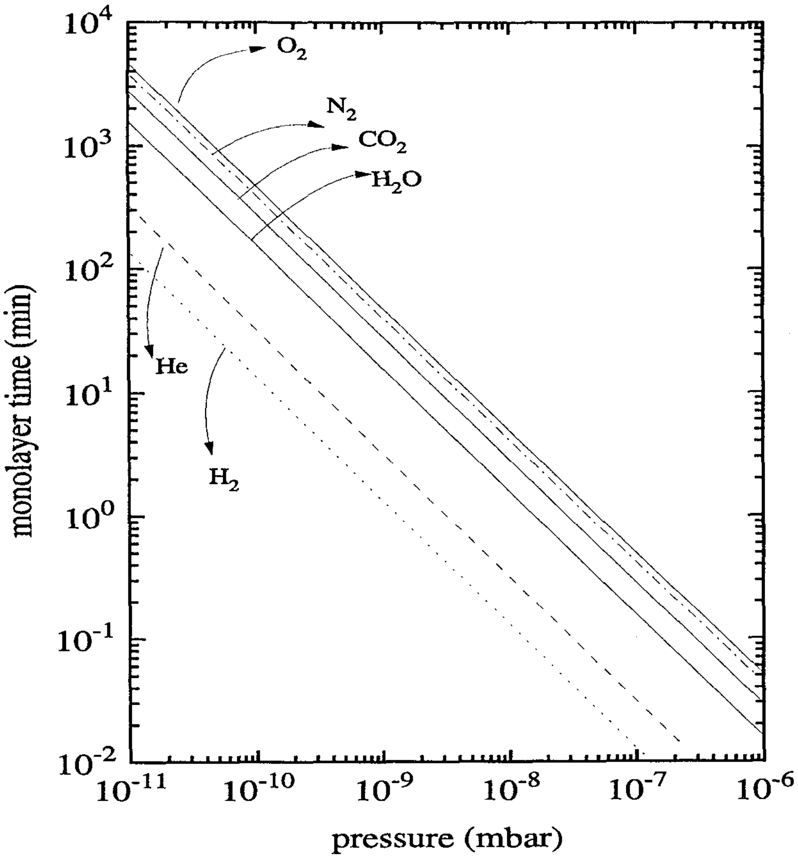

Figure 1.5: Time required to form a monolayer of certain gases on a surface assuming unity sticking coefficient.

thus laser cleaning of the surface is achieved [Lu94]. The repetition rates of the used lasers varied from 1 Hz minimum up to 80 MHz maximum. According to the data of Fig. 1.5 it is impossible for an initially cleaned surface to form a monolayer in such periods of time.

The surface contamination is controlled by observing the photoemission signal during the time of the laser irradiation. More information for this control is presented in chapter 2.

The output of laser metallic surface interaction is nothing more than electrons and photons. There are three ways of measuring multiphoton effects. The first one is to measure the integrated yield of the multiphoton effects versus the laser intensity. This type of measurement has no time and energy resolution. On the other hand, in the perturbation regime, it is possible from the intensity dependence curve to evaluate the order of the nonlinear multiphoton effect by measuring the slope of the log-log plot of the multiphoton yield as a function of the incident laser intensity. The term multiphoton yield indicates the intensity of the n-harmonic light in the case of n-harmonic generation and the photocurrent density in the case of n-photon photoelectric emission. Also, other phenomena like temperature effects or any other extra nonlinear effects can be observed by the above type of measurements.

The second way of measurement is the time resolved experiments. Using ultrafast laser pulses, one can study the dynamics of the multiphoton effects. Especially in the measurements of electron relaxation time of a metal, the above measurement type is the most suitable. This is proved by the analysis in the introductory part of chapter 4. The last way of measurement is the energy resolved experiments, i.e., the measurements of the total number of n-harmonic photon versus the wavelength or the measurements of the kinetic energy of the emitted electrons. Note here, that for electron energy-resolved measurements there exists a main experimental problem, that is the space charge effect. As mentioned previously, in order to observe MHG or MPE high intensity laser pulses with ultrashort pulses are required. This means that the initially produced electrons are very near with each other in space. The coulomb interaction changes dramatically the energy distribution and thus no information can be derived. Some research groups have published results on photoelectron energy spectroscopy from metallic surfaces i.e., Farkas and Toth [Far90]. They observe electrons with energies of a few hundreds of eV. This fact can be explained only in terms of the space charge effects in the extracted electrons as it is shown by Girardeau-Montaut et. al. [Gir91].

Chapter 2

Study of multi-photon photoelectric emission from metals induced by ultrashort and intense laser radiation.

2.1 Historical Review

It was observed since the begining of the century that most of the metals under the influence of radiation (light), especially ultraviolet radiation, emit electrons. This phenomenon was termed photoelectric emission, and detailed study of it showed:

(a) The emission process depends strongly on the frequency of the light, and for each metal there exists a critical frequency such that light of lower frequency is absolutely unable to liberate electrons, while light of higher frequency always does. Indeed, for a given surface, if the frequency of the light is increased, the energy of the emitted electrons increases in some linear relation.

(b) The emission of the electrons occurs within a very short time interval after the arrival of the radiation, and the number of electrons emitted is strictly proportional to the intensity of radiation. The experimental facts given above were the first evidence for our present-day belief that the electromagnetic fields are quantized.

The electrons are bound inside the metal surface with an energy W where W is the work function. If the frequency, ω, of the light is such that $\hbar\omega > W$ it will be possible to eject photoelectrons. While if $\hbar\omega < W$ the emission is impossible since the probability that an electron will absorb two photons simultaneously was minimal. In the former case, the excess energy of the quantum appears as kinetic energy of the electrons, so that $\hbar\omega = \frac{1}{2}mu^2 + W$, which is the famous photoelectric equation formulated by Einstein in 1905. In writing the equation in this form we express the fact that the energy is shared between the electron and the photon only; however, to balance momentum, a third body is needed, which in this case is the crystal lattice, which recoils with negligible energy.

When the intensity of radiation is increased, i.e., in laser pulses, the above conditions are not inforce. In such a case, an electron can leave the metal absorbing two or more photons. The first estimations of the efficiency of electron emission from a metal as a result of two photon absorption were published well before the discovery of the laser [Mak51].

In fact the opportunity to observe experimentally the multi-photon effects had to await the development of sufficiently powerful lasers. After laser invention several reports of photocurrents proportional to the n-th power of the laser intensity have been published. Experimental [Tei64, Far67], as well as theoretical works [Smi62, Bun65], were carried out in order the multi-photon photoelectric electron emission to be studied in detail.

Initially, most of the experimental investigations of the photoelectric emission from metals used as ejection tools, nanosecond laser pulses [Rea65]. The maximum intensities of these laser pulses were in the range of 10^6-10^7 W/cm^2. Most of used lasers were Q-switched ruby lasers. The observed photocurrent was explained in terms of thermionic emission due to target heating. Further systematic study of these effects, both experimentally and theoretically determined that the photoelectric effect is mainly a multi-photon emission and differs from the thermionic emission. The main differences are:

a) The photocurrent density is proportional to the *nth* power of the laser intensity, where n is the number of the required photon in order the electrons to be delivered. In contrast the photocurrent density for the case thermionic emission is expressed by the well known Richardson's law:

$$j = AT^2 e^{-W/k_B T} \tag{2.1}$$

b) The multi-photon photoelectric effect is strongly suggested to be an instantaneous process. This means that there is not delay between the laser pulse and the current pulse. In the case of Gaussian laser pulses, it is proposed by Anisimov et. al. [Ani77]. that the photocurrent pulse duration, t_j, is related to the laser pulse duration, t_L, by :

$$t_j = \frac{t_L}{\sqrt{n}} \tag{2.2}$$

where n is the number of absorbed photons. In contrast, the duration of the thermionic emission current is depended on the temperature time-decay of the cathode, after the laser action, which in the case of nanosecond laser pulses (normal heating) is of the order of a few μs.

c) As it is already explained in chapter 1, the multiphoton photoelectric emission is predominately a surface effect. The yield of the multiphoton photocurrent density is governed by the component of the electric field normal to the surface. On the other hand, the thermionic emission current is governed by the temperature of the probe region, i.e., the absorbed power of the laser by the metal cathode.

d) The energy distribution of the emitted electrons also differs in the two cases. In the thermionic emission, the emitted electrons have a Maxwellian energy distribution. In the multiphoton case, the electrons energy distribution has a maximum close to the highest energy of the emitted electrons, $E_{max} = n\hbar\omega - W$, and it is independent of light intensity and time, while in thermionic emission case it is proportional to the target temperature and it varies with time.

In the case of photoelectron emission using picosecond (ps) or subpicosecond (subps) laser pulses the situation is different compared to the case of nanosecond (ns) ones. Using ps or subps laser pulses, it is easy for very strong laser electric fields to be achieved . For such a field, perturbation theory should break down. Keldysh [Kel65], and Silin [Sil71], predicted the break down of the power law dependence in the emission current. In reality, when the laser intensity increases, the cathode heating affects, principally, the electron emission. especially in the case of ns pulses. Thus, in order to study the multiphoton photoelectric effects, one must increase the laser intensity by reducing the laser pulse duration and not by increasing the number of the laser photons. The heating of the cathode is different in the case of ns than in the case of ps or subps laser pulses.

The dominant role for the cathode heating is played by electron relaxation phenomena. When the laser pulse duration is less or in the order of electron relaxation time, the thermal equilibrium between the electron and the lattice is disturbed. The result is a high electron temperature which relaxes very fast to the cold lattice. The electrons acquire very fast a high temperature due to the low specific heat of the degenerate electron gas. On the contrary, the heavy ions, with orders of magnitude bigger specific heat, are not affected by the ultrashort pulse. On the other hand, when ns laser pulses are applied, the heating of the electrons is followed by lattice heating having a common temperature at each time instant (normal heating). In the second case, the metallic surface can be destroyed when the lattice temperature exceeds the melting point of the metal.

In the following sections of chapter 2 as well as in the chapter 4, these effects are studied in more detail.

In order to verify the prediction of the theories of Keldysh for the break down of the perturbation theory, many experimental works have been performed [Far72, Far74]. The experiments show a reduction in the degree of nonlinearity at high illumination laser intensity (around 50 GW/cm^2). The break down of the perturbation theory is predicted by Keldysh parameter to happen in about one order of magnitude higher laser intensities. In fact, even for subps laser pulses and for intensities of few 100 GW/cm^2, any metallic surface is destroyed by thermal effects.

After the above analysis it is clear that many question remain without answer. For example; What is the origin of the reduction of the observed degree of the non-linearity?, what is the influence of the thermal effects in the photocurrent emission? and what is the best conditions in order to achieve the maximum photocurrent density? and finally, are the photocurrent density values predicted by the theories? In the next section of this chapter we will try to answer the above questions.

The photoelectric effects are studied in two laser intensity regimes: a) Low intensities, i.e., $I_\omega \leq$ few GW/cm^2 b) High intensities, i.e., for intensities higher than few GW/cm^2

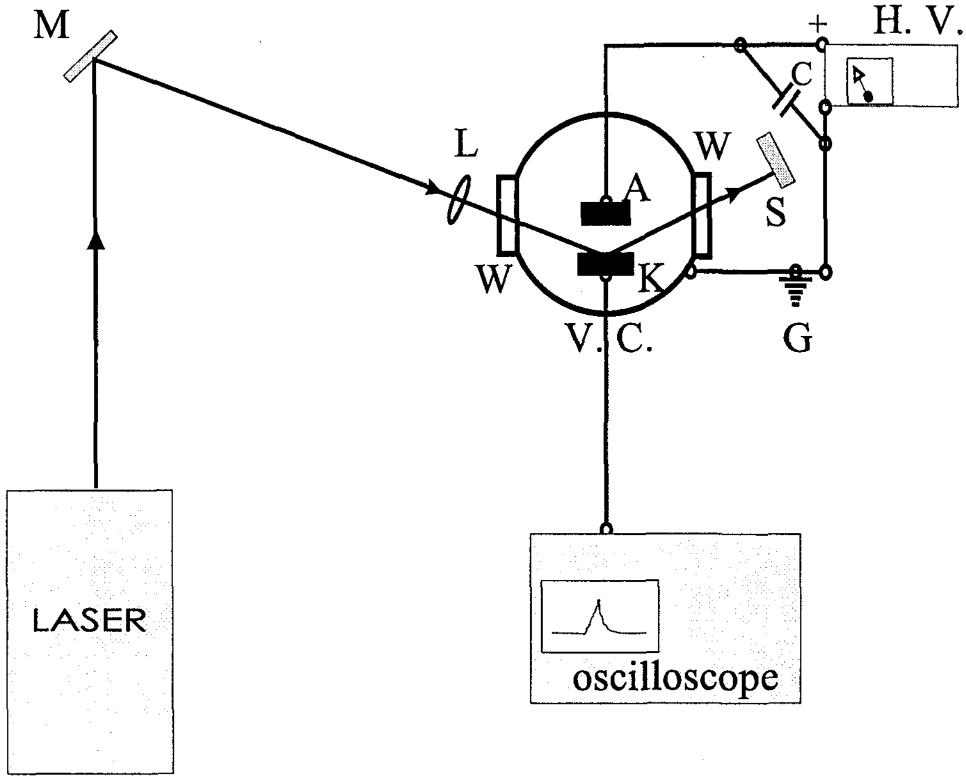

Figure 2.1: Experimental set-up for electron emission from metallic surfaces; K is the metallic photocathode; A is a stainless steel electron collecting anode; L is a the focusing lens; V. C. is the vacuum chamber; W is the windows of the V. C.; S is a beam stopper; M is an optical mirror; G is the ground; C is the charged capacitor; H. V. is the high voltage power supply (0-30 kV).

2.2 Low Intensities

2.2.1 Experiments

For the main part of our experimental work, a polycrystalline gold was tested. There are three reasons for this choice; a) gold surface is inert in air with most of the reagents, b) in the vicinity of Fermi energy it follows quite well the Sommerfeld model for the electrons and since this model is used by most of the theoretical treatments is good for comparison, and c) gold has very good electrical and thermal conductivity properties.

The experimental set-up is shown in Fig. 2.1. The photocathode consisted of an rectangular plate 10×10 mm^2, high purity polycrystalline gold. The work function of our sample is 4.67 eV. The gold is kept in a vacuum vessel in about 10^{-8} mbar. A flat stainless steel anode with an electron gap fixed to 5 mm is placed over the gold cathode.

The laser beam is focused to the gold surface by biconvex silica lens or calcium floride lens with 15-20 cm focal length for the laser wavelength used. The anode was biased at a high voltage, V_A, varying from 0 to 30 kV. The angle of laser incidence, θ, on the photocathode is between 77° and 84° with a precision ±0.2°. These grazing incident angles are used in order to avoid the unwanted thermal effects which destroy the metal surface. Also, in such a laser beam incidence configuration, the electric field of the laser can have the maximum component normal to the surface.

The laser beam was linearly polarized normal to the surface (p-polarization), except for the case that intentionally the polarization is changed, in order for polarization dependence experiments to take place. The photoelectron signal was detected by the 50 Ω input resistance of 1GHZ Tektronix 7904A fast-oscilloscope connected to the photocathode by a 50 Ω cable. Electron pulses were recorded on 3000 ASA Polaroid films and then read with a scanner. For every laser intensity a series of measurements took place by measuring the average value of 50 consecutive electron pulses V_e, as a function of the applied voltage, V_A, in order to achieve the saturation possible. This was not in every case succeeded. The photoelectron charge was evaluated as the product of V_e and the input oscilloscope capacity (20 pF).

The choice of the laser wavelength permitted the one-, two-, three-,and four- photon photoelectric effect. For the single-photon photoelectric effect were used two KrF lasers with 248 nm wavelength, i.e. 5 eV energy. The first one was a common Lambda-Physic excimer laser with a about 15 ns pulse duration. The other was consisted by a Lambda-Physik XeCl laser oscillator which was used to pump a sequence of six dye lasers, providing linearly polarized pulses at 496 nm (2.5 eV) with 450 fs pulse duration. The latter laser beam is doubled in the energy by a BBO doubling crystal, and then is amplified twice by a KrF excimer laser amplifier [Sza88]. The final beam has a 450 fs duration at 248 nm (5 eV). The used repetition rate of both lasers was 3-5 Hz. Diagnostics are performed by 1 m Littrow-type spectrograph and a multi-shot cross-correlation measurements using a Michelson-type autocorrelator and measuring the yield of electrons that the laser beam produce in the NO gas via two-photon ionisation process. Attention was paid for low amplified spontaneous emission either by the energy measurements via the spectrograph either by controlling the 3:1 peak-to-background ratio in the second order cross-correlation curve.

The laser photon energy was higher than the gold work function W=4.68 eV and thus the photoelectric emission corresponds to a single-photon process.

The laser beam was linearly polarized. The highest photoemission yield was observed for the p-polarization arrangement. This is the reason that p-polarized incident radiation was kept for the whole experiment. For the case of ns laser and for laser intensities (100-250) MW/cm^2, the photocurrent signal (V_e) was saturated at about 10-15 kV applied voltage. This means that the photoelectric emission is in the space-charge-limited region, as is described by Girardeau-Montaut et. al. [Gir89, Gir89a].

For the case of 450 fs laser pulses the current saturation vs the applied voltage was not successful every time. For intensities higher than several hundreds MW/cm^2, the saturation current is not possible to be achieved in the range of the used applied voltage. This region is called the non-space-charge-limited and the experimental data need to be corrected. Using the shape of the curves for space charge limited region, the saturation current for the non-space-charge region can be estimated with a satisfactory precision. The estimated values is close enough to these calculated by the code of the refs.[Gir89, Gir89a]. Typical V_e vs V_A curves are shown in Fig.2.2

Higher order multiphoton photoemission currents (n=2,3,4) were measured using the same experimental arrangement for the Au surface. For the case of n=2 the 450 fs green laser pulse (496 nm) was used. This is a laser pulse that was provided by the sequence of the six dye laser pumped by the XeCl amplifier. Similar tests with the 248 nm, 450 fs laser pulses were performed. The second order cross-correlation measurements took place using as nonlinear medium a BBO doubling crystal or the metallic surface itself. These techniques for the pulse characterization are presented at chapter 5. The repetition rate of the green laser was 3-5 Hz. The photon energy is 2.5 eV, i.e., two laser photons are required in order to produce photoemission. The tested intensities were of the order of a few GW/cm^2. The polarization dependence was similar to that for 248 nm laser pulses.

For the case of n=3, we used the 790 nm, 110 fs laser pulses produced by a Ti:sapphire laser with a repetition rate about 80 MHz. Characterization of the Ti:sapphire laser pulse have

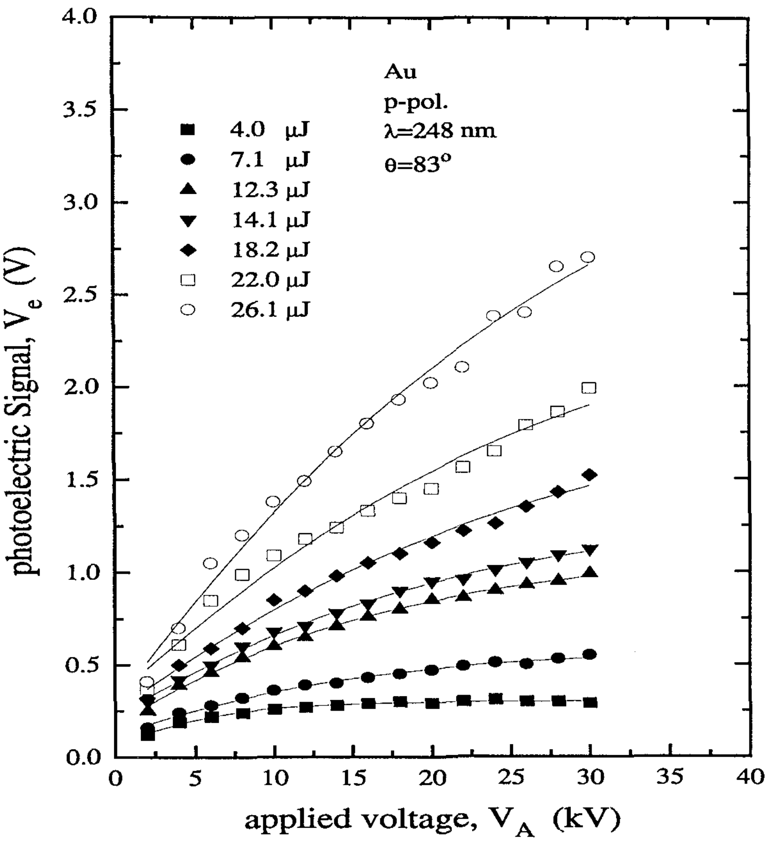

Figure 2.2: Typical curves of photoelectric signal, V_e, versus the applied collecting voltage for various p-polarized 248 nm and 450 fs laser pulse energies. The metallic surface was a polycrystalline gold and the angle of laser incidence was 83°. The photoelectric emission for this case is single photon.

been performed using second- and third-order cross-correlation measurements via the second and third harmonic generation from the gold surface. These measurements are presented in chapter 5, but briefly the conclusions are that the Ti:sapphire laser pulse is fully coherent with a duration between 100-110 fs, FWHM of its symmetric Gaussian temporal profile.

The photon energy is 1.57 eV. Unfortunately, for this case the maximum laser intensity for the grazing incidence angles used in this experiments was in the range of several tens MW/cm^2. Varying the direction of the input polarization relative to the surface normal using a λ /2 plate, the photocurrent signal was measured. The polarization dependence curves are similar to that of n=2 and n=3 case and are presented in Fig. 2.3 for three different angles.

Because of the low laser intensity used in this case, the saturation current is measured for relatively low applied voltages ($\leq 10kV$).

Finally, for the case of n=4, a Nd-YAG laser emitting 1.17 eV photon energy was used. The pulse duration of the Nd-YAG laser was 35 ps as measured by second-order cross-correlation in a KDP crystal. The polarization dependence curve for this also case shows that the dominant current is produced by the component of the electric field which is normal to the surface.

The different orders of the multiphoton photoeffects for the case of $\theta = 80^o$ incident laser angle are shown in Fig.2.4.

Similar results were obtained by using various metallic photocathodes as W, Al, Cu, Fe. For intensities up to 1 GW/cm^2, the above metals showed a very good agreement with the N-power law dependence on the laser intensity and with the p-polarization dependence of the photoelectric emission. More experimental results for the photoemission of these metals are presented in the section for higher laser intensities of this chapter, as well as in chapter 4 of this work.

2.2.2 Results and Discussion

The dependence of the electron current on the laser intensities used in our experiments exhibits an interesting feature. The general expression relating the current density J and the laser beam intensity I is $J \propto I^n$, where n is the number of the absorbed photons. The $log - log$ plot of the Fig. 2.4 shows that up to about 1 GW/cm^2 the above power law is correct for all the order of the non-linearity.

On the contrary, in the case of n=1 (mainly) and n=2, a positive systematic deviation of the n-power low is observed. This deviation indicates a higher efficiency of the surface photoeffect for these intensities in the femtosecond range. For ns laser pulses, it is impossible to reach such intensities values without the destruction of the metal surface by thermal effects and plasma creation. The origin of the observed deviation, in the fs case, has again thermal character but in another sense. There is a difference between lattice and electron

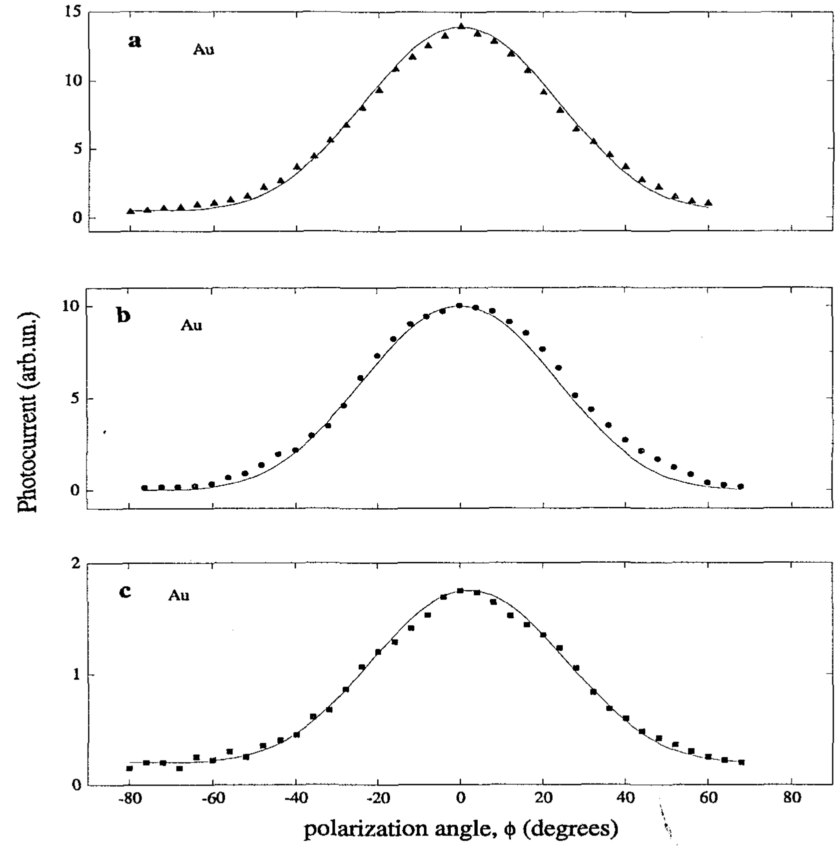

Figure 2.3: Three-photon photoelectron emission signal dependence on the polarization angle. $\Phi = 0^o$ corresponds to p-polarization. The pumping laser is a Ti:Sapphire laser (790 nm) with about 110 fs pulse duration and intensity 30 WM/cm^2. The solid lines are $cos^6\Phi$ function shown the third order of the process. (a) Angle of incidence 75.5^o. (b) 81^o and (c) 84^o.

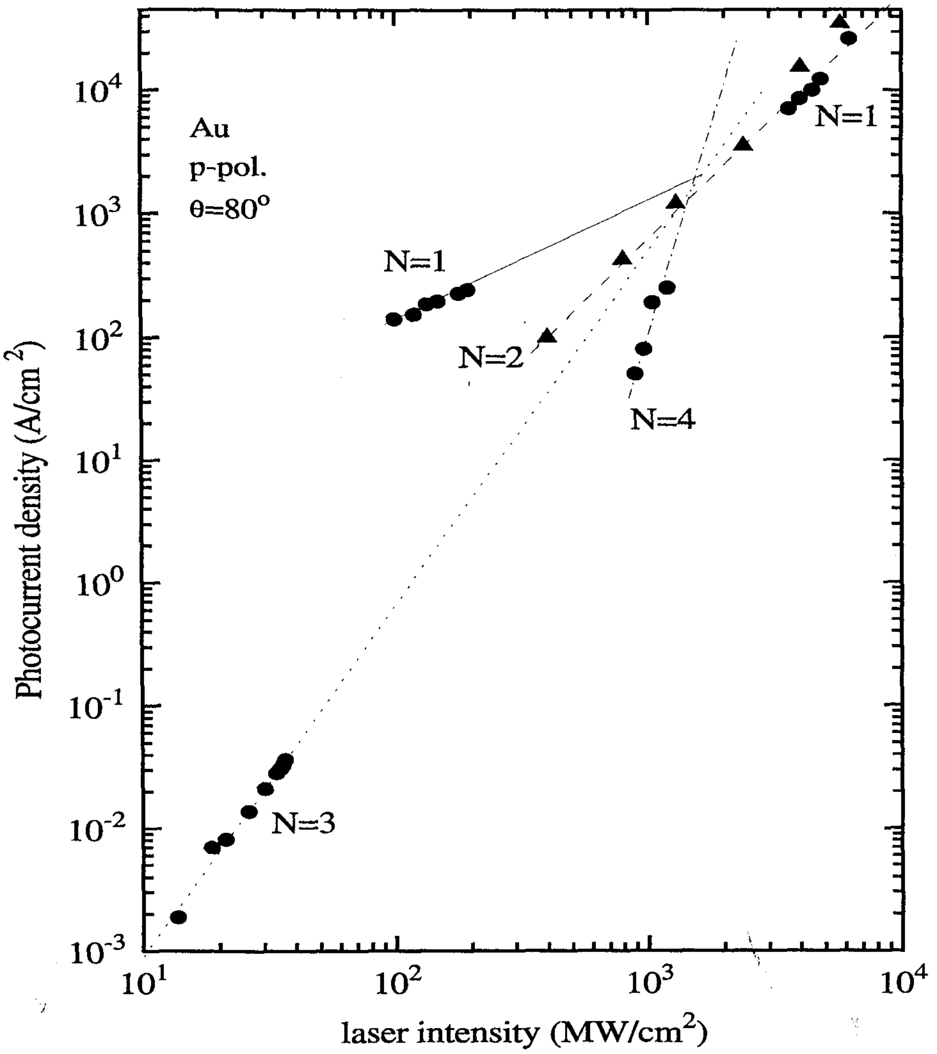

Figure 2.4: Log-log plot of emitted photocurrent density for various orders of multiphoton electron emission from gold, vs laser intensity. The angle of laser incidence was 80° for all the different cases. For the N=1 case at the low laser intensities; few 100 MW/cm^2, the incident laser pulse had duration about 15 ns and photon energy equal with 5 eV. For N=1 and high intensities the laser pulse was a 450 fs duration and photon energy again 5 eV. For the N=3 case the laser pulse had duration 110 fs and photon energy 1.57 eV and for N=4 case the laser pulse was 35 ps with photon energy 1.165 eV. The work function of Au is 4.68 eV. Note that except from N=1 curve at high intensity region and few points of N=2, the slopes are equals to the order of the non-linearity of the photoemission.

temperatures. The electrons are rapidly thermalized in a high temperature but the lattice temperature remains almost constant (room temperature) due to its high specific heat. The non-linear change of the temperature of the electrons in the Fermi - Dirac distribution affects positively the photocurrent emission. The detailed study of this effect is present in the section: high intensity of this chapter as well as in chapter 4.

In the following, we limit ourselves in the intensity region, where the power law is valid. The first experimental result is that the photocurrent density can easily reach values of several kA/cm^2 for about 1 GW/cm^2 laser intensities. Another important observation is that for laser intensities about 1 GW/cm^2 the various multi-photon orders exhibit the same order of magnitude photocurrent density emission, i.e., about 10^2 to 10^3 A/cm^2, see for example Table 2.1 This fact could either put in question the validity of the perturbation theory for the laser intensities used in the experiment or there is another effect that probably makes the high order non-linear photocurrent more efficient for laser intensities more than 1 GW/cm^2. The first suggestion is wrong. The Keldysh parameter that calculates the intensity limits for the validity of the perturbation theory has a value that in any case is of the order of a few hundreds, see Table 2.1.

Perturbation theory breaks down for the laser intensities higher than a few 100 GW/cm^2. But, this is the damage threshold of the metallic surfaces in the subpicosend regime as it was observed many times in our experiments. Thus, it is valid to conclude that it is impossible to observe tunneling effects in such an experiment like the above. At this point, the question that arises is: what is the cause of the observed reducing in the order of photocurrent from the n-power law observed by Farkas et. al.? (their results are presented in the introductory historical part of this chapter). The explanation that is suggested is that in high laser intensity regime space charge phenomena reduce the measured photocurrent signal.

The explanation for the similar efficiencies of the different orders of photoelectric emission in the laser intensity region of the 1 GW/cm^2 must be a fundamental one. In the case of atoms, and for intensities that the perturbation theory is valid the effect of the n-order ionization is typically a few order of magnitude smaller than in the case of $(n-1)$-order of ionization. Similar values are observed for other non-linear phenomena in the range of validity of the perturbation theory, even though the transitions are between resonance states.

In the independent electron approximation of the Sommerfeld model for metals the electronic states are extremely near each other (continuum-like spectrum) but the bandwidth of every state is only the intrinsic one. If we imaging gradually turning on the interactions between electrons, and between electrons and lattice, this will lead to an increase in the bandwidth of the states. This effect may increase the photocurrent of the higher orders because it makes the photoabsorption process to be incoherent and stepwise and not direct [Geo95].

Another point is that the photoeffect depends on the electric field component of the laser light perpendicular to the surface. The p-polarization dependence can be explained from the basic laws of energy and momentum conservation. The surface electrons are free to move in the plane of the cathode surface. It is known that a free electron can not absorb photons because it can not conserve energy and momentum simultaneously. On the contrary, in the perpendicular to the surface direction the force from the positive ions restrains the electrons with the metal surface, thus in this direction there is a possibility for photon absorption. The above observations suggest that the produced photocurrent is predominately from surface electrons. This is called surface photoeffect.

On the contrary, when the electrons come from the bulk of the metal the n-photon photocurrent density depends on the absorbed light energy, E, which is proportional to the $2n^{th}$ power of the total light electric field strength. This is the volume photoeffect. The low photocurrent density (compared to the p-polarization case) that measured in the s-polarization case of our experiment may be explained in terms of volume photoeffect.

Most of the works up to now indicated that the volume photoeffect is lower compared to the surface photoeffect [Gir93a], but it is about the same order at normal incidence, as shown by both p- and s-polarized light at 4.66 eV on Cu [Sri91].

2.2.3 Theoretical Interpretations

The surface photoelectric effect from pure metals was the subject of many theoretical studies in the far past e.g., ref.[Mit36]. These theories used the approximation that no photoelectric current can be produced at energies less than the work function of the metal. All these treatments was based on the first order perturbation analysis. During the sixties the calculations took in account the multiphoton photoemission. The first theoretical work was done by R. L. Smith [Smi62]. He used second-order perturbation theory in order to calculate the two-photon photoelectric emission. He derived the basic power law and the polarization dependence of the two-photon photoemission.

Smith's formula is used in order to compare the calculated two-photon photocurrent with our experiment results for Au. The laser photon energy was 2.5 eV, the work function of Au is W=4.68 eV and the laser intensity was I_ω=1 GW/cm^2 i.e., the electric field was 7.8 $\times 10^7$ V/m. According to Smith's formula a current equal to 12 A/cm^2 is calculated. This value is more than one order of magnitude smaller than our experimental result ($\approx$630 A/cm^2). However, the difference is not so dramatic, taking into account the neglect of reflection and refraction of the light in the metal surface, as well as the simplicity of the free electron model used in this treatment.

In the following years theories both perturbative and no perturbative have been developed [Bun65, Sil71, Mis91, Dan92]. These theories are based on the Sommerfeld model of a metal. Most of the theories predict the n-power low and the polarization dependence of the photocurrent as it is shown in the experiments. For the single-photon photoelectric effect they predict photocurrent density about 3-orders of magnitude higher compared to the experimental results, see Table 2.1. But, the main problem of these theories is that they predict a very low current for the $n \geq 2$ photoelectric effect. As the order of the photocurrent increases the deviation between the theories and our experiments get worse, see for example Bunkin theory [Bun65] in Table 2.1.

For many years no theory had appeared to calculate the multiphoton photoelectric density. In any case, the experiment showed that the above mentioned theories have major problems.

Very recently, a new theoretical treatment for the multiphoton photoelectric effect was published by A. T. Georges [Geo95]. Considering that the possible problem of the previous theories is the use of the simple free electron model for the metallic surface, the new theory is based on an extension of the Sommerfeld model of a metal that takes into account the energy and momentum relaxation.

In the latter theory, the metal is described by the well-known model of the one-dimensional step potential, which is presented in the introductory chapter. The novelty of this theory is that the effect of electron-phonon interaction is taken into account by broadening each bound state in the continuum for negative electron energies by $\hbar\Gamma$, where Γ is the dephasing rate of the bound electronic states. Γ is electron-phonon momentum scattering rate, i.e., $\Gamma \approx 10^{15} sec^{-1}$. Another important rate is the electron-phonon energy relaxation rate. This rate can be understood as the statistical rate for energy relaxation of the electron-gas after the inelastic collisions with the lattice and is of the order of $10^{11} sec^{-1}$.

In the next paragraphs we present the treatment by Georges [Geo95]. He uses normalized wavefunctions:

$$\Phi_I(z) = \frac{1}{\sqrt{N_I}} \sum_{i=1}^{N} w_i^{1/2} \phi_i(z) \tag{2.3}$$

where $\phi(z)$ are the unperturbed wavefunctions of the step potential (see chapter 1), w is the Lorentzian weights of the mixed states, $N_I = \pi g(\omega_I)\Gamma/2$ is the effective number of states within a Lorentzian line shape of width Γ, and $g(\omega)$ is the one-dimensional density of states for each spin state. The electron transitions are considered resonant through these mixed states.

The value of the z-component (normal to the metal surface) of the electric dipole between two such states is

$$\mu_{I,J} \approx \frac{\pi}{2} \sqrt{g(\omega_I) g(\omega_J)} \Gamma \overline{\mu_{i,j}} \tag{2.4}$$

where $\overline{\mu_{i,j}}$ is the average dipole over the $N_I N_J$ pairs of unmixed states.

Applying the equation of motion for the slowly varying part of the off diagonal matrix elements of the density matrix for N-1 states in the case of N-photon photoelectric emission and using the rate approximation for the weak field case and steady state approximation the population of the $N-1$ bound mixed state is expressed as:

$$P_{N-1} = \prod_{N=2}^{N} \frac{|\Omega_{N-2,N-1}|^2}{2\Gamma\gamma}. \tag{2.5}$$

$\Omega_{I,I+1}$ is the Rabi interaction frequency for the coupled by the laser photon states (I, I+1),

$$\Omega_{I,I+1} = 2\hbar^{-1}\mu_{I,I+1}E_{z,0} \tag{2.6}$$

where $E_{z,0}$ is the amplitude of the z component of the electric field at the surface.

Then the photoelectron current density in the presence of the radiation field of the laser is expressed as:

$$\vec{J}(\vec{r},t) = \frac{ie\hbar}{2m}\sum_{l} p_l[\Psi_l\nabla\Psi_l^* - \Psi_l^*\nabla\Psi_l + \frac{i2e}{\hbar}\vec{A} \mid \Psi_l \mid^2], \tag{2.7}$$

where the sum is over the unmixed states, $\vec{A}$ is the vector potential, Ψ_l the final state wavefunction in the continuum and $p_l = P_{N-1}w_l/N_{N-1}$ the probability of an electron to be in one of these states. Applying first order perturbation to one of such states and averaging over an optical period the photoelectron current density evaluated at $z \to \infty$ is:

$$\vec{J}(k_i,\theta_i) = \frac{e\hbar}{m}P_{N-1}\frac{\mid 1+r \mid^2}{V}4\pi^2|\hbar^{-1}\overline{\mu}_{lf}E^*_{z,0}g(\omega_f)|^2 \times [\vec{k}_\perp + q_{zf}\hat{z}]|_{\omega_f=N\omega}, \tag{2.8}$$

where k_i, θ_i are the initial electron wave number and angle from z-axis, respectively, V the normalization volume, (1+r) the transmission coefficient outside the metal surface in the wave function of the final electron state, and $[\vec{k}_\perp + q_{zf}\hat{z}]$ the wavevector of the outgoing photoelectron. The total N-photon photoelectron current density is found by integrating the magnitude of $\vec{J}(k_i,\theta_i)$ over the Fermi sphere.

The above theory, for intensities up to about 1 GW/cm^2 suggests a clear power low dependence $J_N \propto I^N$, as expected from perturbation theory. The parameters which have been used for gold are: Fermi Energy E_F=5.51 eV, depth of the metal step potential equal to 10.19 eV (W=4.68 eV). For the electron-phonon relaxation rate, the experimental value 3 ps^{-1} is used, and the ratio Γ/γ was taken equal to 3×10^4. The theoretical prediction of the theory of ref. [Geo95] comparing to previous theories (e.g. Bunkin [Bun65]) is close enough to our experimental data for N-photon photoelectric effect which are presented in this thesis, see Table 2.1.

λ_L (nm)	γ_K	n	$J_{ex}(A/cm^2)$	$J_{th}^G(A/cm^2)$	$J_{th}^B(A/cm^2)$
248	941	1	1260 ± 100	6220	4.9×10^6
496	471	2	630 ± 75	1350	17
790	295	3	460 ± 30	122	3.2×10^{-4}
1064	219	4	120 ± 20	58	1.3×10^{-8}

Table 2.1: Photocurrent density from a Gold surface with work function 4.68 eV using p-polarized laser pulses with intensity 1 GW/cm^2 and angle of incidence 80^o. λ_L is the laser wavelength, γ_K is the Keldysh parameter, n is the number of photons required to be absorbed by an electron for photoemission, J_{ex} is the photocurrent density measured by us, J_{th}^B is the photocurrent density calculated by Bunkin et al. [Bun65], and J_{th}^G is the photocurrent density calculated by Georges [Geo95].

The low cross-section for the MSPE predicted by the previous theories is due to the destructive interference between the different channels in the assumed coherent excitation process. However, the excitation process cannot possibly be coherent in the presence of electron-phonon collisions with momentum relaxation rates of the order of $10^{15} sec^{-1}$. The rapid dephasing of the bound electronic states makes the optical excitation incoherent and stepwise, and thus more efficient.

2.3 Higher Intensities

The term high laser intensities, for the case of metallic surfaces, characterizes laser pulses with intensities one or two orders of magnitude down from damage threshold of the cathode. The damage threshold is dependent on the time duration of the laser pulses. For laser pulses with ns or several ps duration, the intensity threshold for surface damage is in the order of 0.1 to 1 GW/cm^2. For subpicosecond laser pulses the damage threshold is in the order of 100 GW/cm^2 [Fuj84, Gir95, She89, Wan94].

In the Fig. 2.4 it was already appeared an extra nonlinearity (higher than the number of asborved photons N) for the N-photon PE and for intensities higher than a few GW/cm^2. In order to approach this effect, we performed single-photon experiments for the case where high intensity pulses are applied on the cathode surface.

2.3.1 Experiments

In this section we report the measurements concerning the single-photon electron emission from Gold(Au), Tungsten(W), Aluminum(Al), Copper(Cu) and Iron (Fe). The photocathodes were irradiated by a 450 fs laser pulses generated by the KrF excimer laser beam (248 nm=5 eV) using the previous experimental set-up of Fig. 2.1. The laser beam was focused onto the same point of the metallic cathode under an angle of incidence θ=80^o with a precision of 0.2^o, by a silica convex lens of 18.5 cm focal length at 248 nm. The distance between the lens and the photocathode was fixed at 17.5 cm in order to get a sufficiently large laser spot area 0.2 mm^2. As it was previously observed in various metals, the photoemission efficiency for s-polarized incidence radiation was always lower than for p-polarization. Thus only p-polarization data are considered for the experimental measurements of this section. The anode was charged up to 28 kV by means of a positive high voltage power supply, allowing a production of an accelerated electric field up to 6.6 MV/m. The photocurrent was measured for applied high voltage from 0 to 28 kV by increments of 4 kV, in order to avoid (if it is possible) the space charge effects in the electron collection from the anode.

Before photocurrent measurements, the cathodes were fully activated by irradiating it in situ for an hour and a half with 248 nm fs laser pulses transporting a energy fluence of about 0.5 mJ/cm^2. In same photocathodes like tungsten the cleaning process was controlled by measuring every minute the photocurrent produced by the laser pulse. As it is observed from Fig. 2.5, the photocurrent reach a maximum value in about 90 min and then fluctuate around it. Subsequently, the measurements were performed in the saturation area.

2.3.2 Experimental Results and Discussion

The photocurrent density as a function of the laser peak intensity of the p-polarized fs excimer (248 nm) beam, for various metals is presented in Figs. 2.6, 2.7, 2.8, 2.9, 2.10. All the data were deduced for measurements at incidence angle $\theta = 80^o$. For all the tested metals, the work function is less than the KrF laser photon. Then, the photoelectron emission is a single-photon process. On the other hand, it is clear, that the intensity dependent curves for

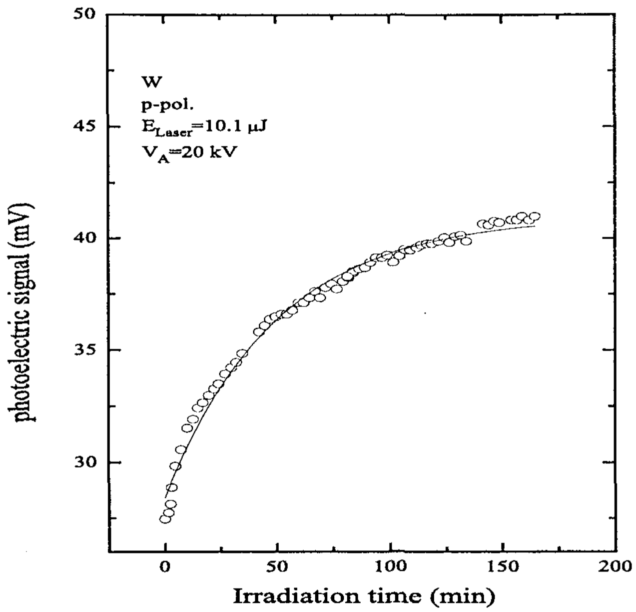

Figure 2.5: Photoelectric signal from tungsten vs the irradiation time using p-polarized UV (248 nm) laser pulses with energy 10.1 μJ, pulse duration 450 fs, angle of incidence $\theta = 77^o$ and applied voltage 20 kV. It is shown that the cleaning of the metallic surface as a function of irradiation time is a continuous process with a slow saturation temporal profile.

all the metals are nonlinear curves which is not expected in the perturbation theory analysis of the previous sections.

The higher non-linearity was observed for the Au and Cu. Also, the higher photoelectric sensitivity (photocurrent density divided by the laser intensity) was observed again for Au and Cu. The photoelectric sensitivities of W, Al and Fe are about 3 times less in the intensity range of a few GW/cm^2. These results are in agreement with other experimental results measured in the same conditions [Gir93, Gir94, Gir96].

In the following sections, the observed non-linearities as well as the appeared differences in the single-photon photoelectric sensitivities of the various metals are tried to be explained. Before the results analysis, we place beside, the theory of cathode heating. The electrons on the metallic surface, absorb the laser photon and many of them return to their equilibrium state with non-radiative decay, i.e., scattering with the other electrons and the lattice. This fact increases the electron temperature in the vicinity of the Fermi energy which affects the

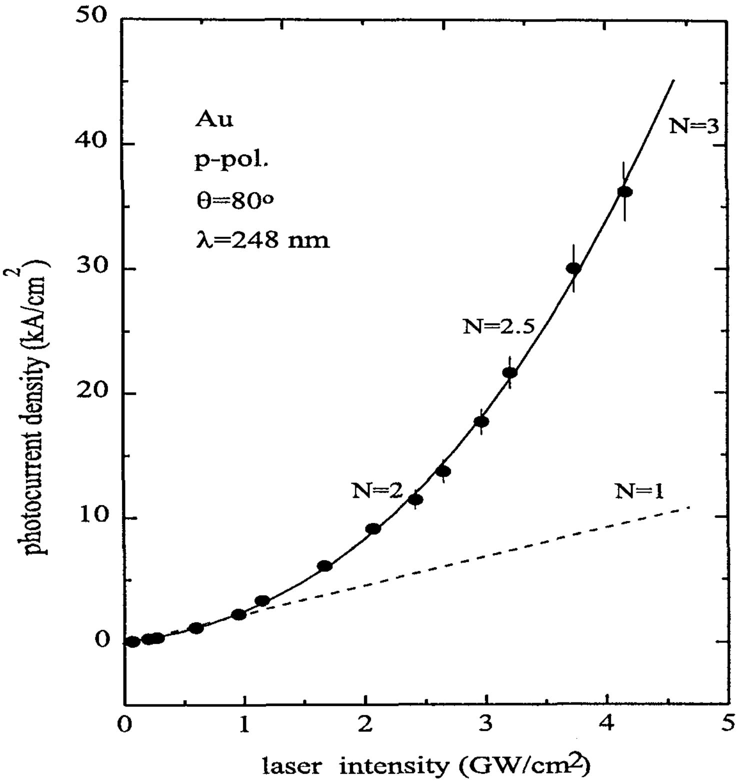

Figure 2.6: Photocurrent density produced by single-photon electron emission from a gold surface versus the laser intensity of the p-polarized incident pulse with duration 450 fs and photon energy 5 eV.

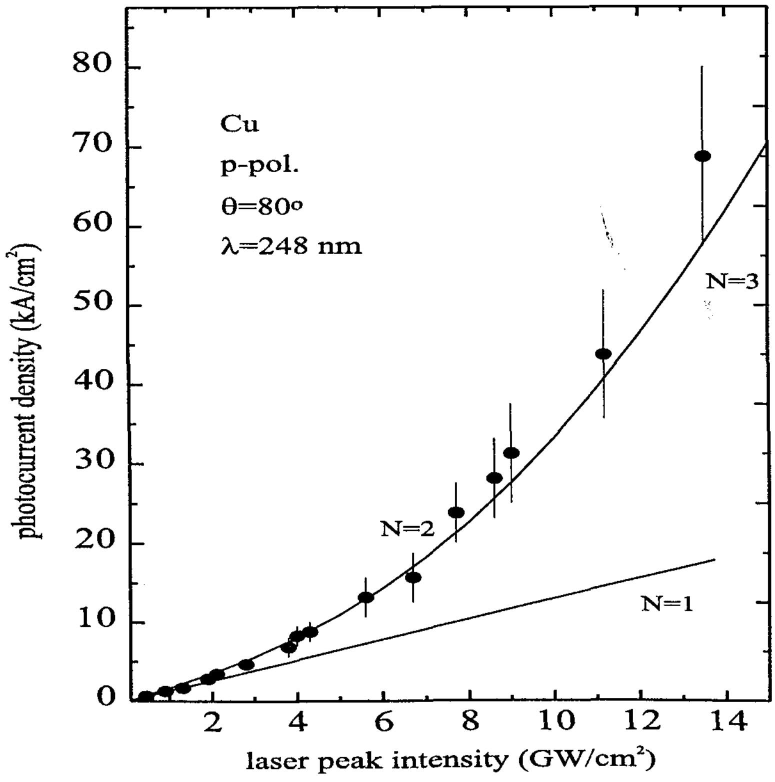

Figure 2.7: Same with Fig. 2.6 but for the copper.

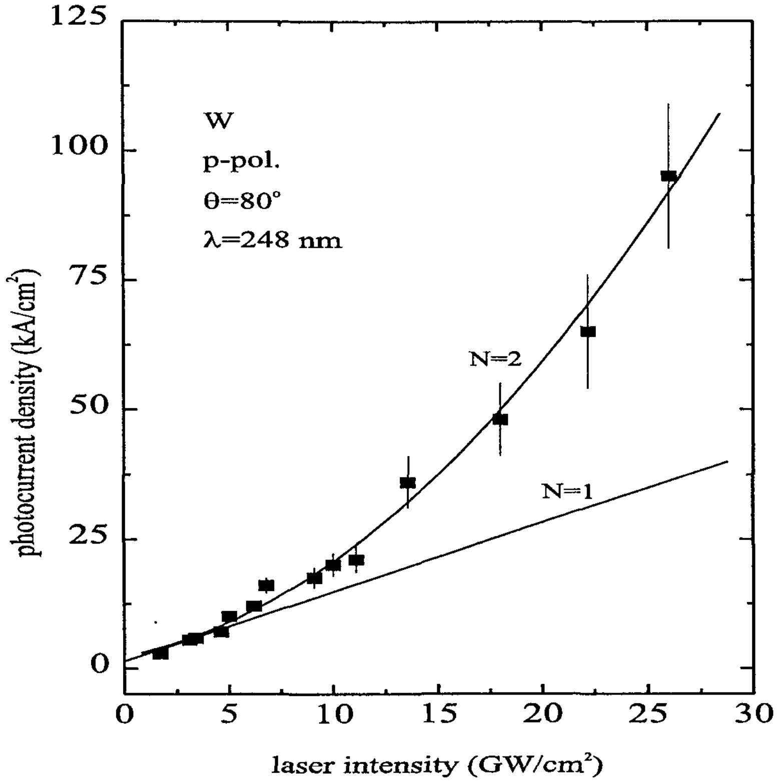

Figure 2.8: Same with Fig. 2.6 but for the tungsten.

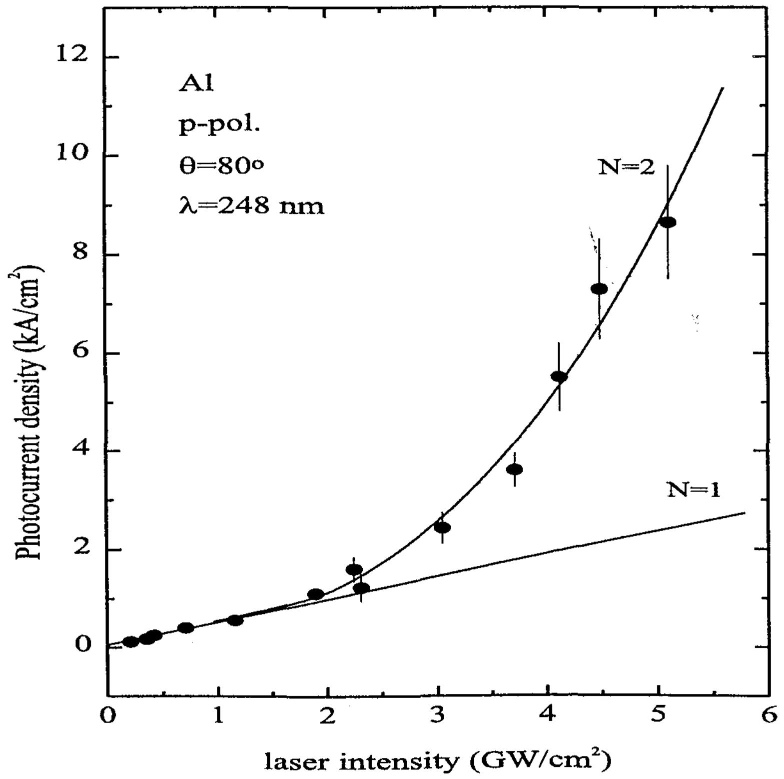

Figure 2.9: Same with Fig. 2.6 but for aluminium.

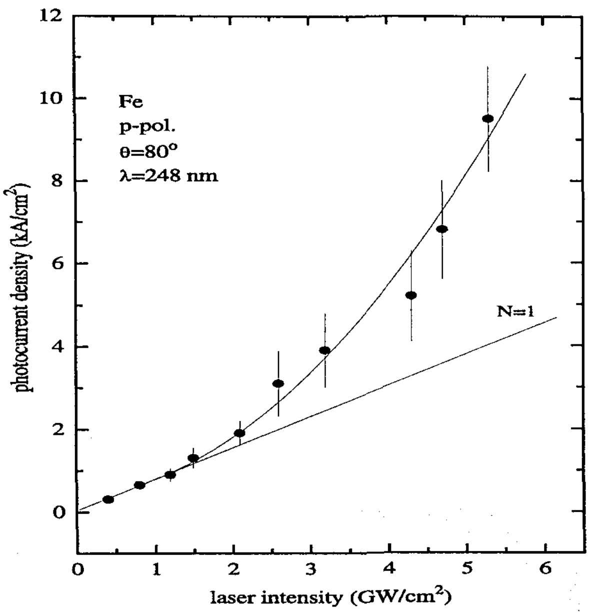

Figure 2.10: Same with Fig. 2.6 but for the iron.

yield of the electron photoemission. The electron gas heating follows a different process for laser pulses longer than few ps than for subps and fs ones.

2.3.3 Normal Heating, nanosecond Laser Pulses

Heating of the cathode by the laser radiation can be significant due to the high intensity needed for observing the multiphoton photoemission process. For a high enough cathode temperature, thermionic emission can in fact mask any multiphoton signal. Since the temperature rise of the cathode is essentially a linear function of the total energy deposited, the N-photon photoemission signal varies with the intensity of the pulse to the Nth power. In order to minimize the energy of the pulse and maximize the peak intensity, a short pulse duration is a prerequisite for any multi-photon photoemission experiment.

For ns laser pulses the electrons and the lattice of the metallic surface are at any time instant in thermal equilibrium with a common temperature T. The temperature spatial and temporal profile can be calculated by solving the heat diffusion equation [Bec75]:

$$\rho C \frac{\partial T(\vec{r},t)}{\partial t} - K\nabla^2 T(\vec{r},t) = G(\vec{r},t) \tag{2.9}$$

where $G(\vec{r},t)$ is the source term which is expressed for a Gaussian laser pulse, as:

$$G(\vec{r},t) = I_o(1-R)\alpha e^{-\alpha z} e^{-(r/\rho)^2} e^{-(t/\tau)^2} \tag{2.10}$$

where I_o is the incidence laser peak intensity, R is the metal surface reflectivity (see chapter 1), α is the absorption coefficient, i.e., the inverse of the penetration depth, ρ and τ are the FWHM laser beam spot size and pulse duration, respectively and K is the metal thermal conductivity. When the radial diffusion of heating is small compare to the characteristic radial dimension, i.e., $\sqrt{\frac{4Kt}{\rho C}} << \rho$, then the change in temperature is given by the solution of the 1-D heat diffusion Eq. (2.9) [Bec75].

Nevertheless, because the normal heating has been studied in details, in the work of Bechtel [Bec75], in our experimental studies, the ns pulses are used here to observe the pure multi-photon photodynamic effects.

From a microscopic point of view, the energy in the light wave is transferred to the metal in the following sequence. Photon energy is first transferred into electronic excitations, subsequently, these hot electrons come into thermal equilibrium with the lattice via phonon collisions. For laser pulses longer than the electron-phonon energy electron relaxation time (typically few ps), the electrons and the lattice obtain a common temperature before the end of the laser action. Especially, for the ns laser pulses, the thermal equilibrium between electrons and lattice take place after the absorption of the first photons of the relative long ns pulse. In the latter case the electrons are thermalized simultaneously with the lattice (normal heating).

In the following, we try to answer what happens when a subpicosend laser pulse is applied in a metallic surface.

2.3.4 Anomalous Heating

In the subpicosecond or femtosecond regime, where the laser pulse is shorter than the relaxation time of the conduction electrons, the electron gas and the lattice are described by different temperatures T_e and T_i. It has been proposed by Anisimov et al. [Ani74], that in the interaction of ultrashort laser pulses with metallic surfaces, the temperature of the electron subsystem is detached from that of the lattice subsystem and non-inertially follows the shape of the laser pulse.

The electron temperature reaches the lattice temperature after a certain time (electron energy relaxation). This time is depended on the characteristics of the metallic surface as well as on the laser pulse characteristics. The energy relaxation time is studied in details at chapter 4. Anisimov et. al. [Ani74] assumed local equilibrium between electron-gas and lattice at any time instant. They wrote down for first time the energy balance equations for the electrons and lattice of a metal, probed by a short laser pulses, in the form:

$$C_e\frac{\partial T_e}{\partial t} = \vec{\nabla}(K\vec{\nabla}T_e) - U(T_e, T_i) + G(\vec{r}, t), \tag{2.11}$$

$$C_i\frac{\partial T_i}{\partial t} = U(T_e, T_i), \tag{2.12}$$

where C_e and C_i are the electron and lattice heat capacities, $U(T_e, T_i)$ is the amount of energy per unit volume per unit time transferred by the electrons to the lattice, which is calculated by Kaganov et al., based on the approximation of the free-electron model of metal with a Dedye phonon spectrum [Kag57]. According to their theory and when $T_e > T_i > T_D$

$$U = \frac{\pi^2}{6}ms^2n\{\frac{1}{\tau_{e-ph}(T_e)} - \frac{1}{\tau_{e-ph}(T_i)}\} \tag{2.13}$$

where T_D is the Debye temperature, m is the electron mass, s is the sound velocity in the bulk of the metal, n is the electron density and $\tau_{e-ph}(T_e), \tau_{e-ph}(T_i)$ are the electron-phonon scattering times, i.e., the time of the free flight of electrons in the lattice, under the condition that the lattice and the electrons are in thermal equilibrium with temperature equal to T_e or T_i, respectively. K is the electron thermal conductivity which depends on the temperatures of both electrons and the lattice [Ashb76],

$$K = \frac{1}{3}u_F^2C_e\tau, \tag{2.14}$$

where u_F is the electron Fermi velocity and τ is the total electron scattering time with the other electrons and the lattice.

The total scattering rate of electrons, according to the Matthiessen's rule [Ashn76] within the relaxation time approximation, is the sum of the rates of the separate mechanisms:

$$\frac{1}{\tau} = \frac{1}{\tau_{e-e}} + \frac{1}{\tau_{e-ph}} \tag{2.15}$$

where τ_{e-ph} and τ_{e-e} are the electron-phonon and electron-electron scattering times, respectively. For $T_e > T_D$, τ is the same used in the theory of electrical conductivity.

According to Fermi-liquid-theory and the Thomas-Fermi screened potential [Ash76c], τ_{e-e} is given by the equation:

$$\tau_{e-e} = \frac{\hbar E_F}{A\prime k_B^2} \frac{1}{T_e^2} \tag{2.16}$$

where E_F is the Fermi energy of the metal, k_B is the Boltzmann constant, $\hbar$ is the Plank constant and $A\prime$ is a dimensionless number of the order of 1 to 10.

In the case of electron-phonon scattering the average energy loss, of the scattered electron, will be a phonon energy (few hundredth of an eV), because in such a collision, a creation or destruction of a photon may occur. The probability of phonon creation or destruction is proportional to the phonon population, since the latter depends on the lattice temperature in Bose-Einstein statistics, it is convenient to write that the electron-phonon scattering time depends on lattice temperature, T_i. It can be proved that [Har80]:

$$\tau_{e-ph} = \frac{\hbar}{2\pi k_B \lambda_b} \frac{1}{T_i}, \tag{2.17}$$

where λ_o is a dimensionless electron-phonon coupling constant characteristic of the metal and it is in the order of 0.1 to 1. Thus, we may write:

$$\tau_{e-ph} = \frac{1}{BT_i} \tag{2.18}$$

$$\tau_{e-e} = \frac{1}{AT_e^2}, \tag{2.19}$$

where A, B are constants dependent on the metal and are equal to:

$$A = \frac{A\prime k_B^2}{\hbar E_F} \tag{2.20}$$

$$B = \frac{2\pi k_B \lambda_o}{\hbar} \tag{2.21}$$

Using Eqs. (2.13) and (2.19) we get

$$U = \frac{\pi^2}{6} \frac{ms^2 n}{\tau_{e-ph}(T_i) T_i} (T_e - T_i) \tag{2.22}$$

Now, we define g as:

$$g \equiv \frac{\pi^2}{6} \frac{ms^2n}{\tau_{e-ph}(T_i)T_i} \tag{2.23}$$

the transferred power by the electron to the lattice per unit volume takes the form: $U = g(T_e - T_i)$, and since $\tau_{e-ph} = 1/BT_i$ we have finally:

$$g = \frac{\pi^2}{6} ms^2nB \tag{2.24}$$

After the previous analysis is clear that in order to calculate the electron and lattice temperatures in any time and space, one has to know the parameters A and B. The order of magnitude of the parameter A can be estimated by using theoretical and experimental data from the bibliography [Mac80, Kav84]. A is estimated to be in the range of 10^6 to $10^7 K^{-2}sec^{-1}$. The same order of magnitude may be calculated by the Eqs. (2.21) ($A\prime \approx 1 - 10$). Similar, the parameter B is calculated by Eqs. (2.21) to be in the order of $10^{11} K^{-1}sec^{-1}$ ($\lambda_o \approx 0.1 - 1$).

The exact values of A and B for any metal can be evaluated using autocorrelation data. This method is presented in chapter 4. Nevertheless, using the order of magnitude of the parameters A and B, the parameter g is calculated to be in the order of $10^{16} - 10^{17}\ Wm^{-3}K^{-1}$. Another more recent calculation based on a theory related to superconductivity [All87] expresses g as:

$$g = \frac{3\hbar\gamma_e\overline{\lambda} < \Omega^2 >}{\pi k_B^2} \tag{2.25}$$

where $\gamma_e = C_e/T_e$, $\overline{\lambda}$ is a kind of electron-phonon coupling constant used in superconductivity theories, $< \Omega^2 >$ is the second momentum of the phonon spectrum defined by McMillan [Mac67]. For the metals studied in our experiments, the g is calculated to be on the same order of magnitude with the earlier calculations.

The values of E_F, s, n, R, C_e, C_i could be found in the literature directly or calculated from simple laws. For example, C_i is calculated by the law of Dulong and Petit, i.e., $C_i = 3nk_B$; C_e is calculated by the Sommerfeld theory [Ash76] to be:

$$C_e = \frac{\pi^2}{2}(\frac{k_BT_e}{E_F})nk_B \tag{2.26}$$

The metal reflectance is calculated by the complex refractive index of every metal using (for p-polarized incidence light) the Eq. (1.30)

Using all the above parameters (the exact values of A, B, will be calculated in chapter 4), the electron temperature can be estimated numerically from the Eqs. (2.12). The general observation of the calculations for subps laser pulses are: The electron temperature follows in time almost non-inertially the rise part of the laser pulse. Few fs after the maximum of the laser pulse, the electron temperature reach its maximum value which is typically few thousands of K degree for the conditions of our experiments. After several hundreds fs (or few ps), the electron temperature reaches the lattice one (cooling time). This common temperature is relatively low (about room temperature) for laser intensities of the range of few GW/cm^2.

The lattice temperature, due to the high specific heat, changes very slowly and it reaches its maximum value (which is close to its initial value) when it reaches the electron temperature. Following, both electrons and lattice have a common temperature for several μs.

In the above analysis, it is assumed that the electrons thermalized instantaneously in to a Fermi-Dirac distribution. There is some recent works, e.g. the work of Fann et al. [Fan92], where by using a 270 fs laser pulse, a nascent distribution of the thermalized FD distribution in thin Au films was observed. However, the 450 fs laser pulses which was used in our experiments is relatively long compared to the electron-electron scattering time for electron temperatures up to a few thousands of Kelvin degrees, it can be assumed that the electrons are always in thermodynamic equilibrium and they can be continuously well described by the Fermi-Dirac statistics. A theoretical analysis for the possibility of non-thermal electrons is presented in chapter 4.

It is clear that as the laser intensity increases, heating of the Fermi electrons induces an increased occupancy of the electronic states at higher energies. This causes an enhancement of the electron emission by a thermally assisted process because more electrons are able to interact with the laser beam and finally escape from the metal. In this laser intensity region, where the temperature effects set-in together with the purely photodynamic effects there is not any quantum mechanical theory which takes in to account the dissipative optical processes in bound-bound transitions, which leads in electron heating of the Fermi electrons and calculates the photoemission current.

Thus, in order to describe the temperature dependence of the single-photon photoemission near the work function threshold, we use phenomenological theories. A satisfactory theory to do this is a theory of Fowler [Fow31], which was improved by Dubridge [Dub33], subsequently. Their starting point was the assumption that the electrons in the metal obey Fermi-Dirac statistics and are uniformly distributed in momentum space. The probability of absorption of a photon is independent of the initial state of the electrons. An electron may escape from the metal if its kinetic energy associated with the component of velocity normal to the surface is greater than the potential barrier. Also, all the energy of the absorbed laser photon, is used to increase the normal kinetic energy, and the velocity components parallel to the surface remain unchanged. Finally, the number of the electron emitted per absorbed photon is proportional to the number of electrons per unit volume of the metal whose normal kinetic energy when augment by $\hbar\ \omega$ is sufficient to escape the potential energy barrier. Then, the photocurrent density is expressed as:

$$J = \sigma \frac{I(1-R)}{\hbar\omega} \frac{2e}{h^3} \int_{-\infty}^{\infty} dp_x \int_{-\infty}^{\infty} dp_y \int_{p_{0z}}^{\infty} dp_z \frac{p_z/m}{e^{((p^2/2m)-E_F)/k_B T_e}+1} \tag{2.27}$$

where σ is proportional to the cross-section of the photoemission and is to be inferred from the experiment, I is the laser intensity, R is the metal reflectivity and p_{0z} is the minimum momentum (z-axes) that the electron in the metal must have, in order, after one-photon absorption its kinetic energy be greater from the potential energy barrier produced by ions. The integration of Eq. (2.27) can be performed and results in:

$$J = \sigma R_c(\frac{e}{\hbar\omega}) I(1-R) T_e^2 F(\frac{\hbar\omega - W}{k_B T_e}). \tag{2.28}$$

where $R_c = 4\pi m e k_B^2/h^3$ is the Richardson constant (120 $Acm^{-2}k^{-2}$). $F(x)$ is the Fowler function defined as:

$$F(x) = \int_0^{\infty} dy ln(1 + e^{-y+x}) \tag{2.29}$$

$$= \begin{array}{ll} \sum_{n=1}^{\infty}(-1)^{n+1}\frac{e^{nx}}{n^2} & \text{if } x < 0 \\ \frac{\pi}{12} & \text{if } x = 0 \\ \frac{\pi}{6} + \frac{x^2}{2} - \sum_{n=1}^{\infty}(-1)^{n+1}\frac{e^{-nx}}{n^2} & \text{if } x > 0 \end{array} \tag{2.30}$$

The Eq. (2.28) could explain the non-linearity observed experimentally for the various metals in the single-photon case.

In the low laser intensity region the electron temperature is constant and consequently the Fowler function is also constant. At this intensity region, the single-photon photoemission current density is depended linearly on the laser intensity. This is supported from the experiment shown Figs. 2.6, 2.7, 2.8, 2.9, 2.10. In order to explain the different non-linearities observed for the various metals is required to evaluate the exact values of the parameters A and B. If the values of A and B are known it is possible to calculate the electron-electron and electron-phonon scattering rates and consequently the exact temporal evolution of the electron temperature of the surface. The possible electron temperature difference for the various metals certainly explains in part why the Au and Cu have the maximum photoelectric sensitivity and non-linearity. This evaluation is presented in the chapter 4.

Chapter 3

Multiple Harmonic Generation from Metallic Surfaces

3.1 Historical Review

The generation of harmonics from metallic surfaces followed immediately the invention of the laser in the nineteen sixties. The first experiments [Bro65, Bro66], reported second harmonic generation on reflection from a silver mirror. They showed for the first time that the phenomenon has a surface origin. The second order polarization is proportional to the term $\vec{E}(\vec{\nabla}\vec{E})$. The main contribution from this term comes from the boundary due to the discontinuity there of the metal dielectric constant. Thus, the above term is known as the surface term.

On the contrary the term $\vec{E} \times \partial\vec{H}/\partial t$ is the bulk term, which originates from the Lorentz force on the electrons.

The intensity of the reflected harmonic wave is of course much smaller in centrosymmetric media compared to noncentrocymetric ones. The abrupt variation of the normal component of the electric field at the boundary takes place over a distance which is comparable to a unit cell dimension. Thus, it can be said that the surface effect comes only from the first atomic layer. This makes the observation of the effect still more dependent on surface conditions.

At about the same time, semiclassical theoretical treatments of Jha [Jha65, Jha65a, Jha66] appeared who showed for the first time the importance of the surface term by calculating classically and quantum mechanically the non-linear optical response of the free electron gas on a metallic surface. The classical book of Bloembergen [Blo65] summarizes and generalizes the nonlinear optical reflection of media.

During the next years, along with the ongoing theoretical discussions further experiments on gold, silver and their alloys by Bloembergen et al. [Blo66] appeared and several years later the work of Sonnerberg and Heffner [Son79]. The previous papers studied the effects of conduction and bound electrons on second harmonic generation and compared with the existing theories. The activity on the metallic harmonic generation in the sixties terminated with the classic paper of Bloembergen et al. [Blo68]. This paper derived general expressions for second harmonic generation in bulk media with inversion symmetry and applied them to a series of data on metals and semiconductors, showing an agreement between experiment and theory within a factor of two.

The early quantum theories of Jha were extended by Bower [Bow76] to include the effects of the interband transitions near their resonance as well as the effects of surface states.

3.2 Observation of Multiple Harmonic Generation from Metallic Surfaces

3.2.1 Introduction

High order harmonic generation has been extensively used for the production of coherent radiation in the ultraviolet and soft-xray region. In most of the cases a gaseous medium has been used [Fer88, Lom90, Hui91]. For intensities up to the threshold of the ionization, the electric field of an intense laser pulse can induce an unharmonic response in the electrons of gaseous atom leading to high harmonic generation, exhibiting spectacular characteristics: extremely wide spectra consisting of a high number of odd harmonics, with a wide plateau region terminated with a sharp cutoff.

These phenomena are governed by the fundamental laws of intense field Quantum Electro-Dynamics (QED), therefore the obvious question arises: Do these fundamental laws produce analogous phenomena for metals characterized by a rectangular surface potential well?

Additionally, metallic surfaces give the advantage that do not require ultra-high vacuum,

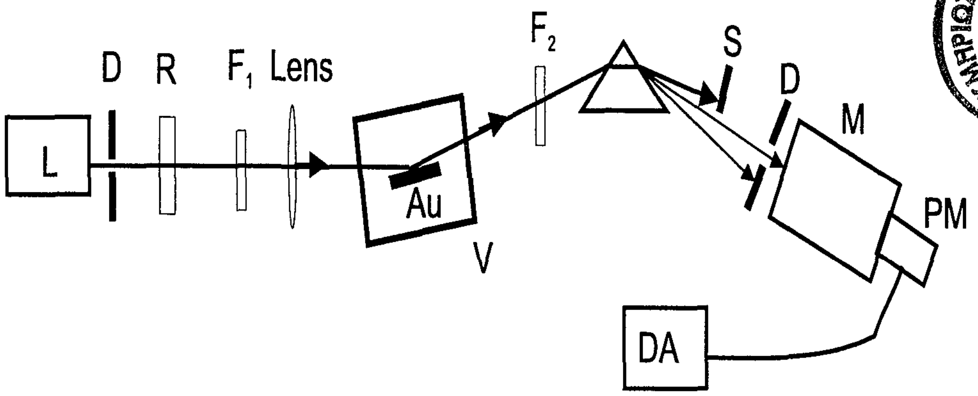

Figure 3.1: Experimental set-up for harmonic generation on metallic surface. L:Laser; R: polarization rotator; D: diaphragms; Au: polished gold metallic surface; V: vacuum vessel; P: quartz prism; S: fundamental beam stop; M: monochromator; PM: photomultiplier; DA: data acquisition system.

they are easily prepared and they withstand in the subpicosecond regime very high electric fields without suffering electrical breakdown. Also, the continuous wavelength tunability is expected.

3.2.2 Experiment 1: Nd-YAG laser

In our initial studies the high order harmonics (up to the fifth order, both odd and even) from a gold surface was observed [Far92]. Gold was chosen as an appropriate metal to realize the rectangular-model potential case; it is a monovalent metal $[Xe]4f^{14}5d^{10}6s^1$, and the energy between the full d-band and the E_F of the conduction band is 2.45 eV [Ros73].

The experimental arrangement is shown in Fig. 3.1. Linearly polarized, single, bandwidth-limited pulses were selected from the leading part of an actively mode-locked pulse train of a neodymium-doped yttrium aluminum garnet (Nd:YAG) laser (L) with pulse duration, $\approx$ 35 ps; intensity, 5 GW/cm^2 in the cross section of the beam; repetition rate 10 Hz; wavelength, 1064 nm. The light beam was directed through the slit (D) and a polarization rotator (R) onto the appropriately polished and treated surface of a 2-mm-thick polycrystalline gold sample (Au) kept under $\approx 10^{-7}$ torr in a vacuum vessel(V).

A grazing incidence of 70^o was used -at which the laser intensity was roughly $5\ cos(70^o) \approx$ 2 GW/cm^2 on the surface- to prevent heating and plasma effects and to favor the predicted surface excitations. The sample was prepared in the same traditional way as in all our previous multiphoton electron emission experiments. The reflected light passed through a quartz prism (P) which deviated and separated the direction of the different harmonics.

The fundamental high intensity laser light was blocked by the stop (S). Then by turning the prism (P) in the appropriate direction, the subsequent harmonic light components entered the slit (D) of a monochromator (M) (capable of measuring down to 200 nm) one by one and were detected by a photomultiplier (PM). The spectra was taken by the wavelength scan of the monochromator M, simultaneously rotating the prism into the appropriate direction. The most crucial disturbing effects which may occur in this type of experiment have been controlled and taken into account. For example the possible hazard lights which may be included in elements other than surface (diaphragms, windows, prism, e.t.a.) were filtered and completely eliminated by inserting different density color filters (F1, F2, F3) in appropriate combinations between the different elements of the set-up. A further similar control was done realizing the configuration in which the light beam passed the whole setup without touching the gold surface. The signal of the photomultiplier is analyzed by a data processing system (DA) containing a boxcar average and an acquisition and detecting setup.

In the following the experimental results are summarized. Figure 3.2 shows that the second, third, fourth and fifth harmonics, which were emitted in the speculary reflected laser beam in solid angles roughly equal to the 0.7 mrad laser divergence, appearing at the correct expected harmonic wavelengths, i.e., at 533, 355, 266 and 213 nm. The real relative values of the components were calculated taking into account the overall spectral response of the whole detection system. The spectral response is found using the known *black body* radiation spectra of a tungsten ribbon-lamp with horn-shaped bulb and measuring the response of the whole optical system at every wavelength emitted by the lamp.

The relative values of the observed harmonic generation yields are presented in Table 3.1. The appearances of the laser monitor pulses and those of the harmonic light pulses were simultaneous within the 5 ns time resolution of our detecting system. Special care was taken during the whole experiment to avoid any plasma formation on the surface by keeping the laser intensity value lower than 10 GW/cm^2 in the beam cross section, i.e., $I < 3GW/cm^2$ on the surface.

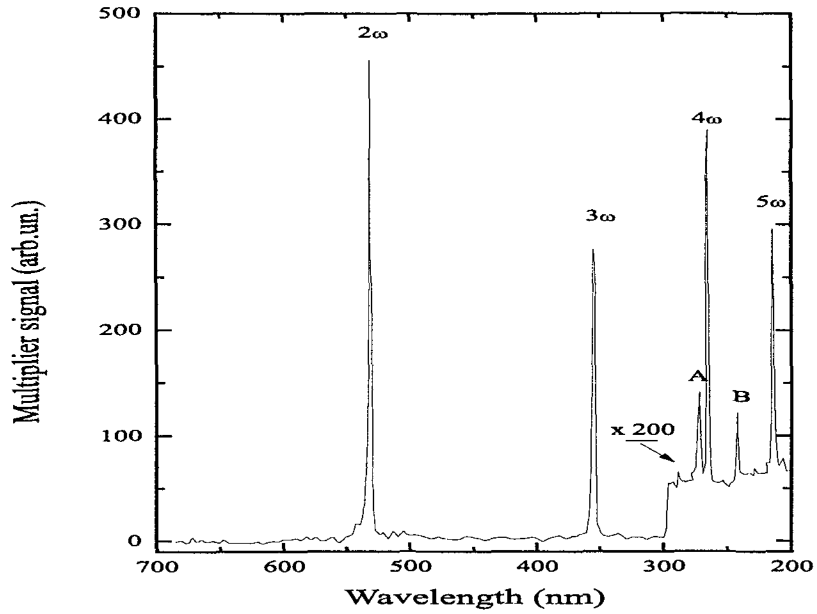

Figure 3.2: Spectra of the light emitted from the gold surface illuminated by picosecond Nd:YAG laser pulses with 5 GW/cm^2 intensity. The existence of second up to fifth harmonic, both odd and even is clear. There is an enhanced sensitivity in the wavelength region between 300 and 200 nm. The lines A and B corresponds to transitions of the neutral Au atom.

In contrast with other previous works, in which nanosecond pulses or long pulse trains of ps pulses were used (which may cause accumulation heating effects), the plasma creation threshold in our case was sufficiently increased by applying single, transform limited picosecond pulses.

As can be seen in Fig. 3.2, the second and the third harmonic lines appeared in a clear form, without any additional lines or considerable background in this part (700-300 nm) of

Harmonic order, n	n_{expt}	Expt.	[Mis91]	[Var94]	[Geo96]
2	1.8 ± 0.2	1	1	1	1
3	3.2 ± 0.2	5×10^{-1}	10^{-5}	10^{-1}	6.3×10^{-1}
4	4.1 ± 0.2	5×10^{-3}	10^{-8}	10^{-4}	3.6×10^{-3}
5	4.7 ± 0.5	10^{-3}	10^{-10}	10^{-3}	0.4×10^{-5}

Table 3.1: Experimental exponents of the power dependencies and relative intensities of the harmonic lines found experimentally by us and theoretically predicted by others.

the spectra. To detect the weaker fourth and fifth harmonics, we had to increase the detection sensitivity in the 300-200 nm spectral range. This is shown in the right side of Fig. 3.2, where we see the fourth and fifth harmonic lines in a somewhat increased harmonic noise level. Besides the harmonic lines, with less reproducibility, sharp additional lines appeared also in time coincidence with the laser pulse, only in this shorter wavelength spectral range (A and B in Fig. 3.2). They correspond to the $5d^{10}6p_{3/2} \rightarrow 5d^{10}6s_{1/2}$ and $5d^{9}6s_{5/2} \rightarrow 5d^{9}6s^{2}_{3/2}$ transitions of a neutral Au atom, as it was identified from table data.

In contrast to the appearance of similar additional lines in the noble-gas experiments [Fer88, Lom90], which are always performed in inherent plasma background, in our case any plasma process can be excluded as a possible origin.

Our experimental setup being roughly the same as that used in our multiphoton electron emission experiments, the absence of plasma and any surface damage may be routinely checked by observing the multi-photon photocurrent, which is sensitive to high order for any disturbing effects. In any case, the appearance of the weak A, B lines is irrelevant from the point of view of our original objective.

Unfortunately the observation of higher than fifth order was no possible with the monochromator available in this experiment.

The maximum harmonic signal was obtained at the p-polarization of the incoming laser light. The produced harmonic were always p-polarized. On the contrary, the light of the satellite lines was randomly polarized and thus one can say that the emitters are located outside of the metallic surface.

Measuring the yields of each harmonic as a function of the laser polarization we obtained an unambiguous proof that only the laser electric field component $E\perp(\omega)$, which is perpendicular to the gold surface causes the effect. This fact proves that the effect is predominantly of surface origin, i.e., it comes from the laser-induced non-linear current of the surface electrons [Blo68, Jha66, Jha65a].

The laser light polarization dependence curves for the second, third, fourth, fifth harmonic is measured by changing the angle ϕ between the laser field strength and the plane of

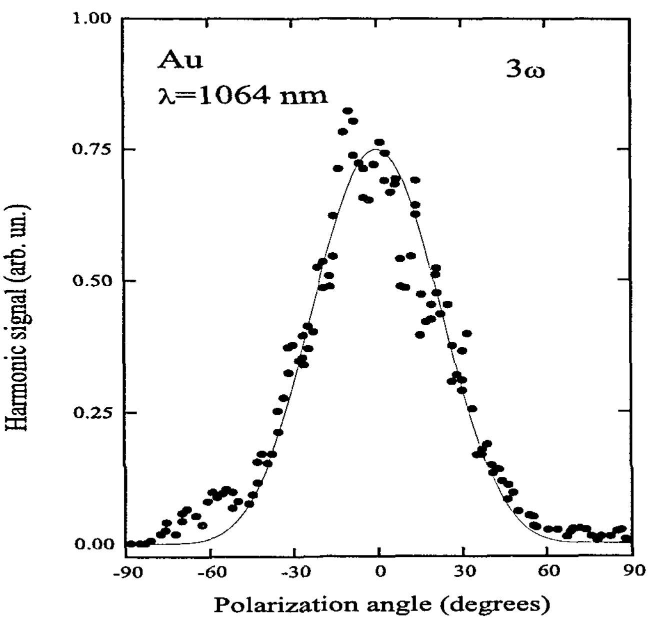

Figure 3.3: Third harmonic intensity dependence on the polarization angle, relative to the plane of incidence, $\phi = \pm 90^o$ correspond to the s-polarization; $\phi = 0^o$ corresponds to the p-polarization.

incidence. Figure 3.3 shows the polarization dependence curve of the third detected harmonic which agree with the expected $cos^{2n}\phi$ where n is the order of the harmonic (n=3). Similar results are obtained for all the detected harmonic up to 5. The fitted n is reported in the Table 3.1. correspondingly to the above harmonics. This polarization measurements furnished a basic control: In that geometrical configuration, in which the laser beam did not touch the gold surface, no effect was found.

From the polarization dependence it is estimated that the harmonic intensity $I(n\omega)$ depended on the incoming laser laser intensity $I(\omega) \approx |E(\omega)|^2$ in the form of the nth order power law, i.e., as $I(n\omega) = I^n(\omega)$. The polarization dependencies of the additional satellite lines were are also measured and exhibited stronger, $n_{expt} \approx 5 \pm 1$ values. The experimental data led to typical harmonic production efficiency of 10^{-10} for $n = 2$ at I $\approx$ 5 GW/cm^2.

3.2.3 Experiment 2: Nd-YLF laser

Other observations of harmonic generation from metallic surfaces took place using the fundamental beam of an Nd-YLF laser. The pulse duration of this laser was 2 ps and the wavelength was 1050 nm.

Using experimental set-up, similar to the previous one and metals prepared in the familiar way, the second harmonic of the fundamental beam from polycrystalline gold(Au), copper(Cu) and tungsten(W) was observed. The metals were kept in vacuum vessel under a 10^{-7} mbar pressure. The optical system was calibrated for the second harmonic light using the second harmonic generation in KDP doubling crystal.

The results are plotted on Fig. 3.4. The angle of laser incidence was $\theta = 72^o$. The laser was p-polarized relative to the metal surface. The polarization dependence of the second harmonic generation on Au, Cu and W was tested and shown the same behavior with the previous experiment, i.e., it follows the $cos^{2n}\phi$ law. Figure 3.4 shows that in the above conditions the Au yields more than one order of magnitude better second harmonic efficiency than W does and about three times more than Cu does.

Similar results were reported in chapter 2 for the electron emission of the previous metals. Gold yields a higher single-photon electron current than Cu and W, but the difference was not large compared to the electron emission case. Of course, in SHG the phenomenon is of second order and one may expect a higher difference.

In the next step we performed measurements of the yields of second and third harmonic generation from Au varying the vacuum in the vessel. The results are plotted in Fig. 3.5 The vacuum had no affect on harmonic generation. The latter result also confirms that the observed harmonics are produced by the electrons on the metal surface.

Subsequently, the third harmonic generation from the Au surface was studied. The intensity dependence curve is shown in Fig. 3.6 and shows clearly the 3rd order non-linearity. Similar results with the second harmonic are obtained from the vacuum dependence of the third harmonic generation. The third harmonic is not affected by the vacuum. The experiments could be performed in air.

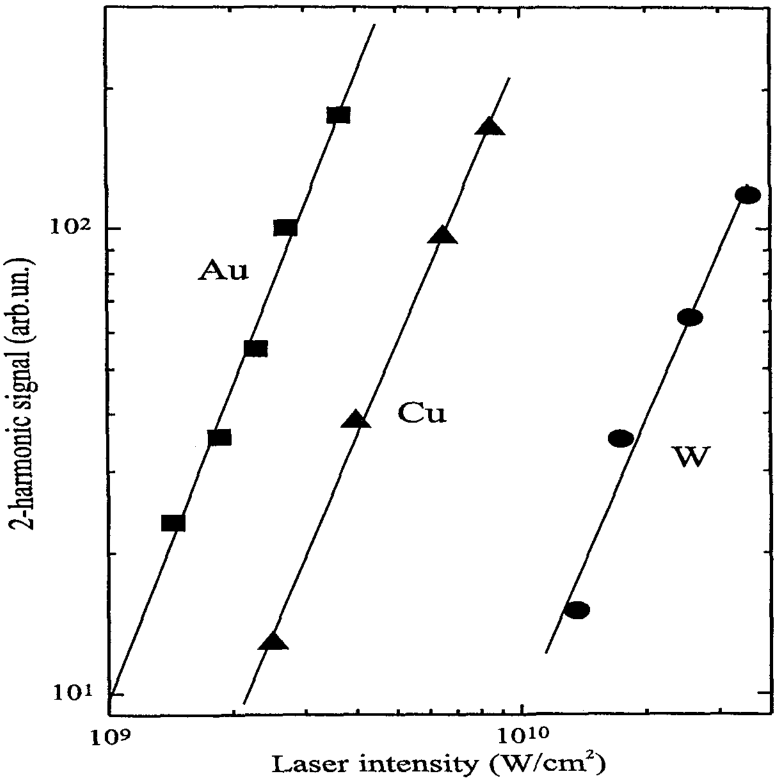

Figure 3.4: Averaged second harmonic generation yields for various metal as a function of intensity of the 2 ps Nd-Glass laser pulses. Gold has the higher second harmonic generation efficiency at this wavelength (1050 nm). Note that the solid lines are the best linear fits on the logarithmic scale with slope about 2 for all the metals. The maximum error in the data points is ± 10 %

The second harmonic generation efficiency ratio between Au and Cu was reported by Farkas et al. [Far94] using the 248 nm pulses of a subps KrF laser. The observed ratio in the harmonic generation efficiency between Au and Cu was about 3, which is in agreement with our observations and is explained using the perturbation parameter g_B [Brod77] for an ideal rectangular potential which is enhanced by a factor $\lambda/a_B(g_{new} = g_B \times (\lambda/a_B))$, where λ is the wavelength of the fundamental laser and a_B is a distance characteristic of the surface in the order of few Angstrom.

The third harmonic (350 nm) is observed only for the gold surface. The reason was the limit of the detection system available for this experiment, which has a limited sensitivity.

The relative yield ratio for third and second harmonic generation is 0.3±0.1 for 2 GW/cm^2, which is in agreement with our previous observation on Au using an Nd-YAG laser.

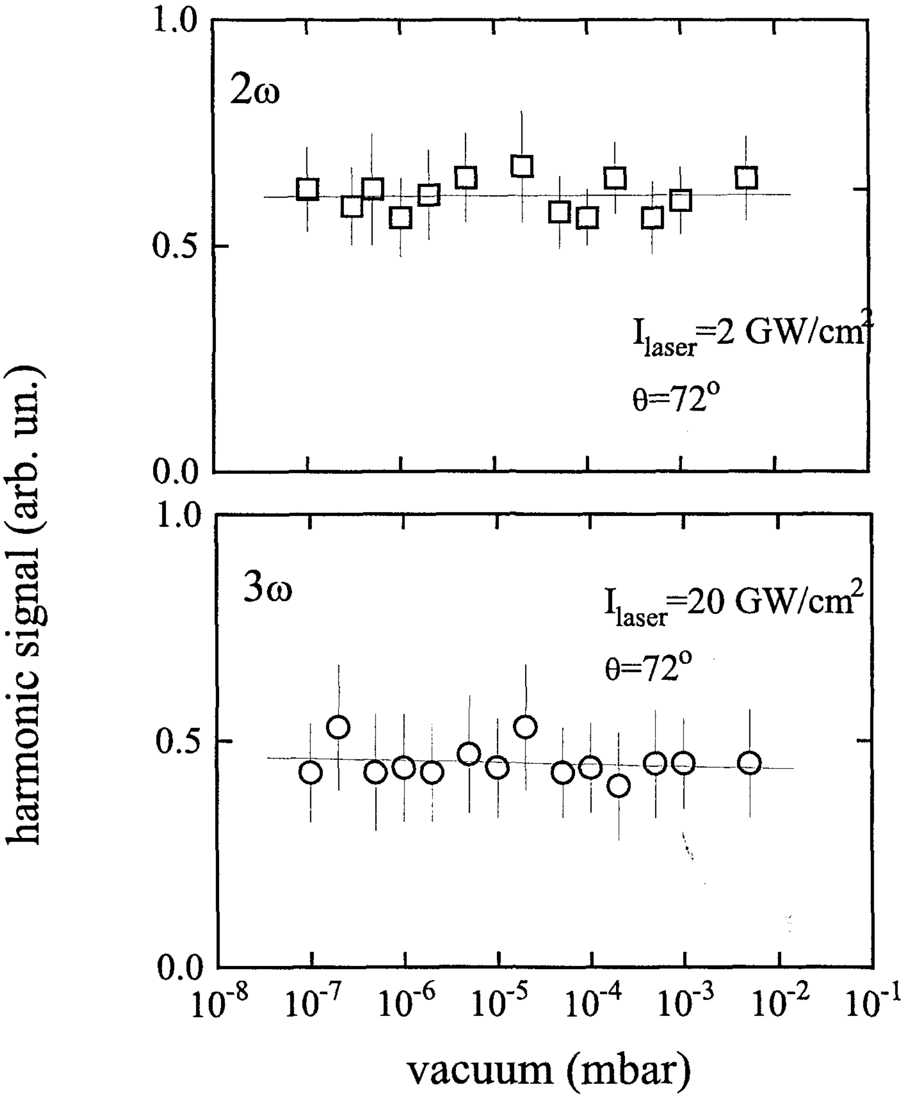

Figure 3.5: (a) Second harmonic generation from a gold surface as a function of the pressure of the vacuum vessel. Within the experimental errors, the second harmonic is not depended on the pressure in the cell. The laser was the Nd-Glass 2 ps duration at 1050 nm. This result also confirms that the harmonics are generated only on the metallic surface and not in the air-gases near the laser focal point. (b) Same with (a) but for the third harmonic situation.

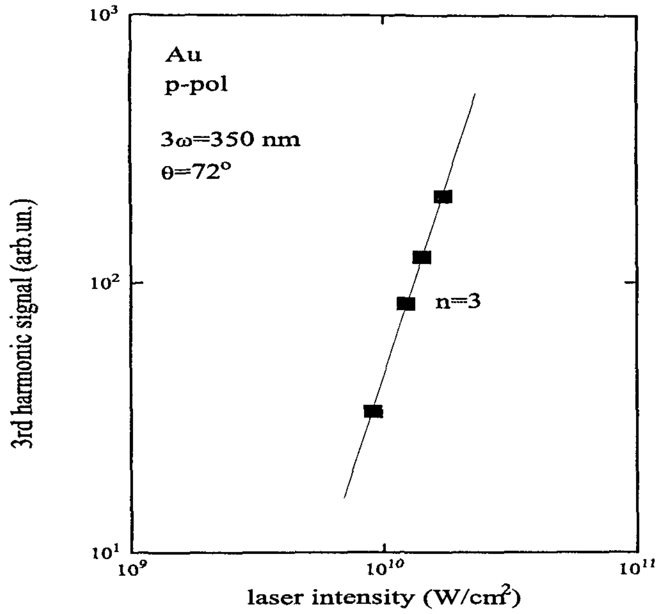

Figure 3.6: Third harmonic generation signal versus the laser intensity of the ps Nd-Glass laser pulses. The slope in the logarithmic scale is 2.98 ± 0.1.

3.2.4 Experiment 3: Ti:sapphire Laser

In this experiment a gold surface is illuminated by a Ti:sapphire laser. In the reflected direction the harmonic signals were observed. For the whole experiment presented in this section the laser pulse characteristics was kept constant: The pulse duration was 110±5 fs and the bandwidth of the laser beam spectra was about 7±0.3 nm with 790 nm central wavelength. The repetition rate of the laser was about 80 MHz. For this reason we used a chopper and a lock-in amplifier in order to measure the harmonic signals detected by the photomultiplier. The experimental set-up was similar to that of the previous harmonic generation experiments (Fig. 3.1) . A BBO crystal was again used for the calibration of the optical system for the second harmonic generation. A 248 nm excimer laser beam was used for the calibration of the optical system in the case of third harmonic generation.

Illuminating the gold surface -prepared with the traditional way- with the Ti:sapphire laser pulses we initial observed the second harmonic signals. Using combinations of various filters we ensured that the observed harmonic was produced on the gold surface. In this experiment the number of fundamental laser photons was kept constant by keeping the laser power to always at 1 W. Thus, the laser intensity per pulse after the focus on the gold surface is estimated to be 0.1 GW/cm^2 for the grazing incidence used in this experiment.

The angles of laser incidence, θ, which were used in this experiment were 56.2^0, 64.8^0, 70.4^o and 82.2^o. For all incidence angles we measured the second harmonic generation efficiency (number of second harmonic photons per number of fundamental laser photons) for the various polarization angles, ϕ. The angle $\phi = 0^o$ corresponds to p-polarization and $\phi = 90^o$ corresponds to s-polarization. The results are plotted in Fig. 3.7. It is clear that:

i) The second harmonic generation efficiency for the tested angles of laser incidence and for p-polarization is between 2×10^{-11} up to 2×10^{-10}. These values are in satisfactory agreement with most of the semiclassical theories as it will be discussed in the next section.

ii) For the various angles of laser incidence the second harmonic generation efficiency from gold surface shows again a strong p-polarization dependence, i.e., the phenomenon is a surface one.

In Fig 3.8 is plotted the second harmonic generation signal as a function of the laser incidence angle. The experimental data are in relative agreement with the theoretical predictions of Jha [Jha65a] despite the simplicity of the theoretical model which used only the plasma frequency of the metal and the laser wavelength as parameters for the calculations.

For the next step we tune the wavelength of monochromator in the vicinity of third harmonic. The third harmonic signal was detected using again a combination of suitable optical filters and a photomultiplier sensitive to the expected third harmonic wavelength, 263 nm. The calibration of the optical path of the third harmonic was done by the 248 nm of a KrF excimer laser. All the previous tests were performed to ensure that the third harmonic is produced on the gold surface.

The third harmonic signal exhibits a strong p-polarization dependence for the various angle of laser incidence as it is shown in Fig. 3.9. In the same figure the $cos^{2n}(\phi)$ functions are plotted. The value of n that fits the experimental value is n=3 for all angles of incidence

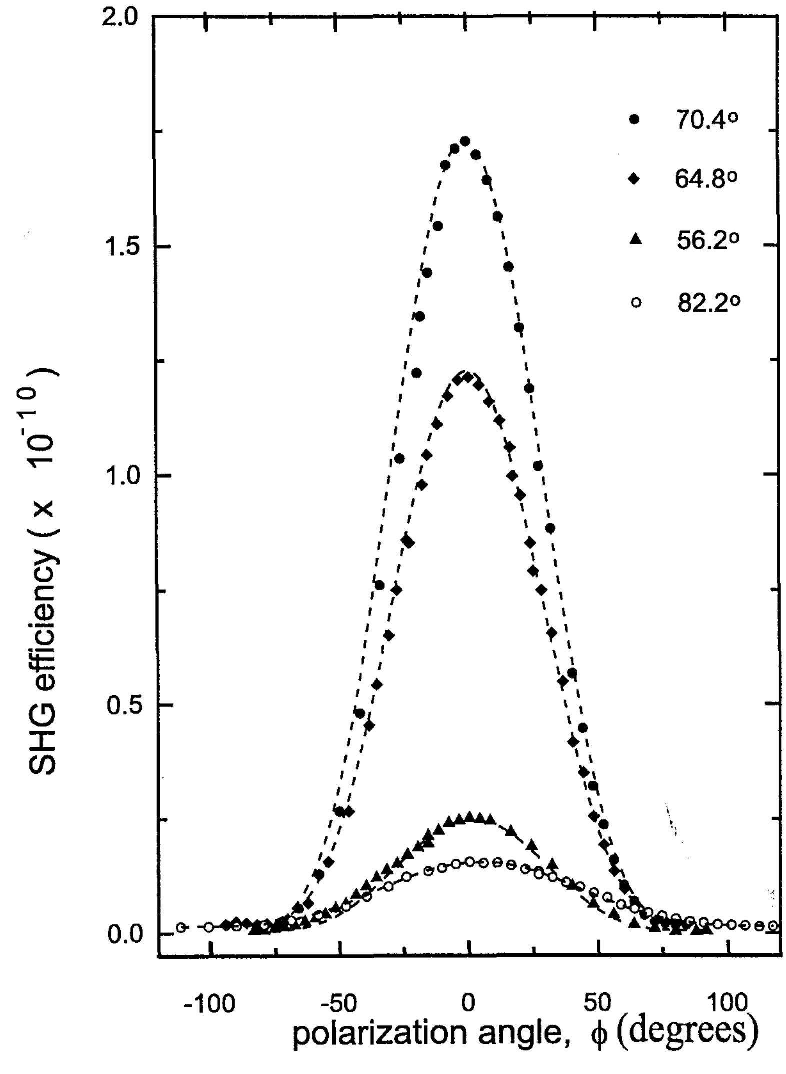

Figure 3.7: Second harmonic generation efficiency, versus the polarization angle (ϕ) for various angles of incidence (θ) of the Ti:sapphire laser pulses (100 fs, 790 nm), obtained from gold surface. The solid line represents the $cos^4\phi$ curves which show the p-polarization dependence of the harmonic generation as well as the second order of the phenomenon.

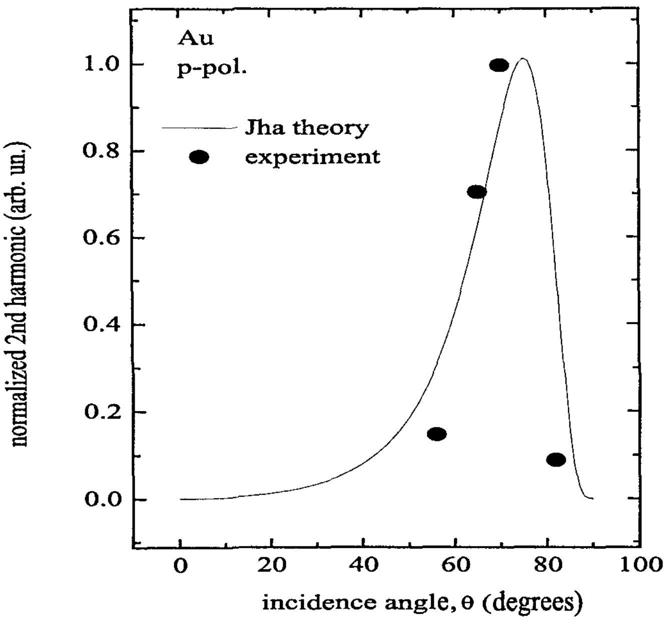

Figure 3.8: Second harmonic signal obtained from gold surface versus the angle of incidence of p-polarized Ti:sapphire laser pulses (110 fs, 790 nm). Dots represent the experimental measurements and the solid line the theoretical predictions of Jha [Jha65a].

which shows that the phenomenon is a pure photodynamic third order one. The third harmonic efficiency (number of third harmonic photons per number of fundamental laser photons) for a laser power of 1 W, i.e, intensity of about 100 MW/cm^2 is in the range of 5 $\times 10^{-13}$ up to 4$\times$10^{-12} for the range of laser angle of incidence used in this experiment. It should be noted here that the values of second and third harmonic efficiency have a maximum relative error of about 15 % which comes from the optical calibration of the detection system.

In the next step we had tried to observe the fourth harmonic generation with expected wavelength at 197.5 nm. Unfortunately it was not possible to detect the fourth harmonic signal. The reasons may be the very low expected efficiency as well as the wavelength limit of our detection system.

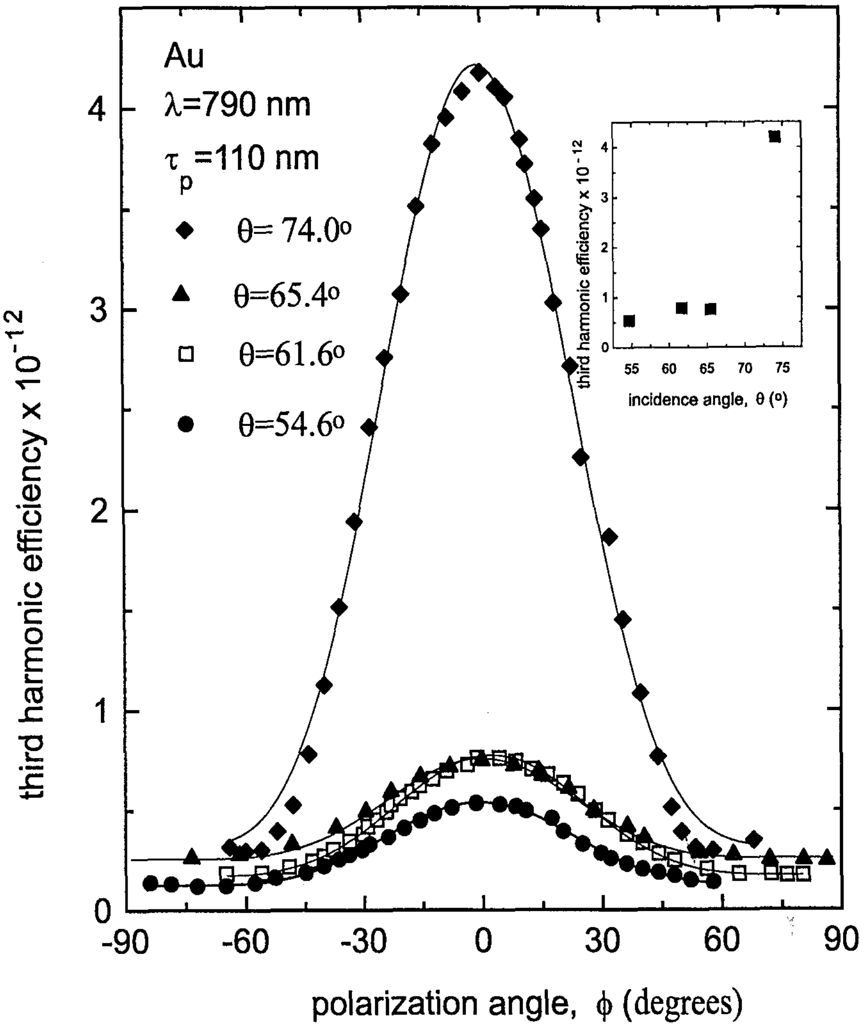

Figure 3.9: Third harmonic generation efficiency obtained from a gold surface versus the polarization angle, ϕ, of the 110 fs, 790 nm Ti:sapphire laser pulse for various incidence angles θ. The angle $\phi=0^o$ corresponds to p-polarization and $\phi=0^o$ corresponds to s-polarization. Inset: The dependence of the third harmonic generation efficiency vs. the θ for the $\phi=0^o$ case.

3.2.5 Comparison with Theories

The experimental results obtained cannot be compared directly to the most of the existing theories. The first class of them [Blo68, Jha66, Jha65, Jha65a, Bun65], i.e., the early semiclassical theories, are restricted to the determination of the characteristics of the low- (second- and rarely third-) order harmonic production only, but they use a very realistic, collective-electron model. They account for the basic features of our experiment: the polarization dependence, the laser intensity dependence, and the specular reflection of the harmonic light. Their $\approx 10^{-10}$ conversion efficiency value predicted for the n=2 agrees well with our measured experimental value for the second harmonic generation. Also, the predictions for the dependence of the second harmonic efficiency on the angle of laser incidence are in relatively good agreement with our experiments as it is shown in Fig. 3.8.

From this qualitative agreement, however, unambiguous conclusions cannot be drawn for the relative contributions connected with the surface or the bulk properties, the conduction or the interband valence electrons, the presence or the lack of the inversion symmetry.

Nevertheless, the observed higher-n-order polarization and power-law dependencies strongly suggest that the generalization of these low-order theories up to higher n-order is possible, similarly to the case of the atoms.

As for the non-perturbative theories [Mis91, Sac91, Sac89], at sufficiently low laser intensities they are equivalent with the second order perturbative calculations. Therefore for $n > 2$, these might be considered as the above-mentioned generalizations of the second order perturbative process (apart from the summation of the collective contributions of each individual electron). Although they are not capable by nature of accounting directly for the correct emission angle, our experiment verify their prediction for the possibility of production of all harmonics above the second up to the fifth. However, they predict a much stronger decrease of the efficiencies with the harmonic order n that found experimentally by us (see the right columns in Table 3.1). This fact seems to be surprising at first, being that the perturbative parameter x, defined in ref.[Mis91] is $x = 3 \times 10^{-3}$ in our experiment; i.e., we were in the perturbative range.

It is well known, however, that theories (elaborated especially for multiphoton electron emission from macroscopic metal surfaces using a modified perturbation parameter and based on the above-mentioned correct coherent summation [Sil71]) predict the breakdown of the perturbation approach at considerably lower (about 50 GW/cm^2) laser intensities. This was confirmed also experimentally. Therefore, a similar decrease of the upper limit of the validity region of the perturbation calculation cannot be excluded also in the case of the laser induced high-order harmonic generation process at metal surfaces.

Following our experimental work, two other theoretical treatments were appeared [Var94, Geo96]. Both describes the metal by the Sommerfeld free-electron model. The first one solves the Schrondinger equation of the problem perturbatively in the Kramers-Henneberger frame and derives a simple expression for the harmonic production. Relatively good agreement with our experiment is found in the relative peak spectral densities $I(n)/I(2)$. In this theory there is no reference to the absolute efficiency value of the second harmonic generation and for the emission angle of the harmonics. On the other hand this theory predicts that the width of the harmonic peaks to be in the order of $4kT_e$, where T_e is the electron temperature (experimental tests for this prediction are presented in the next sections).

The latest theory [Geo96] is based on an extension of the Sommerfeld model of the conduction electrons of metals that takes into account energy and momentum relaxation and consequently accounts for both coherent and incoherent excitations. Also, the theory accounts for the reflection and refraction of the light at the metal surface. Note that in previous theories [Var94] the incoherent components as well as the nonlinear Fresnel factors were not taken in account. The incoherent component dominates the coherent one for the higher harmonic order, while for the second harmonic they are comparable. The theory by Georges [Geo96] explains the relatively slow decrease of the conversion efficiency for the five harmonics obtained experimentally from gold using 5 GW/cm^2 intensity Nd-YAG laser pulses. Also it calculates the dependence of the total intensity of the first four harmonics on the angle of laser incidence, θ and gives theoretical values for the absolute efficiency of the second harmonic.

The basic idea is that the excitation is stepwise mainly for the harmonics n=3 up to

n=5. The values of the harmonic generation efficiencies calculated by the various theories in comparison with our experimental results are presented in Table 3.1.

However, as one can see from Table 3.1 for the fifth harmonic the theory [Geo96] calculates an efficiency which is about two order of magnitude lower than the experimental value. This may be attributed to collective electron excitation effects which are not taken into account in the theory.

3.3 Study of the tunability and coherence of second harmonic radiation produced by ultrashort dye laser pulses from gold surface

3.3.1 Introduction

As we have already confirmed experimentally, on metallic surfaces, both odd and even harmonics are produced and continuous wavelength tunability is expected. The absolute efficiency for harmonic generation on metallic surfaces has been the issue of several current studies.

The aim of the work presented in this section is to prove explicitly the tunability of second harmonic generation from a gold metallic surface, and in addition, to clarify the role of the pulse duration of the fundamental laser beam in harmonic generation processes at surfaces. The observation of higher order harmonic generation requires high intensity laser pulses. The short laser pulse duration is necessary to avoid thermal effects and plasma creation. Additionally, a critical parameter for the harmonic generation is the size of spatial interaction region between the laser pulse and the metallic surface, which is connected to the number of electrons oscillating in phase in the presence of laser beam.

Therefore the interaction is very sensitive to the laser coherence and is very critical for the efficiency of the harmonic generation, the phenomenon being a collective one. Consequently, more coherently driven electrons yield more harmonic generation.

3.3.2 Experiments and discussion

In our experiment the laser was an excimer pumped dye laser [Sza88] with wavelength tuned between 490-510 nm. The pulse duration was originally 450 fs in Full Width at Half Maximum (FWHM) of the Gaussian profile. By inserting an etalon in the dye laser arrangement, it was modified to 4.5 ps at FWHM of the Gaussian-like average envelope of the multi-peak structure (see chapter 5).

The experimental set-up was similar to that described in the previous section. Grazing incidence was used, from $\theta = 75^o$ to 81^o. The focusing of the laser beam on the target had the same geometry during the experiments. The laser intensity on the target was changed between 0.1 and 20 GW/cm^2. The reflected second harmonic light was detected using the same technique described in the previous sections. A BBO doubling crystal was used for the alignment and the calibration of the overall optical system.

Varying the direction of the input polarization relative to the surface normal by a double Fresnel-rhomb rotator, we measured the intensity of the generated second harmonic light. The experimental results, for a laser intensity at surface equal to 20 GW/cm^2, are reported in Fig. 3.10. The fitted curve is a $cos^{2n}\Phi$ (n=2) function, which shows the second order non-linear dependence of the harmonic signal versus the intensity of the p-polarized component of the input laser beam. This demonstrates that the effect is predominantly of surface origin and it arises from the laser induced non-linear current of surface electrons. [Blo68, Jha66, Jha65]. In all further experiments described below the p-polarization of the incident laser light was used.

In the next step we studied the tunability of second harmonic light production at the gold target surface. Varying the wavelength of the fundamental radiation from 490 to 510 nm, the wavelength of the second harmonic light changed correspondingly from 245 to 255 nm, Also, the yield of the second harmonic generation followed the intensity of the fundamental laser beam for the different wavelengths of the tuning curve (Fig. 3.11).

These results show, that one may effectively convert radiation from the visible to the UV or VUV wavelength regions, which might have practical importance from the point of view

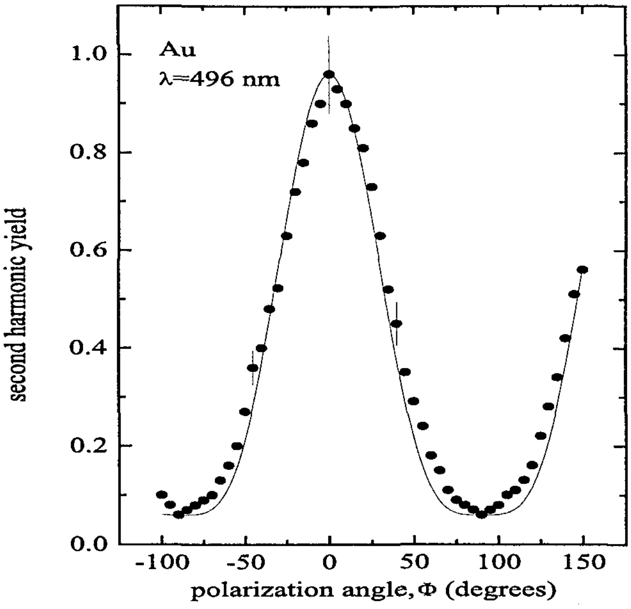

Figure 3.10: Dependence of the reflected second harmonic generation at Au surface on the polarization direction of the incoming laser light. $\Phi = 0^o$ corresponds to p-polarization and $\Phi = 90^o$ corresponds to s-polarization. The function $cos^4\Phi$ fit the experimental data.

of UV and VUV laser spectroscopy.

In the course of the preliminary experiments we observed that harmonic generation efficiency strongly depends on the duration of the inducing pulse and it varies weakly with the angle of incidence.

Supposing that these two features have a common origin, the obvious next step was to perform a systematic study changing both the angle of incidence and the pulse duration of the fundamental radiation. We used pulse duration values of 450 fs and 4.5 ps. As it is shown in Fig. 3.12, the second harmonic signal for 4.5 ps fundamental laser pulse was higher than for 450 fs duration one, at each angle of incidence.

This experimental observation shows the importance of the dimension of the interaction region between the actually illuminated area of the metallic surface and the laser beam. The possible explanation for the observed change of the efficiency difference between 450 fs and 4.5 ps laser pulses and for the different applied angles is the following: Being the harmonic

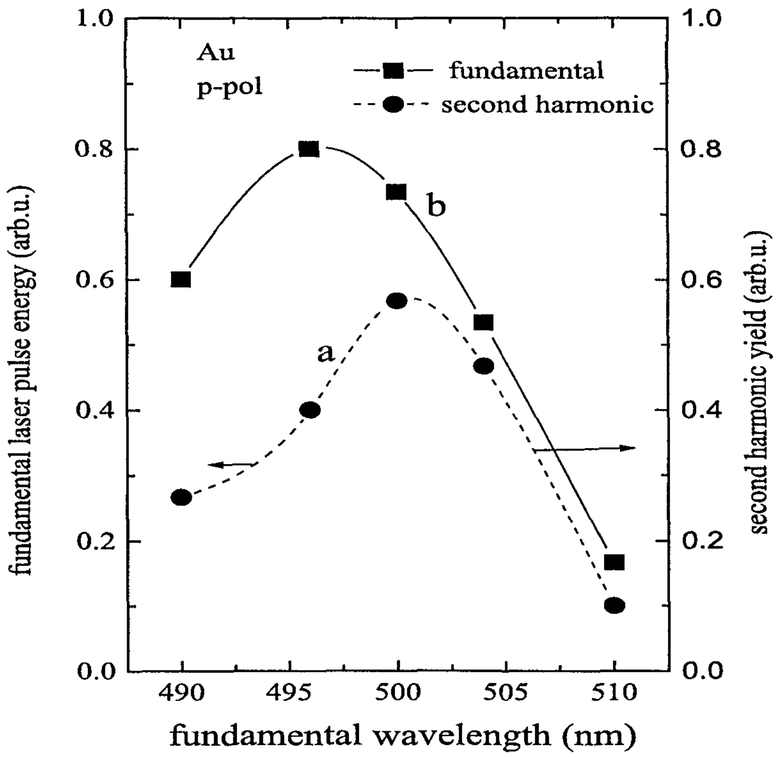

Figure 3.11: Second harmonic yield (curve a) at different wavelengths of the fundamental laser pulse together with the pulse energy changes of the fundamental (curve b).

generation a collective effect, the more the electrons move in phase in the actual presence of electromagnetic field of the laser, the higher the harmonic efficiency. When we illuminated the metallic surface by a laser pulse at grazing angle of incidence, the total illuminated area by the laser on the metal surface is smaller, equal or larger than that covered by the geometrical borders of the laser beam pulse at a certain time instant.

For example, the 450 fs laser pulse has a spatial length (d) of d=0.135 mm in the propagation direction, while the 4.5 ps pulse corresponds to d=1.35 mm. The spatial borders of the laser pulse on the metallic surface are different for each angle: the width of the running strip is $d/sin(\theta)$, where θ is the angle of incidence. Thus, for θ=75.1°, 77.7°, 80.1° the spatial limits of 450 fs are 0.1395 mm, 0.1382 mm, 0.1370 mm, respectively, while for the 4.5 ps pulse are for any case ten times larger. However, the whole length of the time-integrated illuminated area can be simple calculated by $D/cos(\theta)$, where D is the beam diameter in the cross section of the incoming laser beam at the target surface.

In our case these values are 0.93 mm, 1.13 mm, 1.40 mm for the above angles of incidence,

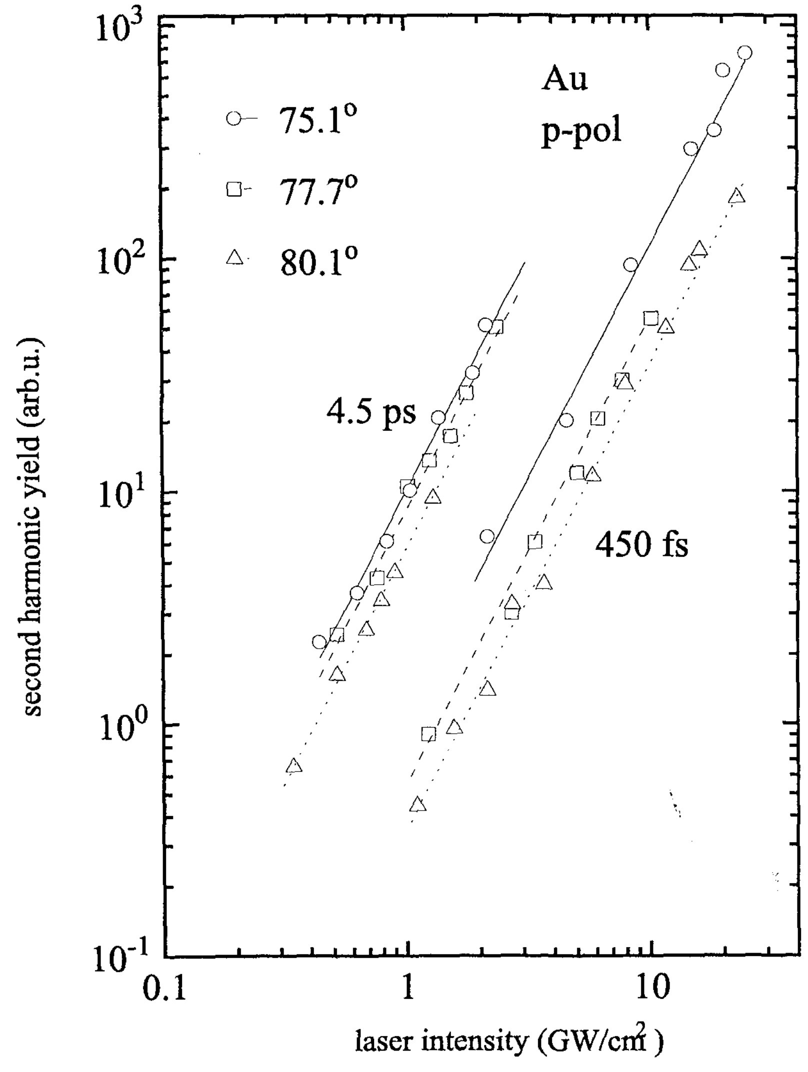

Figure 3.12: Pulse duration dependence of second harmonic generation at Au surface in the intensity range of 0.5 to 20 GW/cm^2. Dots represent the experimental data and solid lines the best fit linear curves with slope equal to 2 on the logarithmic scale.

respectively. Comparing these figures to the previously calculated widths of the running strips, it is obvious that in the case of a 4.5 ps laser pulse the total illuminated area is smaller than the laser pulse length for the cases of θ=75.1° and 77.7° and especially much smaller in the case of 75.1°. For these cases the number of electrons illuminated coherently by the laser pulse are smaller than could be expected considering only the pulse duration of the laser, so the number of the produced harmonic photons will be smaller. This fact seems to be supported by the experimental observations as represented in Fig. 3.12.

The linear curves of the second harmonic generation yields (with the correct logarithmic slope values of 2) for the case of 4.5 ps and the incidence angles 75.1°, 77.7° are more close than in the case of 450 fs for the same angles. Thus, we may conclude that in a metallic surface area illuminated coherently by a laser pulse, a coherent excitation of electron gas is expected. The harmonics generated by the individual electrons are constructively summed in the reflected direction. Furthermore, we may observe that the ratio of the efficiencies for the two different laser pulse durations (efficiency for the long pulse / efficiency for the short pulse) is decreasing when the angle of incidence (θ) is decreasing.

In the limiting case of the perpendicular incidence (θ=0°) one can expect identical efficiencies for both pulse durations (ratio=1), because in this case all the laser spot area is coherently illuminated for both cases.

The absolute quantum efficiency for the second harmonic generation at the metallic target (number of second harmonic photons per number of fundamental laser photons that arrive on the metallic surface) was measured by comparison to calibrated second harmonic generation in a BBO crystal. The calibration was made by the familiar method of application of the series of neutral density filters, energymeter and a photomultiplier.

The estimated absolute quantum efficiency turned out to be about 10^{-9} at 20 GW/cm^2 intensity of fundamental beam, for 450 fs laser pulses. This value is in relatively good agreement with most of the theories [Blo68, Jha66, Jha65, Mis91, Var94, Geo96] predicting second harmonic generation efficiencies in the range of 10^{-10}-10^{-9} at 10-20 GW/cm^2 intensities.

3.3.3 Conclusion

In summary, we demonstrated laser induced second harmonic generation from a metallic surface with predominantly surface character. The laser intensity dependence of the second harmonic signal showed a second order power law character, the form of the polarization dependence followed the $cos^{2n}\Phi$ (n=2) law around the p-polarization direction. Wavelength tuning was possible for the second harmonic generation. The efficiency of the second harmonic generation was higher in the case 4.5 ps laser pulses than at 450 fs in the intensity range of 0.1 to 20 GW/cm^2.

Based on the detailed comparison of the obtained second harmonic efficiency values at various pulse durations and angle of incidence we concluded, that for the practical efficient harmonic generation from metal surfaces one has to use "short" enough pulse duration to avoid the plasma creation, but at the same time "long" enough to have sufficient coherent interaction region.

3.4 Influence of the Electron Temperature in the Second Harmonic Radiation Produced by Ultrashort Dye Laser Pulses on a Gold Surface

3.4.1 Introduction

As it has been already mentioned in chapter 2, in single- and multi-photon electron photoemission from metallic surfaces, a positive deviation of the n-power law is observed, when subpicosecond laser pulses of few GW/cm^2 intensity are employed. The origin of this higher efficiency is attributed to the thermal non-equilibrium between the electron gas and lattice temperatures. The electron and lattice temperatures are described by the coupled heat diffusion Eqs. (2.12) [Ani74, Kag57, Fuj84, Gir95]. We solve numerically these equations, for a gold surface and for laser pulse intensities varying from 1 up to 50 GW/cm^2. Considering a Gaussian laser pulse temporal profile having a FWHM of 450 fs, a high electron temperature up to 3200 K (mean value during the presence of laser beam) is obtained. Electron energy relaxation occurs in the lattice after 0.7 ps up to 1.3 ps respectively to the above laser intensities. These values are in agreement with the measured electron energy relaxation time by Elsayed-Ali et al.[Els91] using thermoreflectivity measurements on polycrystalline and thick (80 nm) gold film at similar laser intensities. Thus, as the laser intensity increases, the heating of the Fermi electrons induces an increased occupancy at higher energies. This causes an enhancement of the electron photo-emission because more electrons are able to interact with the laser photons and finally escape from the metal [Yen80].

The fundamental question is: what is the effect of the high electron temperatures, produced by subpicosecond laser pulses, in the efficiency of the Second Harmonic Generation (S.H.G.) on the metallic surface?

3.4.2 Experiment 1

The experimental arrangement is the same used in our previous work for harmonic generation (Fig. 3.1). A 2-mm-thick polycrystalline mirror-like gold sample is irradiated by 450 fs duration excimer pumped dye laser pulses (496 nm) at grazing incidence (θ=77.7°). The sample is kept under a 5×10^{-8} mbar in a vacuum vessel. The laser system consists of an excimer laser and an ultrashort dye laser system. The laser beam from the XeCl cavity of the excimer laser is used to pump a sequence of dye lasers that provide the subpicosecond green laser pulse at 496 nm wavelength

Diagnostics are performed using a 1 m Littrow type spectrograph and a multiple shot autocorrelation at 496 nm by means of a non-linear crystal (BBO).

As previously observed, the harmonic generation efficiency from metallic surfaces is maximum for the p-polarization of the fundamental laser beam. Thus, the laser beam is kept in the p-polarization arrangement for the whole experiment. The second harmonic radiation is observed only in the direction of the reflected fundamental and in a solid angle roughly equal to the fundamental laser divergence. A BBO crystal is used for the alignment and calibration of the whole optical system. The reflected light is analyzed by a quartz prism and then, using a monochromator, the second harmonic light is detected by a photomultiplier. Similar controls as in our previous work are applied to ensure that the detected second harmonic light is generated by the gold surface. The second harmonic line appeared in a clear form without any additional lines or considerable background in the part 900 nm to 200 nm of the spectra. The absence of any emission, except the second harmonic and the reflected fundamental, confirms that there is no damage related to plasma formation on the metal surface. All previous tests are performed for the whole range of the laser intensities used in this work.

3.4.3 Results

Figure 3.13 shows the second harmonic yield versus the laser intensity. As we observe, up to about 25 GW/cm^2 laser pulse intensity, the experimental points agree with the well known power law ($I_{2\omega} \propto I_{\omega}^2$). The absolute efficiency for the second harmonic generation is measured by comparison to calibrated second harmonic generation in the BBO crystal and is found to be 10^{-10} for the laser intensity of 20 GW/cm^2.

On the contrary, when the laser intensity exceeds 25 GW/cm^2, a non-linearity higher than 2 is observed, i.e., for 48 GW/cm^2 laser intensity the second harmonic yield is 4 times higher than the expected from the n=2 non-linearity (Fig. 3.13). It should be noted here that the laser damage threshold of a metallic surface using subpicosecond laser pulses is higher than 100 GW/cm^2 [Fuj84, Gir95, She89, Wan94]. This is also confirmed by our experimental observations of the photoelectron emission from metallic surfaces using subpicosecond laser pulses.

3.4.4 Experiment 2

Complementary experimental evidence for the deviation from the second order non-linearity is established using an autocorrelation system for the fundamental laser beam and measuring the peak to background ratio of the second harmonic autocorrelation curve. The autocorrelator system is a Michelson type interferometer, in which, the incidence laser beam is separated in two parts by a 50-50 beam splitter. One of the two pulses is delayed or advanced with respect to the other, through an optical delay line with micrometric resolution. Then, the two beams are joined collinearly and focused on the same point of the gold surface under an angle of incidence θ=77.7^o.

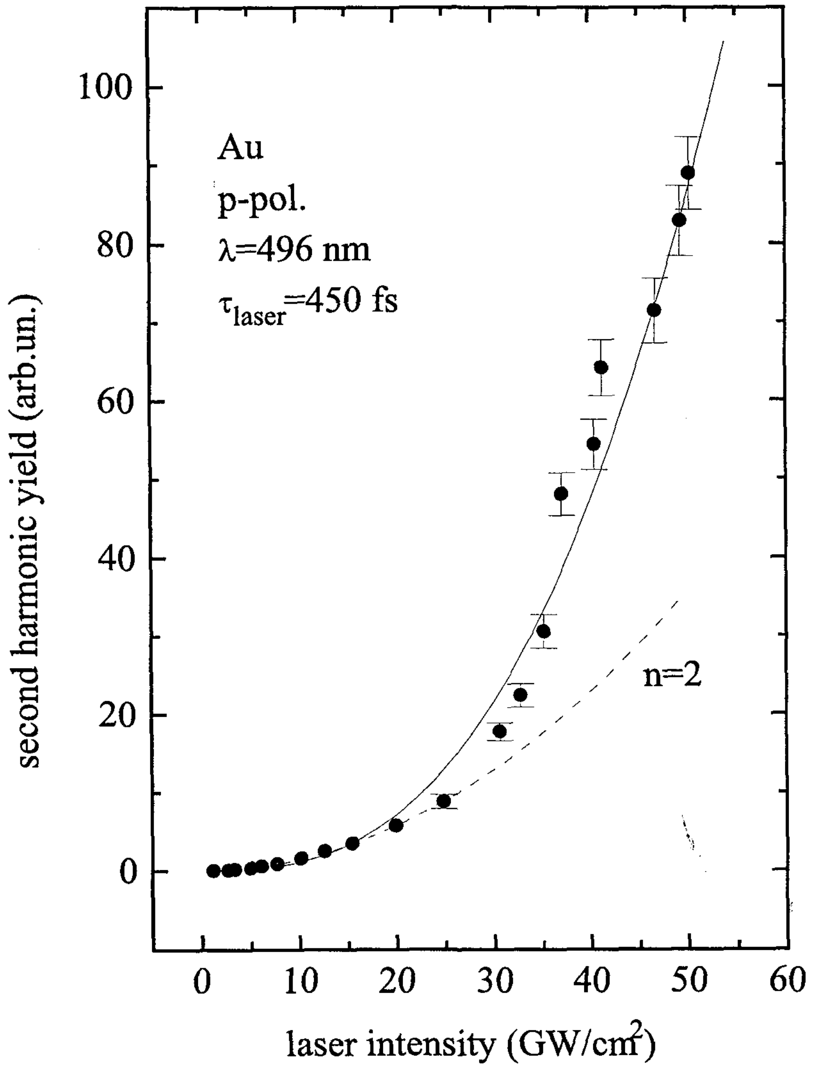

Figure 3.13: Second harmonic yield obtained by a gold surface as a function of the p-polarized fundamental laser pulse intensity. The dots correspond to the experimental measurements, the solid line to the theoretical model and the dashed line is the best square fitting up to 25 GW/cm^2. For laser pulse intensities lower than 25 GW/cm^2, the experimental data agree well with the n=2 non-linear curve, while for intensities that exceed 25 GW/cm^2 a higher than 2 non-linearity is observed.

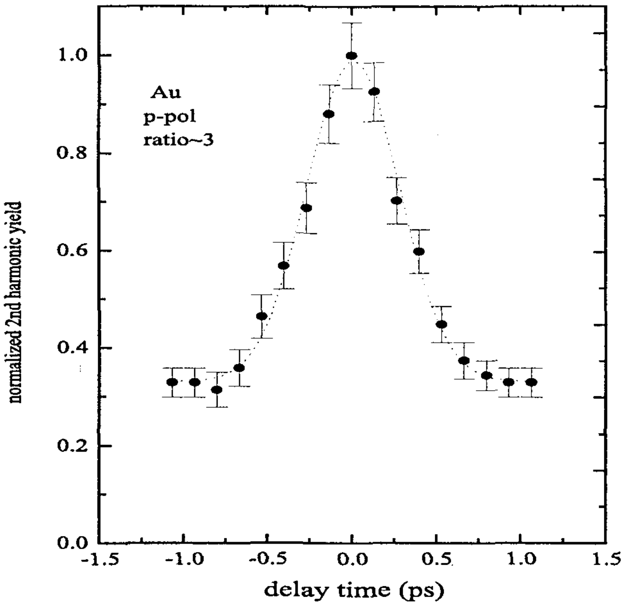

Figure 3.14: Normalized to the maximum, harmonic light yield, obtained by a gold surface, versus the time delay between the two fundamental p-polarized collinear laser pulses. The total intensity of the fundamental laser pulses at zero delay is 10 GW/cm^2 and the angle of incidence is 77.7°. The experimental autocorrelation points are fitted well to a Gaussian with FWHM equal to (630 ± 20) fs.

The reflected second harmonic light, produced by both laser pulses, is analyzed and detected using the experimental system described previously.

3.4.5 Results and Discussion

Figure 3.14 reports the harmonic generation yield versus the delay time between the two laser pulses for 10 GW/cm^2 total laser intensity at zero delay. The fundamental laser pulse has a Gaussian temporal profile. Thus, the second order autocorrelation curve can be fitted to a Gaussian. The peak to background ratio for the above curve is 3:1, which is exactly the expected contrast ratio for a second order, slow-term-measure autocorrelation curve [Sal80].

The expression for the second order autocorrelation curve, i.e., second harmonic intensity as a function of the delay between the fundamental laser pulses is:

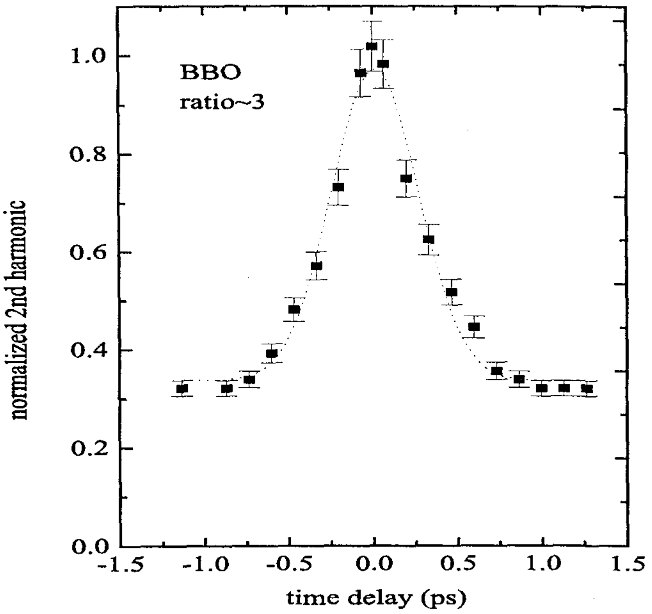

Figure 3.15: Same as Fig. 3.14 but the harmonic light obtained by a BBO crystal. The contrast ratio is 3:1 and the FWHM of the Gaussian is (630 ± 20) fs.

$$I_{2\omega}(\tau) \propto \frac{\overline{I_\omega^2(t)} + \overline{I_\omega^2(t-\tau)} + 4\overline{I_\omega(t)I_\omega(t-\tau)}}{\overline{I_\omega^2(t)} + \overline{I_\omega^2(t-\tau)}} \tag{3.1}$$

where the overline denotes averaging over the real time t, τ is the time delay between the two laser pulses of the autocorrelator and I_ω, $I_{2\omega}$ are the fundamental and the second harmonic intensities, respectively.

Note that, in the slow term autocorrelation function, all information regarding the phase relationships is lost as a consequence of the failure to resolve the much faster optical frequency variations [Sal80]. The Full Width at Half Maximum (FWHM), of the Gaussian autocorrelation curve in Fig. 3.14 divided by $\sqrt{2}$, is the time duration of the fundamental (496 nm) laser pulse [Sal80]. Thus, the 496 nm laser pulse has a duration equal to (452 ± 14) fs. This is exactly the pulse duration of the 496 nm laser pulse, measured by the classical way of autocorrelation, using the second harmonic generation in a BBO doubling crystal (see Fig. 3.15).

In the next step, the laser intensity is increased up to 48 GW/cm^2 at zero delay. The

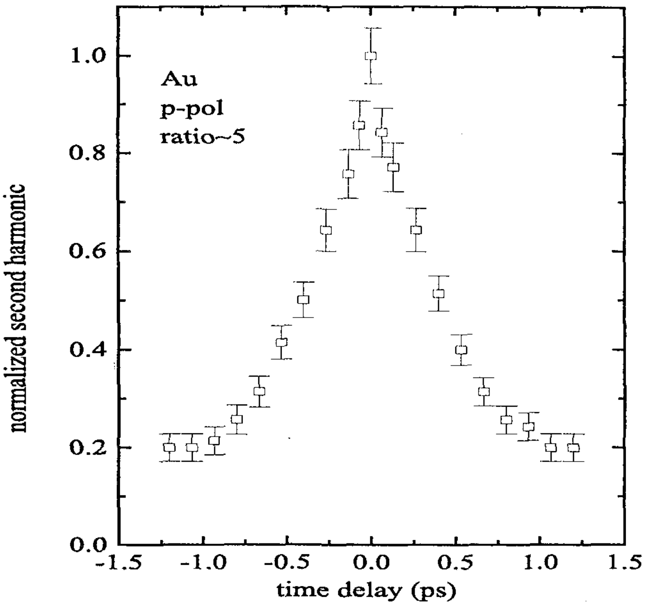

Figure 3.16: Same as Fig. 3.14 but the total fundamental laser intensity at zero delay being 48 GW/cm^2. The contrast ratio is 5:1, i.e., the non-linearity is higher than n=2.

corresponding autocorrelation curve is presented in Fig. 3.16. Now, the peak to background ratio is 5:1. Also, the background starts after 1 ps delay between the green (496 nm) laser pulses. The shape of autocorrelation curve is completely changed. It is obvious, that we are in a higher than 2 non-linear regime and the high electron temperature in the probed region requires more than 1 ps in order to be equal to the lattice one, after the relaxation.

Another important point is that in the measurement of the duration of subpicosecond laser pulses, using an autocorrelator with the metal surface as non-linear medium, one must take in account the above effect, which changes the shape of the autocorrelation curve.

The limits of validity of the pulse duration measurements using the second harmonic produced by a metal surface, can be specified by the intensity dependence curve of the second harmonic generation as shown in Fig. 3.13. The tested laser pulse must be in a clear second order non-linearity regime (see chapter 5).

The experimentally observed SHG enhancement in the high laser intensities could be attributed fully or partly to other possible effects, such as continuum generation with superquadratic dependence on the laser intensity. Both ref.[Agr79-80, Alg87] provide a laser induced thermal glow from the high electron temperature produced by the high intensity picosecond laser pulses. Their calculation for the maximum wavelength of the black-body emission, at a given electron temperature (calculated by the two coupled thermal equations 2.12) are in good agreement with the observed Plank-spectra. It should be noted that this thermal radiation signal depends on the fourth power of the laser intensity [Alg87], as a consequence of the Stephen law. The performed tests in the detection of the SHG of this work, and especially the absence of any continuum emission light during the scanning of the monochromator, excludes the existence of any continuum generation as far our experimental set-up can detect. A roughly calculation of the efficiency of the continuum light in the maximum laser intensity used in this experiment; 50 GW/cm^2, 3200 K, shows that this is at least 3 orders of magnitude less than the observed second harmonic efficiency in the vicinity of second harmonic wavelength.

Reference [Gui91] focuses on a theoretical calculation concerning the second harmonic enhancement due to interaction between a laser beam and a corrugated metallic surface with sinusoidal profile. This effect does not apply to our data since we use a mirror-like surface and the polishing process of this surface avoids any defects as was described in the previous chapter.

The present experimental work strongly suggests that the high electron temperature, produced by the subpicosecond laser beam, gives a positive deviation in the second order non-linearity of the harmonic generation. In comparison with the thermally assisted non-linearity in the electron photoemission from the gold surface, it is observed that, the latter starts at much lower laser intensities ($\leq$ 0.5 GW/cm^2) compared to the harmonic generation and it is much more intense (see chapter 2) . In the following, using a phenomenological model, we attempt to answer how the high electron temperature contributes to the enhancement of the S.H.G. efficiency and why the influence is lower than in electron photoemission. According to Pauli's exclusive principle, the probability for an electron of energy E in the Fermi-Dirac distribution, to absorb two photons of frequency ω and to decay to the initial energy after emitting a 2ω photon, is proportional to $f(E) \times (1 - f(E))$, where $f(E)$ is the Fermi-Dirac

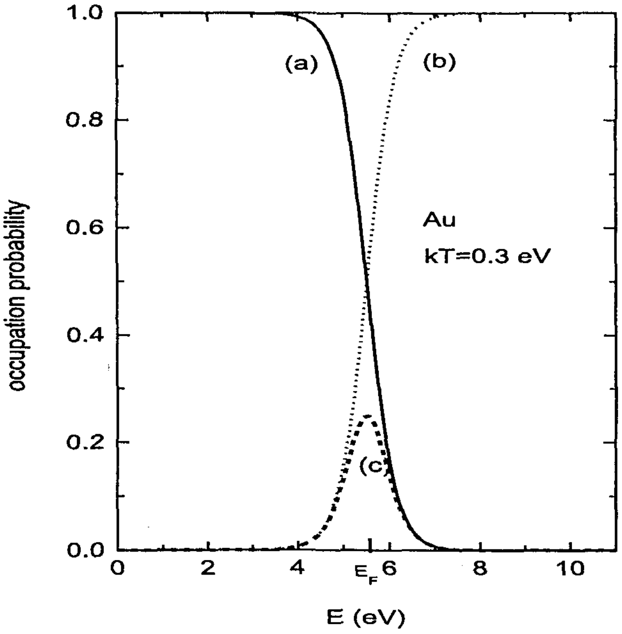

Figure 3.17: (a) The Fermi-Dirac function $f(E)$ versus the energy E for the gold surface and for kT=0.3 eV. (b) The function (1-$f(E)$) versus E. (c) The function $f(E)$ × (1-$f(E)$) versus E. The probability for the harmonic generation is proportional to this function.

distribution function.

In the case where the electron temperature is equal to room temperature, this probability is small. When the electron temperature increases up to a few thousand Kelvin degrees, the probability for harmonic generation increases (see Fig. 3.17). The electrons that contribute with a higher probability to the harmonic generation, are those whose energies are near the middle of the tail of Fermi-Dirac distribution (Fig. 3.17). The S.H.G. intensity $I_{2\omega}$ is proportional to the I_ω^2 and to the integral $\int_0^\infty f(E)\times(1-f(E))\times dE$. The integral represents the probability for harmonic generation according to Pauli's exclusion principle.

Using the methodology described in chapter 2 we solve numerically the coupled thermal Eqs. (2.12) in order to calculate the electron temperature of the Fermi-Dirac distribution. The calculated S.H.G. intensity is normalized to the experimental data. A satisfactory agreement is obtained between the model and second harmonic emission signal. The continuous line in Fig. 3.13 represents the results of our calculations. For low laser intensities ($\leq$ 10

GW/cm^2), where the temperature decoupling between the electrons and the lattice is not intense, and thus the above integral does not contribute to the order of the non-linearity of the S.H.G. because it is equal to a approximately constant multiplication factor. Thus, for these intensities the non-linearity of S.H.G. is in a good approximation constant and equal to two.

On the other hand, in multiphoton electron photoemission, the electrons in the extreme tail of the Fermi-Dirac distribution have a higher probability to be free, after absorbing n photons. The change in the electron occupation number of the extreme tail of the Fermi-Dirac distribution is much more sensitive to the electron temperature than in the middle of the tail. This is clearly shown in Fig. 3.17.

This behavior explains the lower deviation from the nth-power law in the thermally assisted non-linearity of the harmonic generation, compared to that of the electron photoemission for the same laser intensities.

A detailed quantum mechanical theoretical treatment for the absolute values of the S.H.G. from metallic surfaces, taking in account the electron temperature effects, is expected to provide further insight in these phenomena.

3.4.6 Conclusion

In summary, we report for the first time a higher than the expected second order non-linearity in S.H.G. from the gold surface, using intensity dependence measurements and time resolved autocorrelation measurements.

This phenomenon is caused by the intense subpicosecond laser pulses, which produce an increased occupancy of the electronic energy states above the Fermi energy of the metal. The phenomenon mentioned, is weaker than that in the electron photoemission because of Pauli's exclusion principle. Finally, a new method for measuring subpicosecond laser pulse durations, using a metallic surface as non-linear medium, is proposed. Additionally, the limits of its validity are specified.

3.5 Energy Resolved Measurements on Harmonic Generation on Gold Surface Illuminated by Ultrashort Laser Pulses

3.5.1 Introduction

In this section, we present the experimental data for the spectra of the observed harmonics produced on a gold surface by ultrashort laser pulses. The experimental set-up is the same used in the previous experiments descrided in this chapter Fig. 2.1. The only difference is that the slits for both input and output entrances of the 33 cm monochromator are adjusted in order to achieved the maximum resolution of the spectra. The maximum resolution as it will be shown later is between 0.06 nm to 0.1 nm in the range of the wavelengths used and for the gratings used in this monochromator.

3.5.2 Experiment 1: Ti:sapphire Laser Pulses, the Low Intensity Case

The first experiment was performed using as fundamental laser beam of a Ti:sapphire laser at 785 nm. The laser pulse duration as measured by second order autocorrelation technique in a BBO doubling crystal is between 90 and 110 fs depending on operation conditions. Initially, the spectra of the laser beam was measured using the direct output of the beam in the entrance slit of the monochromator. Typical laser spectra are shown in Fig. 3.18.

As we observe, the spectrum can be fitted to a Gaussian with its center at 790 nm and FWHM about 6.9 nm. For a fully coherent, transform limited pulse, as is expected for the Ti:sapphire pulse the measured spectrum agrees well with the pulse duration measurements as is shown in Table 5.1 of chapter 5. Then, the laser beam illuminates the Au target under a 72^o incidence angle. The reflected light is analyzed in the monochromator. In order to eliminate the presence of the fundamental light in the monochromator, which will produce noisy signals in the photomultiplier, we used high pass filters and interference filters depending on the order of the harmonic that is under study.

As a first check that the optics used in the experiment, for focusing on the target or delivering the monochromator, did not affect the spectra of the various harmonics, we measured the spectrum of the reflected fundamental laser. Note that the quartz lens used before the

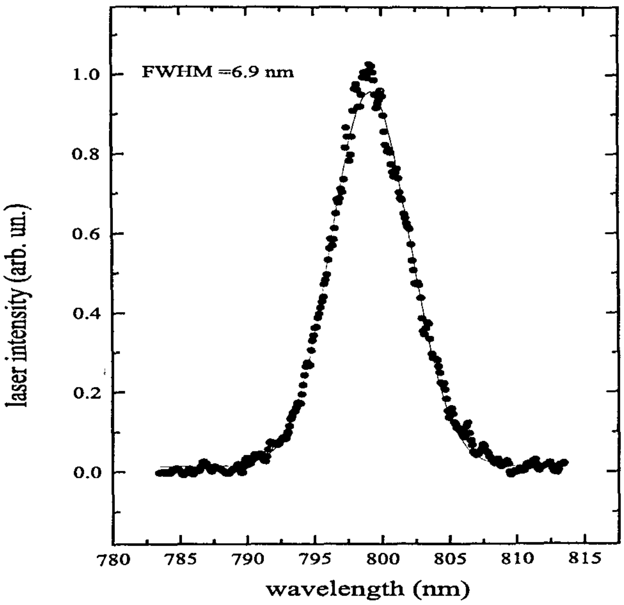

Figure 3.18: Spectrum of the Ti:sapphire laser beam with 110 fs pulse duration. The solid line represents the Gaussian fitting with FWHM 6.9 nm

Au target did not affect the time duration of the laser pulse, as it is checked by the second order cross-correlation measurements. It is important to note that the two lenses produce a telescope in order to avoid extra divergence of the laser beam and in the harmonic beams, which may affected the observed spectra. The signal is measured using a lock-in amplifier with a chopper at 450 Hz. The repetition rate of the laser is about 80 MHz. The spectrum of the reflected fundamental laser beam was the same as before the reflection for the available intensities of this laser i.e., up to 100 MW/cm^2.

Using various optical filters, we measured the spectrum of the reflected second harmonic generation from the gold surface. The results are plotted in Fig. 3.19. The FWHM for the harmonic spectra is 2.5 nm and for the third 1.8 nm. It should be noted here that the spectra of the second harmonic obtained from a BBO crystal is 2.6nm, i.e., similar to that obtained from the gold.

Comparing the spectra of the second and third harmonic generation with the fundamental one, we can observe exactly what one expects for a pure photodynamic multiphoton non-linear effect without any additional processes. In first approximation every λ in the fundamental spectra produces a $\lambda/2$ in the second harmonic spectra and a $\lambda/3$ in the third harmonic one. Suppose a Gaussian spectra for the fundamental, i.e., $I(\lambda) \propto e^{-(\lambda/d)^2}$ where d is linearly proportional to the laser pulse bandwidth in the wavelength domain.

Now for the n-harmonic spectra one could expect [Die85] a spectra profile (in λ/n region): $I(\lambda/n) \propto e^{-[(\lambda/n)/d_n]^2}$ where $d_n = d/(2\sqrt{n})$. Thus, in this simple situation the wavelength bandwidth of the nth harmonic is divided by the parameter $2\sqrt{n}$. These calculations agree well with the measured FWHM of the spectra of 2ω and 3ω in comparison with the fundamental spectra. Thus, the expected value of the FWHM for the second harmonic spectra is $6.9\text{nm}/\sqrt{8} = 2.44nm$ which agrees with the experimental value, 2.5 nm. Similarly, the expected FWHM of the third harmonic spectra is 6.9 nm/$\sqrt{12}$=1.99 nm which also agrees with the experimental value 1.9 nm.

The previous analysis is valid because the laser intensity of the fundamental is maximum 0.1 GW/cm^2. On the other hand, we have proved earlier that the electron relaxation phenomena on metallic surfaces are related to the high electron temperature, produced by the subpicosecond intense laser pulses, which may cause modifications on the harmonic generation signal. The laser intensity threshold for such phenomena is in the range of several 10 GW/cm^2 for the 496 nm, 0.5 picosecond dye laser pulses as it was proved previously. One can expect that these phenomena will appear at even higher laser intensities for the Ti:sapphire laser pulses, since these pulses are about 5 times shorter than the dye pulses. Thus, the change in the electron temperature is expected to be lower for a Ti:sapphire laser pulse compared to the dye case. Nevertheless, in any event the used laser intensity for the Ti:sapphire case was much less than the intensity threshold for such phenomena.

Another important point is that the Ti:sapphire laser photon energy is 1.56 eV. This is much smaller than the energy gap of the d-band to the Fermi-surface transition which is about 2.4 eV for gold [Ros73, Sch87]. Thus, no interband transition is induced. The density of states of gold is almost constant in the vicinity of the Fermi energy [Smi71]. Then, the Ti:sapphire pulses act on a metallic surface where the electrons are described quite well by the Sommerfeld model. So, the continuous and flat tunability for any excitation is expected.

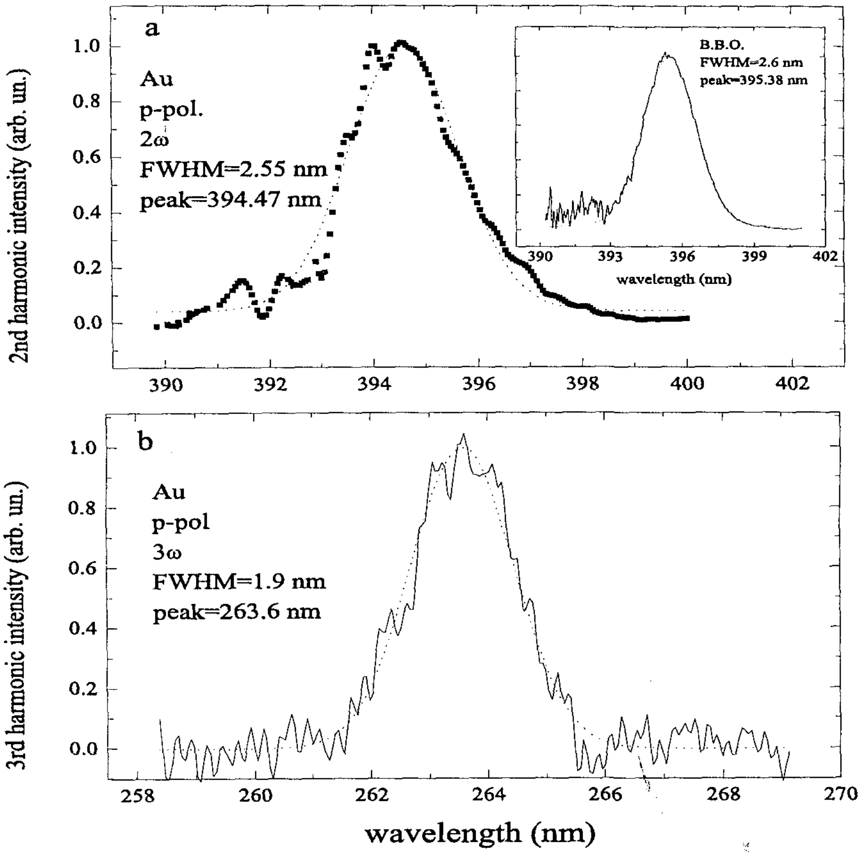

Figure 3.19: a) Spectra of the second harmonic obtained from a gold surface. The FWHM of the Gaussian fitting curve is 2.5 nm with peak at 395 nm. Inset: It is shown the second harmonic spectra obtained from the BBO crystal. The FWHM of the Gaussian fitting curve for the BBO case is 2.6 nm. b) Spectra of the third harmonic obtained from the gold surface. The FWHM of the Gaussian fitting curve is 1.9 nm peaking at 263 nm.

For all these reasons, it is clear why we did not observe any modifications in the harmonic spectra obtained from the gold surface in the Ti:sapphire case.

3.5.3 Experiment 2: Dye Laser Pulses, the High Intensity Case

3.5.4 Experiments

Following the previous analysis it may be interesting to perform the same experiments for the harmonic generation from gold using the 496 nm, 450 fs dye laser pulses. The laser intensity of these pulses may increase up to several 10 GW/cm^2 at the grazing incidence geometry that is required for the harmonic generation in the metallic surface as we have already discussed in this chapter. At these high laser intensities, we have already observed a higher than the expected non-linear increase of the second harmonic experiment versus the incident dye laser intensity.

We used 77.7^o angle of laser incidence in order to connect this experiment with the previous one, where we performed integrated spectra measurements. The optical set-up was the same as previously and the monochromator was able to separate wavelengths as near as 0.1 nm.

The spectra of the fundamental laser pulse is shown in Fig. 3.20. The spectra profile is asymmetric with a 1 nm FWHM. Then, second harmonic light is produced in a BBO doubling crystal. The spectra of the second harmonic from the BBO crystal is presented in Fig. 3.21. We observed that the latter spectra has the same profile with the fundamental one with a FWHM 0.35 nm. This value is exactly what we expected for a pure photodynamic experiment, as we have already analyzed in the case of Ti:sapphire laser pulses.

Following, the spectra of second harmonic produced on the gold surface was measured. The results for various laser intensities are plotted in Fig. 3.21. The main observation is that as the laser intensity increases, new wavelengths are added to the second harmonic spectra. In the low intensity region, up to 7.5 GW/cm^2, the previous effect was not observed. On the contrary, for the higher intensities, an asymmetric one sided (at the low energy side) broadening of the spectra width was observed. The FWHM of the second harmonic spectra

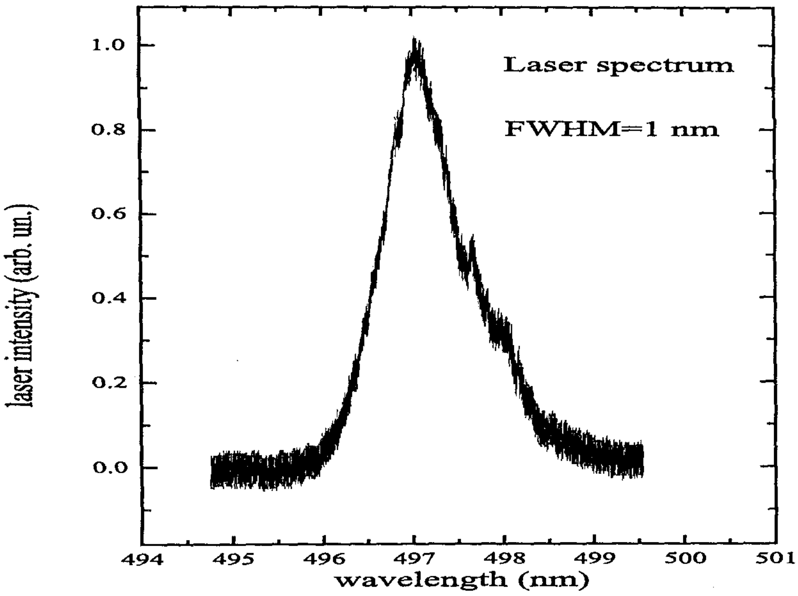

Figure 3.20: Spectra of fundamental dye laser pulse, 450 fs pulse duration. The FWHM is 1 nm with peak at 497 nm.

obtained from gold is increased from 0.35 nm to 1.3 nm for the laser intensity range from 5 to 35 GW/cm^2, respectively.

This asymmetric broadening of the second harmonic spectra required the tunability experiments, i.e., to repeat the same experiment for various fundamental laser wavelengths in the allowed region of the dye laser, taking care to have in all cases 450 fs laser pulse. This wavelength region was from 521 nm to 491 nm. The results are plotted in Figs. 3.21, 3.22 3.23, 3.24, 3.25, 3.26.

It is observed that no effect exists in the range of 521-504 nm fundamental wavelength region for all of used incident laser intensities. In the remaining wavelength region and at high laser intensities, a systematic generation of new wavelengths in the low energy region of the second harmonic spectra is appeared. In the latter case the effect is again intensity dependent and it is disappeared for the low intensities. In connection with the above observations, a higher than two non-linearity in the intensity dependent curve of the second harmonic is observed, when the laser intensity exceeds 20 GW/cm^2. This higher than the expected

(n=2) nonlinearity was observed only for shorter than 504 nm (2.46 eV) and it seems to disappear for longer ones. It is important to recall here that the energy difference for the transition from the top of the d-band up to the Fermi-level of the conduction band of gold is 2.4±0.1 eV. This value is close enough to the 511 nm wavelength threshold of the previous phenomena.

In the next step we tune back in the 496 nm, high intensity case and we perform polarization dependence measurements of the second harmonic light. We changed the incident laser polarization from p-polarization to s-polarization and simultaneously we measured the second harmonic spectra obtained from the gold surface. The results are shown Fig. 3.27. We observe that the total harmonic signal is decreased as the laser polarization was turned from p to s-type. This was expected as it has been mentioned in this work several times. The novel result is that the shape of the spectra remains unchanged as the incident laser polarization changes.

The last experiment performed for the analysis of the observed effect of the generation of new frequencies in the metallic second harmonic generation was the pump-probe time resolved study of this effect. In this study, we measured the second harmonic generation produced from two pulses which have various time delays between them. The results are plotted in Fig. 3.28. As is observed the increase of the FWHM in the second harmonic spectra has a time dependence and has completely decayed when the pump is about 500 fs away from the probe pulse.

It should be noted here that similar and more intense effects in the second harmonic generation from the gold surface was observed when the laser incidence angle was 60^o. In this angle it is expected that we obtain the maximum signal for the second harmonic generation according to the semiclassical theory of Jha (ω=496 nm). For this laser incidence angle the FWHM of the second harmonic spectra obtained from the gold surface was in the range of 0.4 nm to 2 nm for laser intensities in the range of 3 to 35 GW/cm^2, respectively, see Fig. 3.29.

It is well known that the second harmonic optical processes are very useful to probe

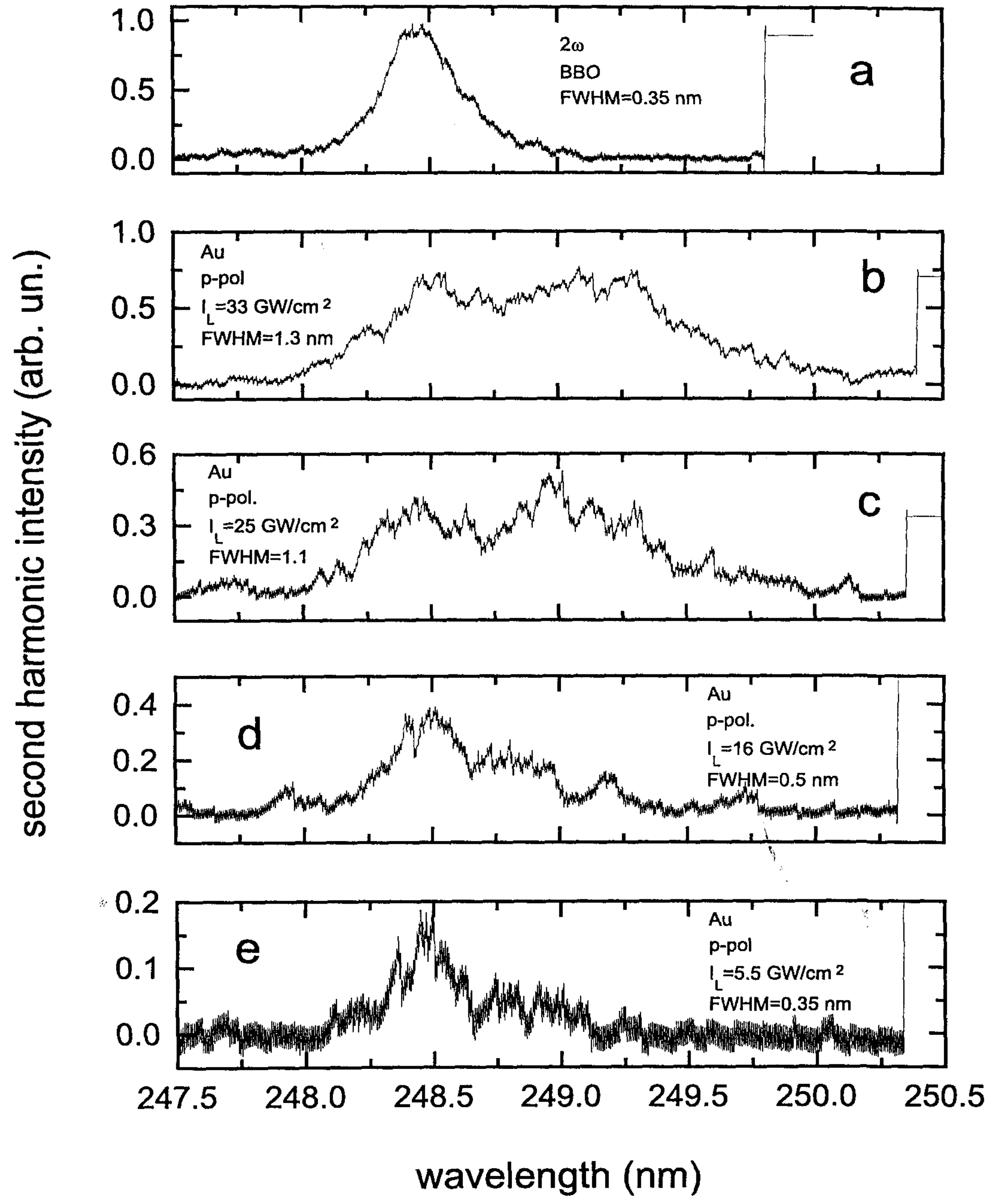

Figure 3.21: a)Spectra of the second harmonic obtained by a BBO crystal using a 450 fs, 497 nm fundamental laser beam. b-e)Spectra of the second harmonic obtained from a gold surface for various intensities of the p-polarized 497 nm, 450 fs p-polarized laser pulses. For the higher intensities an asymmetric expansion is observed of the spectrum in the low energy side. The angle of laser incidence was 77.5°.

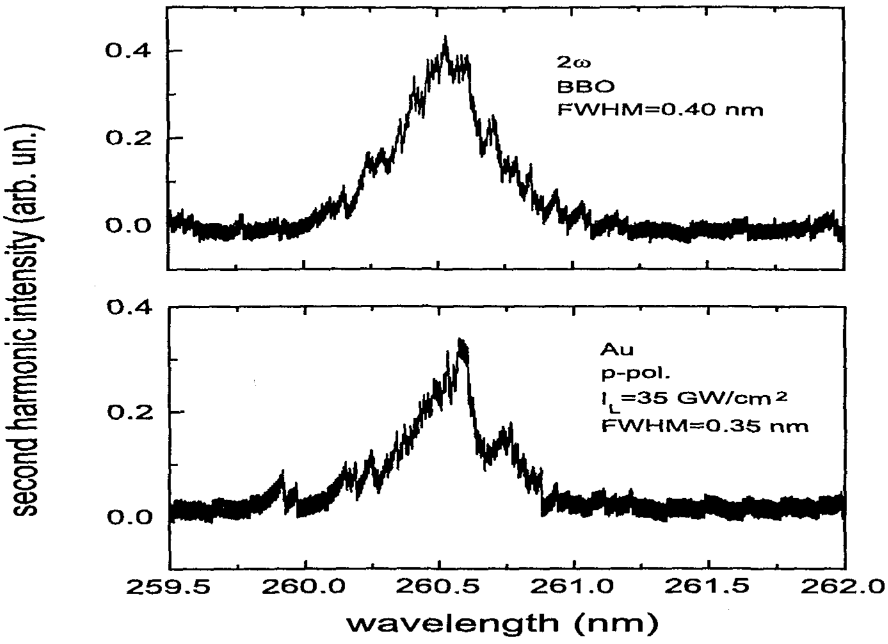

Figure 3.22: Same with Fig. 3.21, the wavelength of fundamental peaking at 521 nm. Here is presented only the maximum laser intensity case. No expansion of the of second harmonic from gold surface was observed.

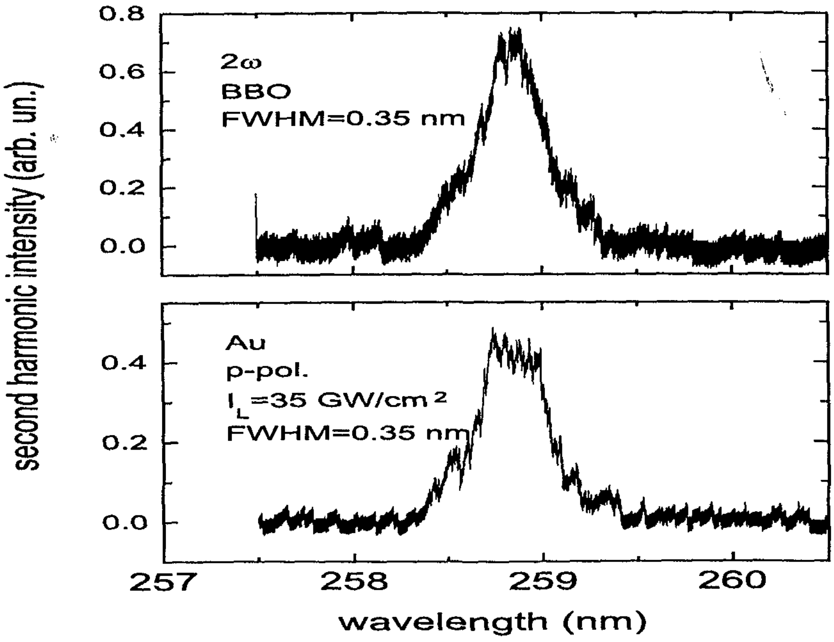

Figure 3.23: Same with Fig. 3.22, the fundamental wavelength is 517.5 nm.

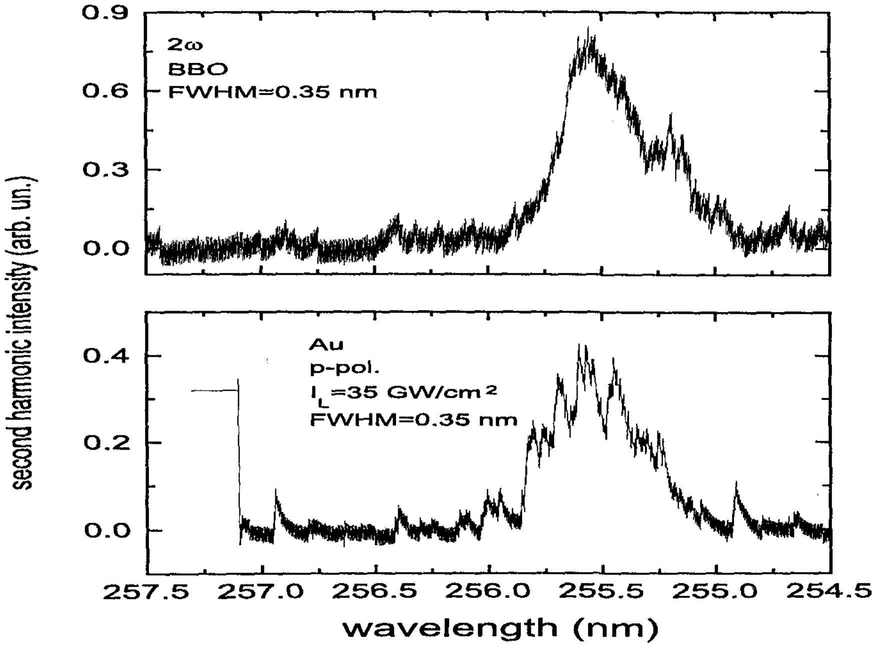

Figure 3.24: Same with Fig. 3.22, the fundamental wavelength is 511 nm.

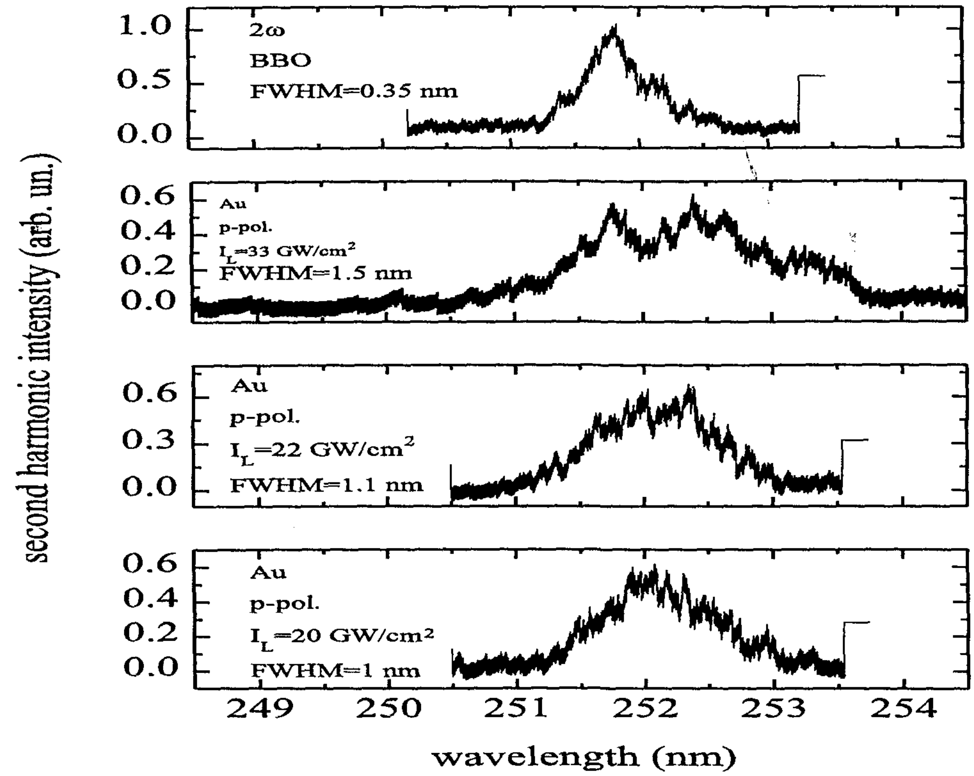

Figure 3.25: Same with Fig. 3.21, the fundamental wavelength is 503.5 nm.

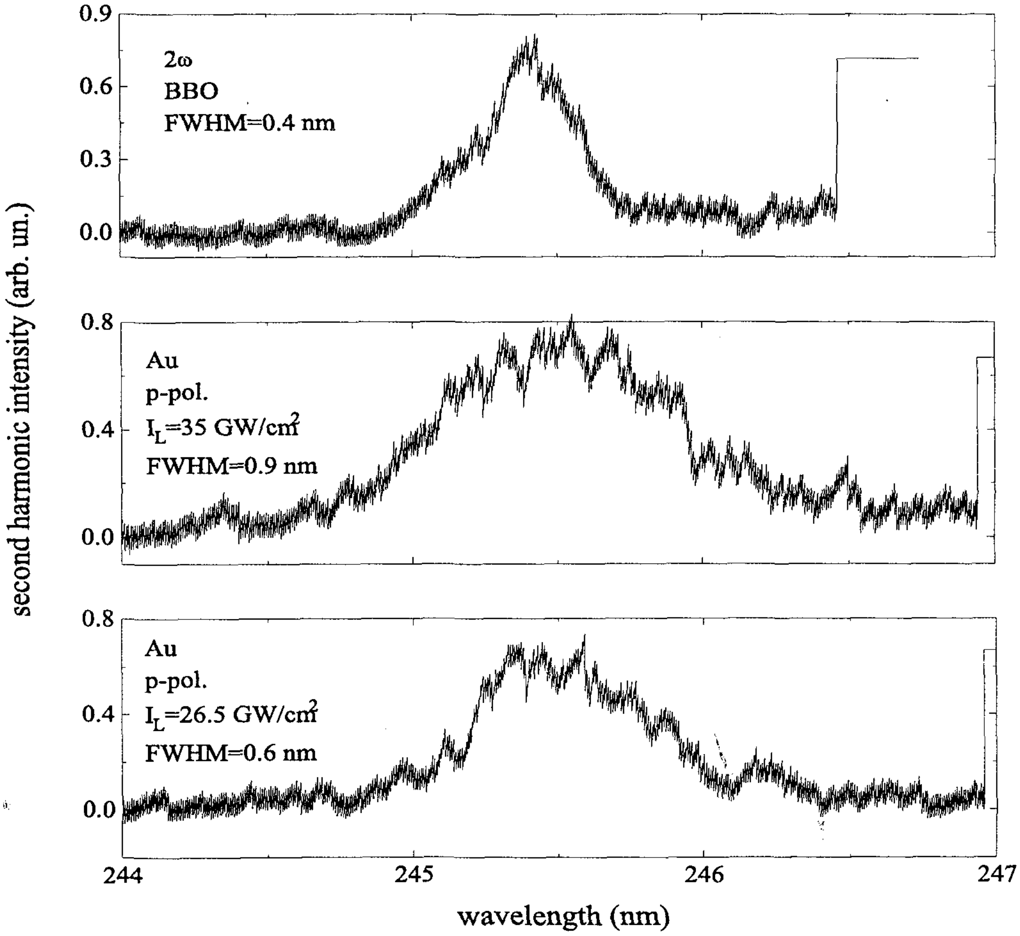

Figure 3.26: Same with Fig. 3.21, the wavelength of fundamental peaking at 491 nm.

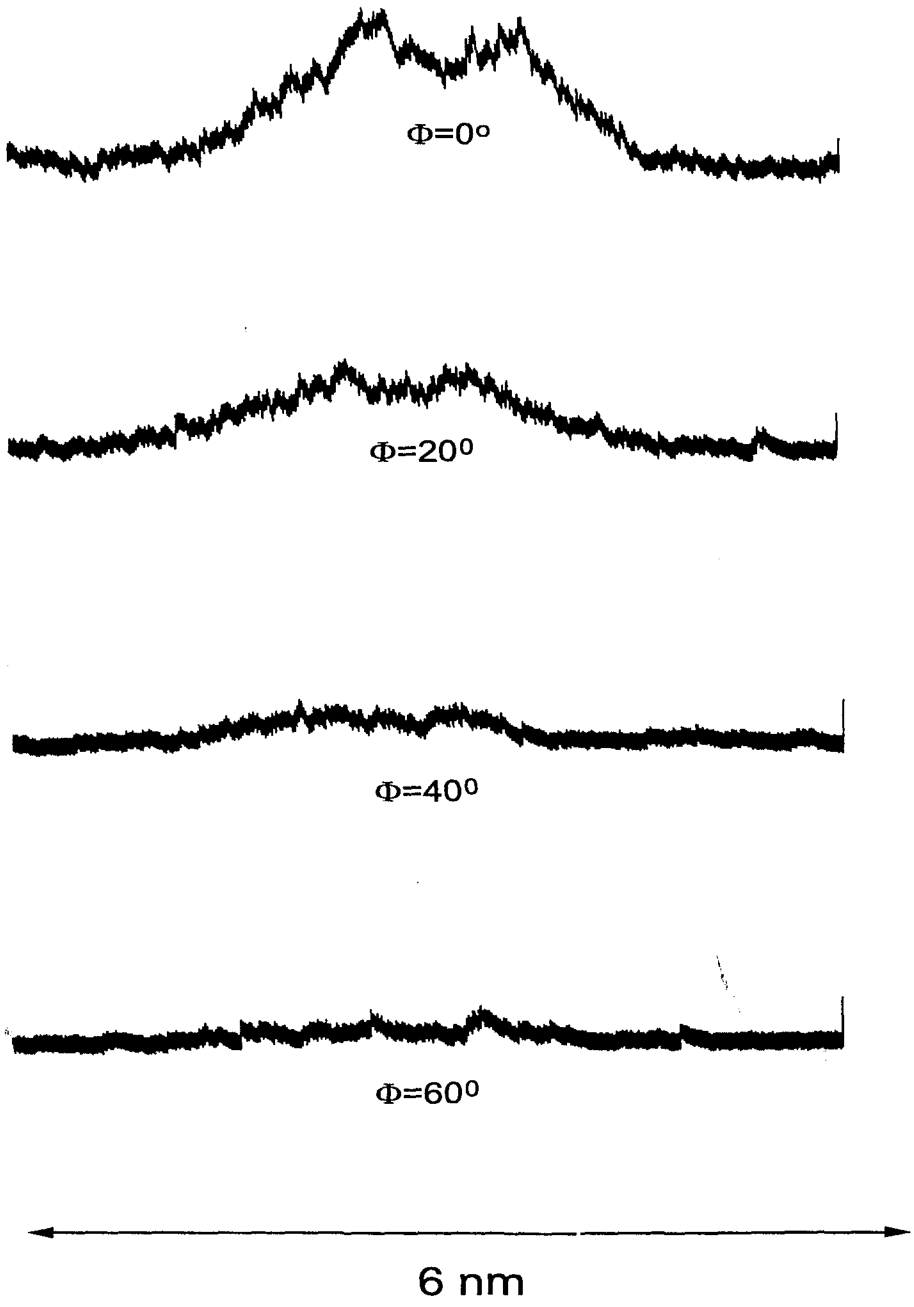

Figure 3.27: Spectra of the second harmonic obtained for the gold surface for 497 nm, 450 fs dye laser pulses for various polarization angles ϕ. The angle $\phi = 0°$ corresponds to p-polarization. The laser intensity was 30 GW/cm^2.

surface phenomena. On the other hand, very few works demonstrate the capabilities of energy resolved harmonic generation experiments on metallic surfaces [Urb92].

A scenario follows that may explain our experimental results of energy resolved measurements in the case of high intensity, short, dye laser pulses. The situation is clear at the fundamental laser wavelength region where interband transition cannot occur. In this case only electrons located in the conduction band participate in the transitions as deep as $\hbar\omega$ down from the Fermi level. Electron temperature changes are mainly due to surface electrons when they absorb one laser photon and then decay to their equilibrium state via non-radiative pathway, i.e., via electron-phonon and electron-electron scattering. It is obvious that the number of unoccupied positions that the electrons leave behind when they participate in the absorption, cannot be re-occupied completely again after the disexcitation via non-radiative pathway or via electrons that initially absorbed one photon and after decay emit again one photon (reflection). The electrons that participate in the second harmonic generation absorb initially two photons and decay emitting one photon with double energy. Since the rates of all the processes described above are about the same (in the order of a picosecond), the overwhelming majority of electrons that emit 2ω photons return to their initial position see Fig 3.30b. Thus, no broadening is observed to the second harmonic spectra.

The situation is different in the case when the fundamental wavelength is able to drive an interband transition, Fig 3.30a. Since the density of states in the d-band is higher than in the conduction band, many electrons of the d-band absorb one laser photon and climb up to the Fermi-level in the conduction band. In the conduction band, electrons absorb one or two (or more) laser photons and leaving unoccupied positions (holes). Simultaneously electrons from the d-band are able to absorb one laser photon and occupy these free positions in the conduction band. Thus, the electron population of the conduction band increases dramatically. The electrons that come from the d-band and occupy positions a higher up of the Fermi-Level decay via electron-electron and electron-phonon scattering and in this way they fill-up many free positions in the vicinity of Fermi level. Now several electrons that participate in the production of the second harmonic cannot decay to their initial equilibrium

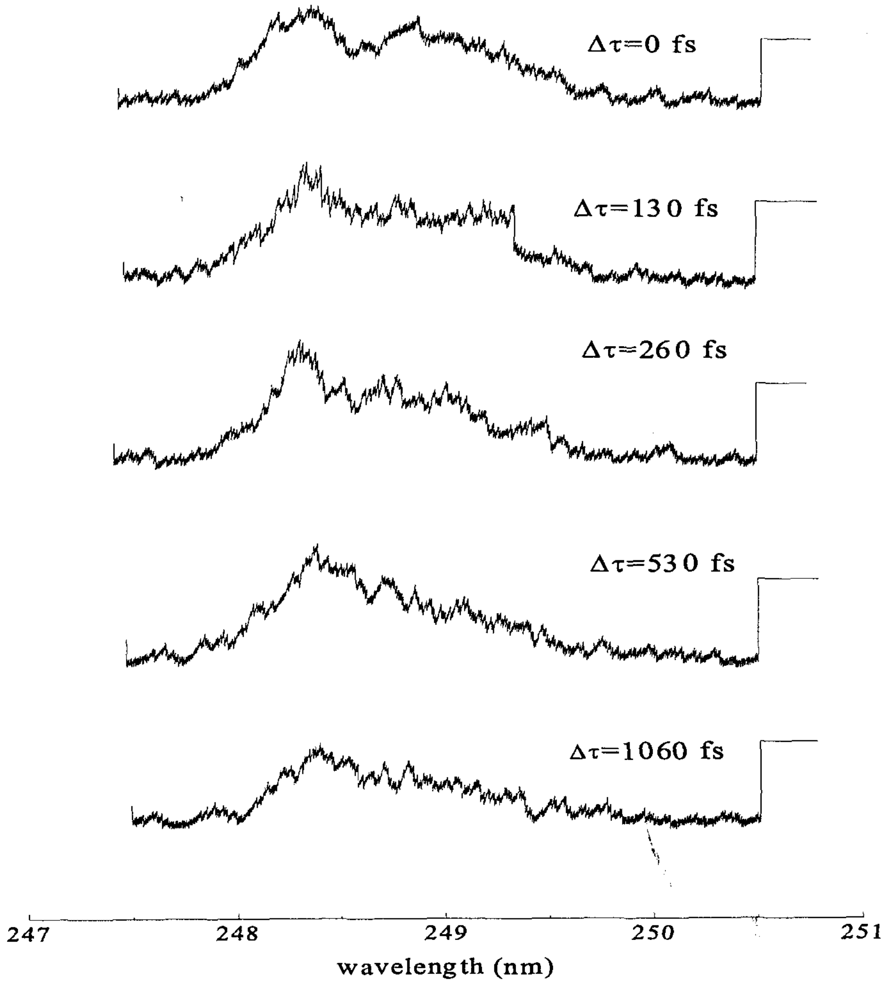

Figure 3.28: Pump-probe measurements of the spectra of the second harmonic obtained from gold surface using p-polarized laser pulses, 450 fs and 497 nm. The pump laser intensity was 32 GW/cm^2.

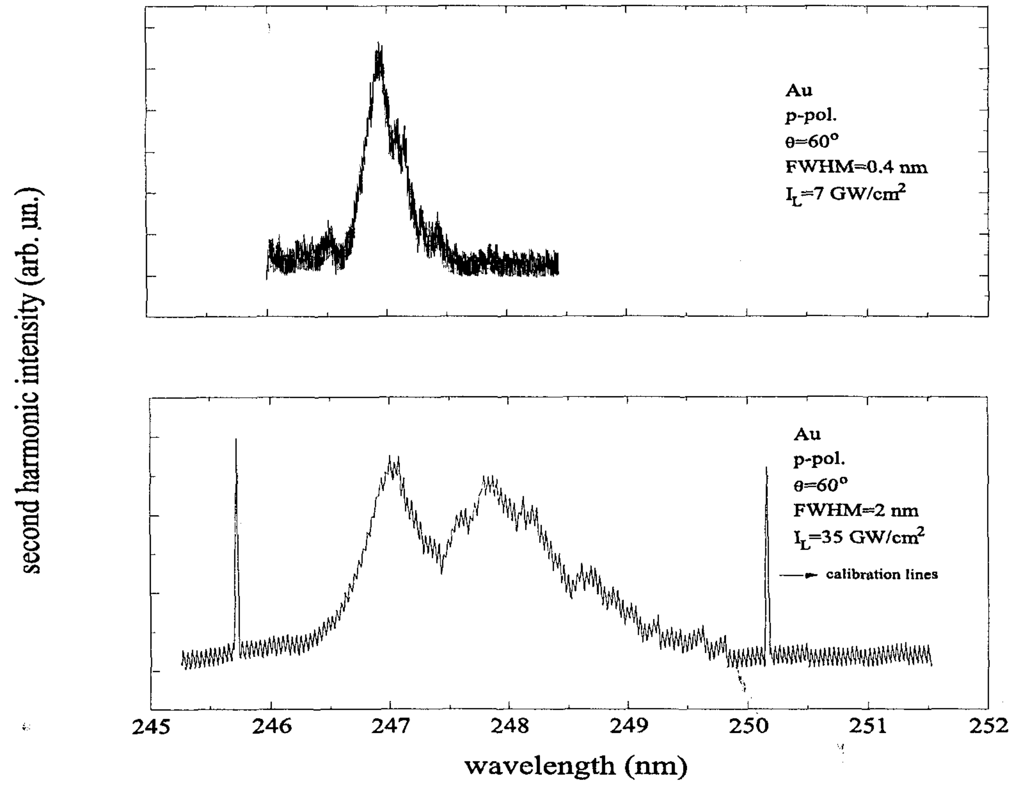

Figure 3.29: Similar figure with Fig. 3.21 but the laser incidence is 60°.

states because these are full, but occupy states with higher energy. This way one can explain the broadening of the spectra of the second harmonic in the low energy side.

At the same time, based on the previous scenario, one may explain the increase of the yield of harmonic intensity with higher than two non-linearity versus the laser intensity. In the case where interband transitions can occur, many electrons which come from the d-band contribute to the increase of the electron temperature of the Fermi-Dirac distribution of the conduction band. Thus, as we showed in a previous section, high electron temperature give rise to a higher harmonic yield. In the case that interband transitions cannot occur, the electron temperature also increases but to a lesser extent, as only the electrons of the conduction band contribute in the absorption.

The experimental result (the asymmetric broadening for wavelengths that are extremely close to the interband transition wavelength is intensity dependent) can be explained by the fact that for higher laser intensities the electron temperature increases. Thus, free positions are created below from the Fermi-level in the conduction band and consequently more d-band electrons participate in the absorption, so that the phenomena described in the last two paragraphs can take place. On the contrary, when the laser photon energy is small enough so that interband transitions cannot occur even when the electron temperature increases by the electrons of the conduction band, then no broadening is observed. This is confirmed by the pump-probe measurements shown in Fig. 3.28; after about 0.5 ps the electron temperature is quite smaller than its highest value, consequently the broadening of the harmonic spectra is negligible.

The reader may wonder how this simple model, used in the previous paragraphs in order to explain the influence of electron temperature in the harmonic generation on metallic surface, works, since it does not take into account any interband transitions and any time-dependence of the parameters. The answer is that the interband transitions were taken into account by the reflectivity parameter. The reflectivity changes dramatically in the vicinity of an interaband transition wavelength threshold. The reflectivity is high for laser photon energies slightly lower than interband transition threshold. On the contrary the reflectivity is very small for laser photons equal or sightly higher than the interband transition threshold.

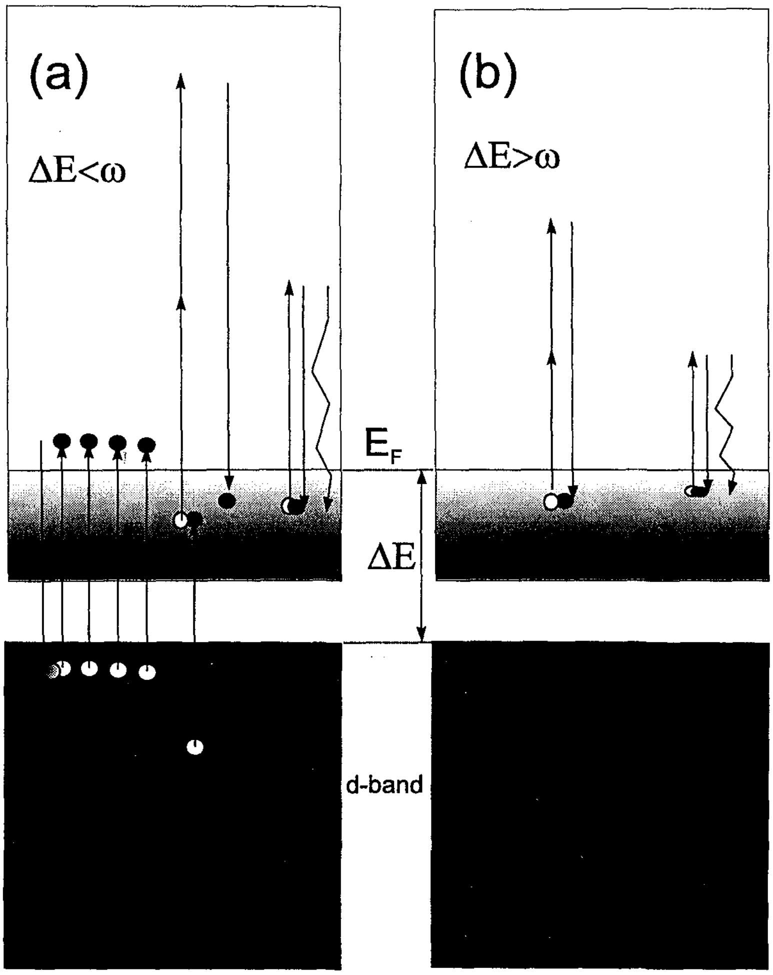

Figure 3.30: a) Harmonic generation for the case that the laser photon energy is higher than the interband transition threshold. b) Harmonic generation for the case that the laser photon energy is lower than the interband transition threshold

From the two temperature model that we used (Eqs. (2.12)), it is clear that the higher the reflectivity the higher the electron temperatures resulting. The time dependence problem, for the model, was solved by the fact that in the calculation we have taken in account average values of electron temperature. In the article of Urbach et al. [Urb92], a dramatic increase of second harmonic generation on a monocrystalline silver surface was observed when a nanosecond laser beam tuned to about 2.0 eV and the laser polarization is such so as to probe the crystal orientation for interband transition. The increase was attributed to the electrons that were initially located in the d-band and with the laser beam action absorb two photons, go to conduction band and then decay again to their initial level emitting the second harmonic photon. In that work the interband transition threshold was 3.8 eV. In the energy space from -4 eV up to -1 eV below the Fermi-level no resonance states exist. Thus, the absorption occurs non-resonantly via virtual states.

In our experiment the situation is different. When the laser photon is unable to produce single-photon interband transition in order to reach unoccupied states close or up from Fermi-level consequently cannot produce any multi-photon transition from the d-band. The reason is that in our experiment the wavelength was in any case close enough to the wavelength threshold for interband transition. Slightly below the Fermi energy there are energy states which are completely full, so that no interband transition occur. This is confirmed also experimentally by the tunability experiments, where we measure the intensity of the second harmonic generation as a function of the photon energy of the fundamental laser beam as well as by polarization measurements which were presented in the previous sections of this chapter. In the case that the laser photon energy is higher than the interband transition threshold, electrons of the d-band can absorb two laser photons and then decay to their initial d-band state. In such cases, simultaneously both conduction and d-band electrons should participate in the harmonic generation. This should lead to an increase of harmonic efficiency, observed by the tunability experiments at the low intensity region where the non-linearity is two (2). This was not seen in our tunability experiments shown in Fig. 3.11, and ref.[Mou95]. The previous experiments are a strong evidence that only the conduction electrons participate in the second harmonic generation. Another indication is the polarization measurements. The strong dependence of second harmonic generation on gold by the normal electric field (p-polarization) compared to s-polarization (ratio ≈ 20, see Fig. 3.10, 3.27) shown that the phenomenon is predominantly caused by the free electron of the conduction band and has a surface origin.

Chapter 4

Electron Relaxation Measurements from Metallic Surfaces

4.1 Introduction

As has already been described in chapter 2, if a metal is excited by a laser pulse with duration less that the electron energy relaxation time, a transient inequality between the electron and lattice temperatures occurs. Thus, the relaxation dynamics of excited electrons in metals reveal fundamental information about the electron-phonon and electron-electron scattering. An introduction to the physics governing the above scatterings was presented in chapter 1.

A widely used technique to study the dynamics of the excited electrons in metals is femtosecond pump-probe spectroscopy. Since the electron energy relaxation times (cooling times) are of the order of one picosecond (or subpicosecond) the study of the dynamics of the non-equilibrium electrons requires ultrafast laser pulses.

In the sections below, the techniques for time-resolved studies of the electron relaxation from metals in picosecond and femtosecond time regimes are presented.

4.2 Transient Thermoreflectance Spectroscopy (TTS)

TTS is based on the observation that relatively small changes in a reflection (or an absorption) spectrum can be enhanced by derivative methods, i.e., measurement of the change in the reflection (or absorption) due to a modulation of some physical parameter such as temperature, electric field or stress [Car69].

In the case of temperature modulation, a change in the reflectivity will result from thermally-induced changes in the dielectric function which can be related directly to the electronic band-structure of the metal. Scouler initially [Sco67], and few years later Rosei and Lynch [Ros72], observed a polarity reversal of ΔR when the photon energy was tuned through the d-band to the Fermi-level interband transition energy of a noble metal (Au, Cu, Ag).

In noble metals, which are used predominantly in this thesis, the band structure which is responsible for optical transitions from the top of the d-band to the empty conduction-band, near the Fermi level is represented in Fig. 4.1 [Ees86]. This transition occurs at a photon energy of about 2.15 eV in Cu, 2.4 eV in Au, and 4 eV in Ag [Sco67, Ros72, Ros74].

The Fermi-Dirac distribution function of the occupied electronic states near the Fermi level is :

$$\rho_E = \frac{1}{1 + e^{(\hbar\omega-(E_F-E_d))/(k_B T)}}. \tag{4.1}$$

When the conduction-electron temperature increases, ρ_E decreases for $\hbar\omega < E_F - E_d$. Thus, for $\partial\rho_E/\partial T<0$ more d-band electrons are promoted into the conduction band by the absorption of laser photons. This results in a decrease of the reflectivity. At the same time, there is a heating-induced increase in the number of the conduction electrons which occupy states above E_F, i.e., $d\rho_E/dT > 0$ for $\hbar\omega > E_F - E_d$.

In this case, an increase of the reflectivity is expected since fewer empty conduction-band states are available for transitions from the d-band. The above feature is presented in Fig. 4.2 ($\Delta\rho_E$ vs $\hbar\omega$).

Thus, changes in the electron occupancy produce changes in the interband absorption which are directly proportional to the change in the imaginary part of the dielectric constant which is proportional (for small changes) to the differential reflectivity as

$$\frac{\Delta R}{R} = \frac{1}{R}[\frac{\partial R}{\partial\epsilon_r}\Delta\epsilon_r + \frac{\partial R}{\partial\epsilon_i}\Delta\epsilon_i] \tag{4.2}$$

Where R is the reflectivity, ϵ_r and ϵ_i are the real and imaginary part of the dielectric constant of the metal, respectively.

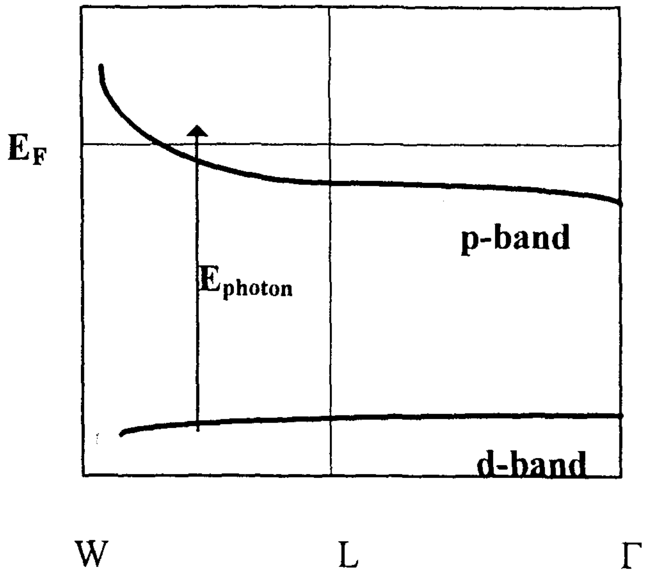

Figure 4.1: Energy diagram for noble metals. The d-band is full as well as the p-band up to the Fermi level.

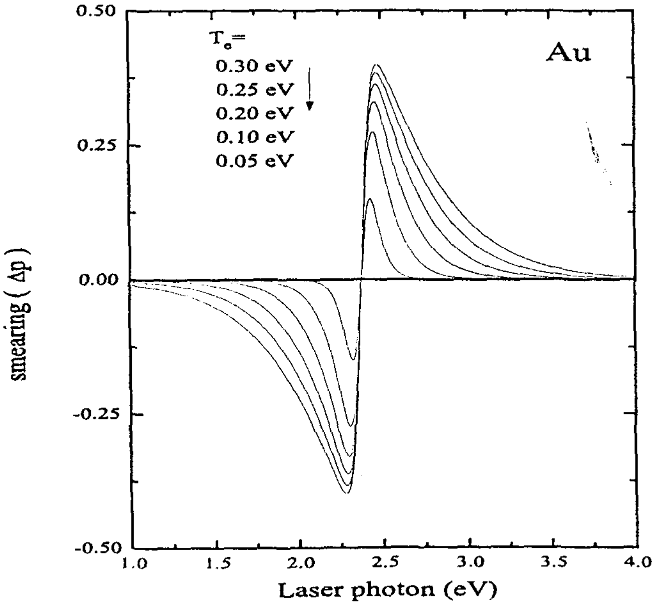

Figure 4.2: Calculated change in electronic occupancy in the vicinity of Fermi energy for various electron temperatures (Fermi smearing)

Experimentally, a femtosecond pump-probe technique is used to perform time-resolved measurements of the transient reflectivity changes. There are many works using TTS in order to study the dynamics of electron relaxation phenomena in metal surfaces [Ees83, Ees86, Els87, Sch87, Bro87, Lor91, Orl95]. The main conclusions of the above studies are:

I) The observation of non-equilibrium electrons with cooling times in the order of several 100 fs up to a few (1-3) ps.

II) The heat is carried by non-equilibrium electrons and the heat transport occurs on a femtosecond time scale with a delay which scales linearly with sample thickness. Observation of heat-transport velocity of the same order as u_F (Fermi velocity) suggests that ballistic electronic motion may also contributes to the heat transport.

III) The loss of the energy of the initially hot-electron distribution is faster a in polycrystalline metal than in a single crystalline metal.

IV) The thickness of the metal film is inversely proportional to the hot-electron cooling time.

Thus, the determination of the energy relaxation time (cooling time) via TTS measurements requires extreme care as several effects may spoil the results. The exact position of the d-band to Fermi level transition cannot be determined from the shape of the TTS curves alone, e.g. from the absence of the rapid component, A. Lorincz et. al. [Lor91] show that this is a function of the relaxation time too.

Also, the dependence of the dielectric constant is complicated in the non-equilibrium regime, because it is generally a function of both the electrons and lattice subsystems characteristics. A solution is the probe wavelength set to the free electron domain, where the contributions of bound electrons is negligible. There is also another advantage of this choice too, since the insensitivity of the free electron contribution to volume changes allows the use of the equilibrium coefficient.

Another problem of the TTS method is apparent in the case of thick samples. There, the fast diffusion of the electron subsystem may appear in the transient reflectivity measurements. Such transients can be avoided if films thinner than the penetration depth are used.

But, also in that case, interference terms from the front and the back side of the thin film must taken into account.

The main problem for the TTS measurements is that visible pulses shorter than few hundred of fs are approaching the transient reflection expressions, and thus losing its validity [Mik88]. From the technical point of view there are additional problems in order to observe the TTS. The first is that the probe beam wavelength must lie in the area(± 0.5 eV) of the transition from the d-band to the Fermi-level. Thus, this method is restricted to wavelengths close to an electronic transition in a metal. The other problem is that the change of the differential reflectivity for laser intensities of the order of a few GW/cm^2 is (depending of the conditions) is the order of 10^{-4} to 10^{-3}. This small change requires a very well stabilized laser system with a repetition rate in the range of kHz or MHz, in order to have good statistics and avoid the fluctuation that can mask the small change of reflectivity. Although thermomodulation studies are widely used, especially in the case of high repetition and low power lasers, they are not easily transferable to low repetition and high power lasers with nonlinear saturation effects.

Another subpicosecond optical transient-reflection method is one which employs the surface plasmon resonance of thin films as a probe to study small transients of the electron and lattice temperature [Rog90]. A surface plasmon is a transverse coupled excitation of the electron gas and electromagnetic field and can easily be optically excited with a method based on attenuated total reflection [Kre71]; A p-polarized laser strikes the hypotenuse face of a fused-silica prism coated by a thin metal film. Surface plasmons are excited at the metal-air interface when the angle of incidence has a certain value θ_{SP}. At this angle, the parallel momentum of the light inside the fused silica matches the momentum of surface plasmon and practically all the incident light is converted into surface plasmons at the metal-air interface. The position, depth and width of θ_{SP} depend strongly on the dielectric constants, i.e, of electron temperature. Thus, by probing the reflectivity changes near the critical angle one can estimate the electron relaxation time. This method is suitable for studying metal films excited in low temperature, but with a well defined surface-plasmon resonance. For this reason it is not applied for all metals. The geometry of surface-plasmons requires the matching of the optical dielectric constant of metal with that of the prism used, which is not possible always. In any case, the above restrictions of the reflectivity experiments leads us to use another method in order to study the electron relaxation phenomena.

4.3 Time-Resolved Photoemission (TRP)

4.3.1 Introduction

The study of the electron photoemission from metallic surfaces was one of the favorite tools in the study of electronic band structure. The advent of high intensity ultrashort-pulsed lasers made possible the extension of studies in time-resolved phenomena like relaxation processes. Additionally, if the laser pulse duration is shorter than the electron-phonon energy-transfer time, then the electron and the lattice will not be in thermal equilibrium. The time-space evolution of the electron and lattice temperature are governed by the set of coupled differential Eqs. (2.12).

As was explained in chapter 2, the non-equilibrium high electron temperature affects the yield of the photoemission. According to Fowler-DuBrighe theory, in the single-photon electron emission the photocurrent density increases as a function of the electrons temperature by the law described in Eq. 2.28. The TRP method was proposed by Fujimoto et. al. [Fuj84], as a possible tool to study the electron-phonon dynamics in metals by measuring the integrated emitted charge, using multiphoton photoemission. However, space charge effects complicated the analysis of their experimental data. In our experiment, the space charge effects were eliminated by the same method proposed by Girardeau-Montaut et. al. [Gir89, Gir89a].

The novel technique is the single-photon autocorrelation (SPA). The proposed SPA has the advantage, that the transition from linearity to the non-linearity, caused by the thermal non-equilibrium between the electron and the lattice, is directly observed in the autocorrelation curves when they start to have a Gaussian-like shape.

On the contrary, in the n-photon electron emission ($n > 1$) the shape of the autocorrelation curves are never flat, independently of the existence of the thermal non-equilibrium between electron and lattice. For example in the case of n=2, the ratio of the photoelectric signal of complete overlap relative to no overlap is a minimum of 3:1 when the electrons and the lattice are in thermodynamic equilibrium. The multiphoton autocorrelation therefore causes difficulties in the direct observation of thermally assisted non-linearity and thus in the measurement of the relaxation time.

4.3.2 Experiments

The photocathodes (Cu,Au,W,Al,Fe) were irradiated by 450 fs laser pulses generated by a KrF excimer beam (248 nm) using the experimental set-up of Fig. 4.3. Note that the laser photon energy (5 eV) is far from the transition energy between the d-band and the Fermi-level of the noble metals Au and Cu. The autocorrelation configuration is a Michelson type interferometer in which the incident laser beam was separated in two parts by a 50-50 beam splitter, delayed in two perpendicular paths. The path of the laser pulse in the first branch of the autocorrelator is fixed, while the pulse in the second branch is delayed by moving the mirrors of the second branch with a micrometric translator, having a precision of 2 μm. Then, the two beams are joined collinearly and focused onto the same point of the target surface under an angle of incidence θ=80^o with a precision of 0.2^o, by a silica convex lens of 18.5 cm focal length at 248 nm.

The distance between the lens and the photocathode is fixed at 17.5 cm in order to get a sufficiently large spot area (in the order of 0.15 mm^2) as it is measured by a diode array. The zero delay between the two laser pulses was determined, when we obtained the best intensity contrast of the interference fringes of the two laser beams on a CCD diode array. The anode was charged up to 28 kV by means of a positive high voltage power supply, allowing production of an accelerating electric field up to 6.6 MV/m. The photocurrent was measured for applied high voltage from 0 to 28 kV by increments of 4 kV, in order to take in to account the space charge effect in the electron collection from the anode.

As previously observed the photoemission efficiency for s-polarized incident radiation was always lower than for p-polarization. Thus only p-polarization data are considered and are shown in Figs. 4.4, 4.5, 4.6, 4.7, 4.8 for the various cathodes and the various laser intensities.

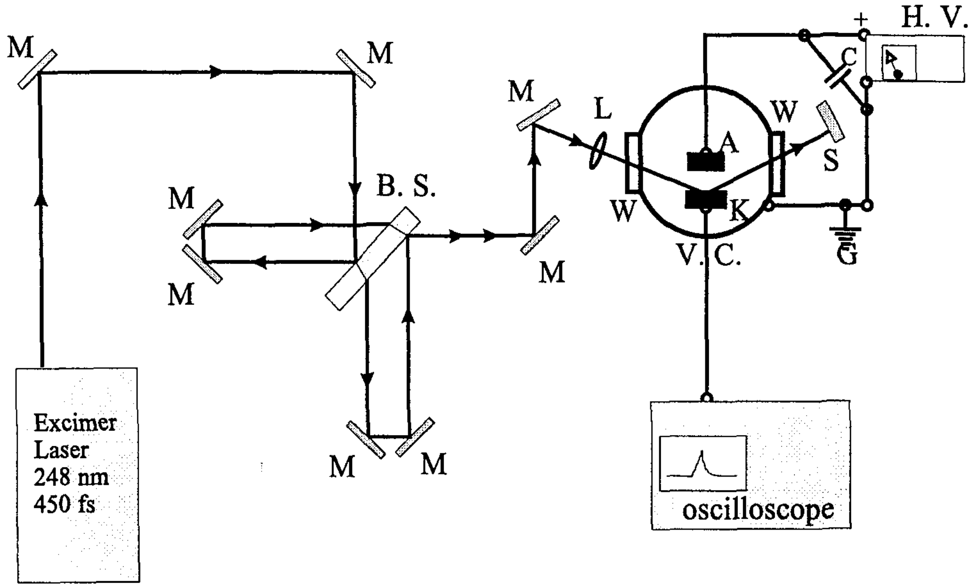

Figure 4.3: Experimental arrangement. M: mirrors; B.S.: beam splitter; L: lens; W: windows, V. C.: vacuum cell; K: photocathode; A: collecting anode; S: beam stop; G: ground; C: capacitor; H. V.: high voltage power supply.

Experimental points were measured in the following way: First the zero delay between the two output autocorrelation pulses is defined as previously described. Then, the optical delay of the laser pulse corresponding to the movable branch of the autocorrelator is changed stepwise. The produced photocurrent is measured for different values of the applied high voltage in order to avoid space-charge effects. At any value of applied voltage the photocurrent value is the average value of 50 consequent laser shots.

By changing the energy of the laser beam, a complete set of autocorrelation curves were obtained for every photocathode. The measurements are stopped at the delay for which the current was equal to the sum of the current produced by each pulse. For higher delays the photocurrent produced by the two laser pulses, remained constant.

In the next subsection is presented a phenomenological model that we introduced in order to analyze the experiments.

4.3.3 Theoretical-Model

I. Single-Photon-Autocorrelation (SPA)

For the classical (perturbative) single-photon electron emission, the photocurrent is a

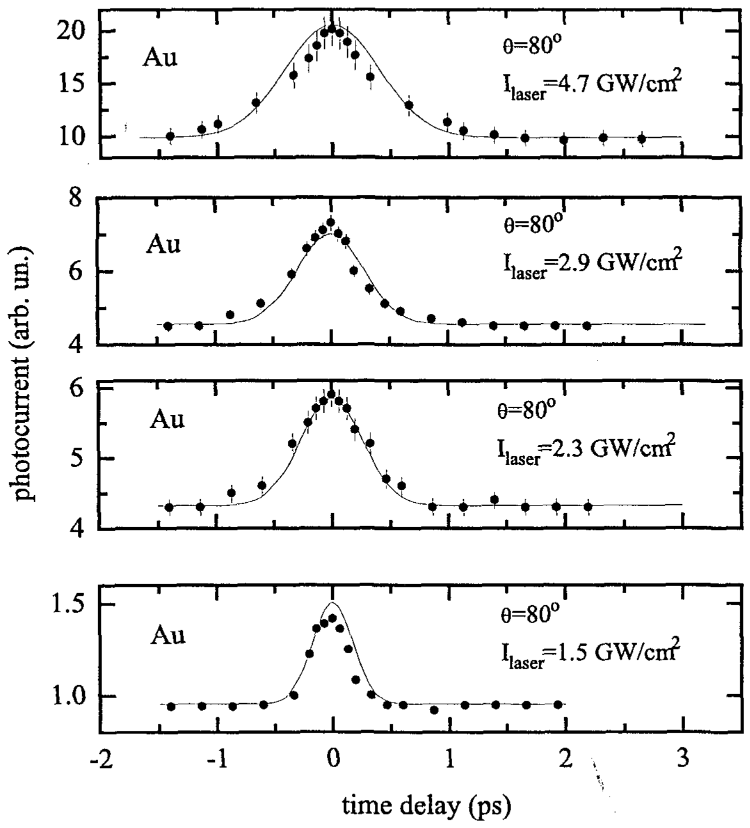

Figure 4.4: Photoelectron current density obtained from a gold surface as a function of the time delay between the two p-polarized KrF laser pulses (450 fs, 248 nm). The dots represent the experimental measurements and the lines the best fitting of the theoretical model. The electron cooling times increases as the laser intensity increases.

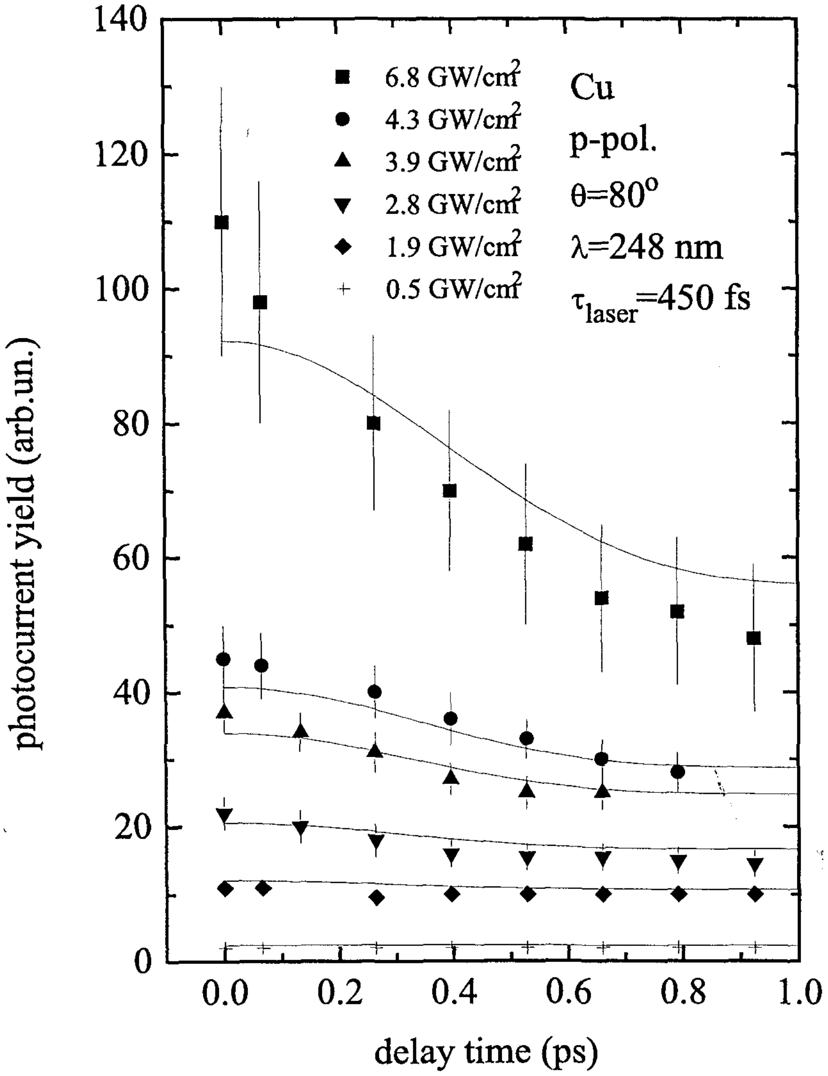

Figure 4.5: Similar to Fig. 4.4 but for a copper surface.

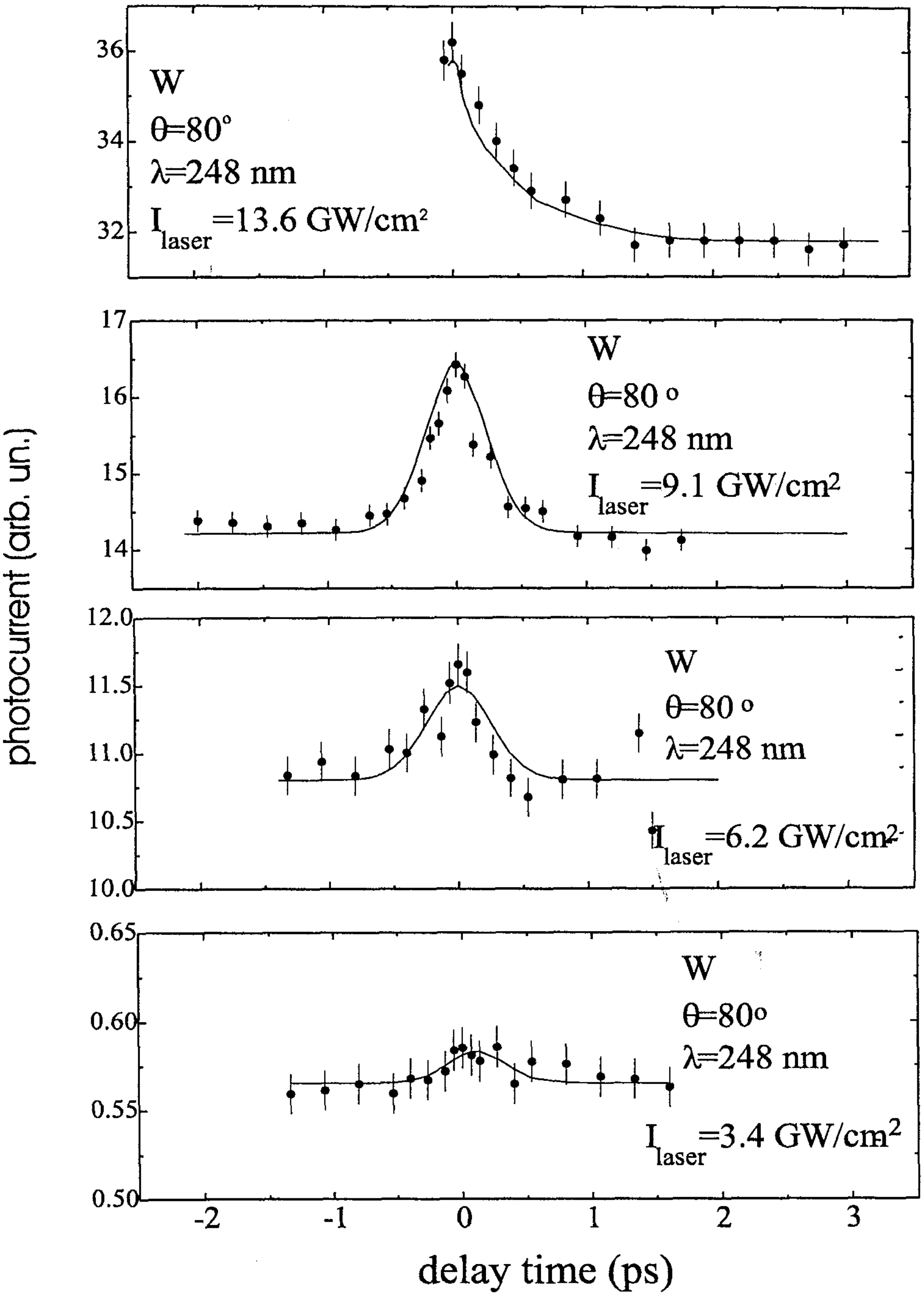

Figure 4.6: Same as Fig. 4.4 but for a tungsten surface.

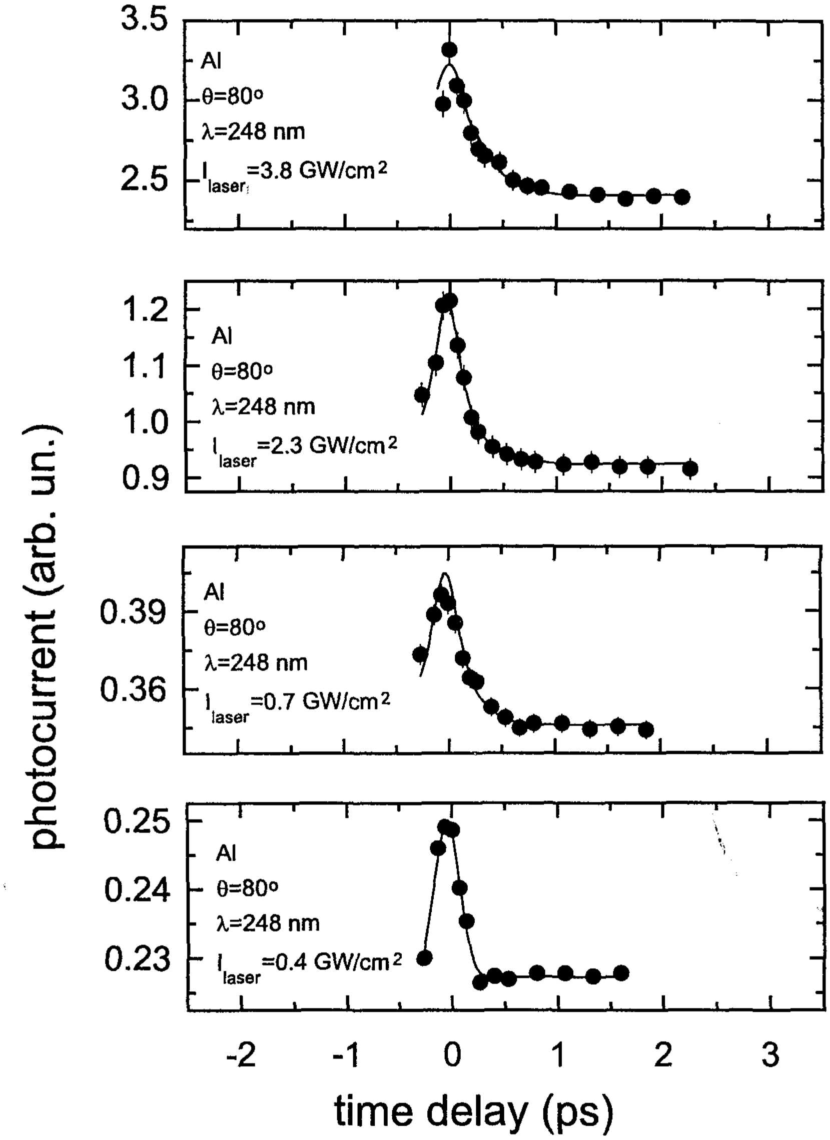

Figure 4.7: Same as Fig. 4.4 but for an aluminium surface.

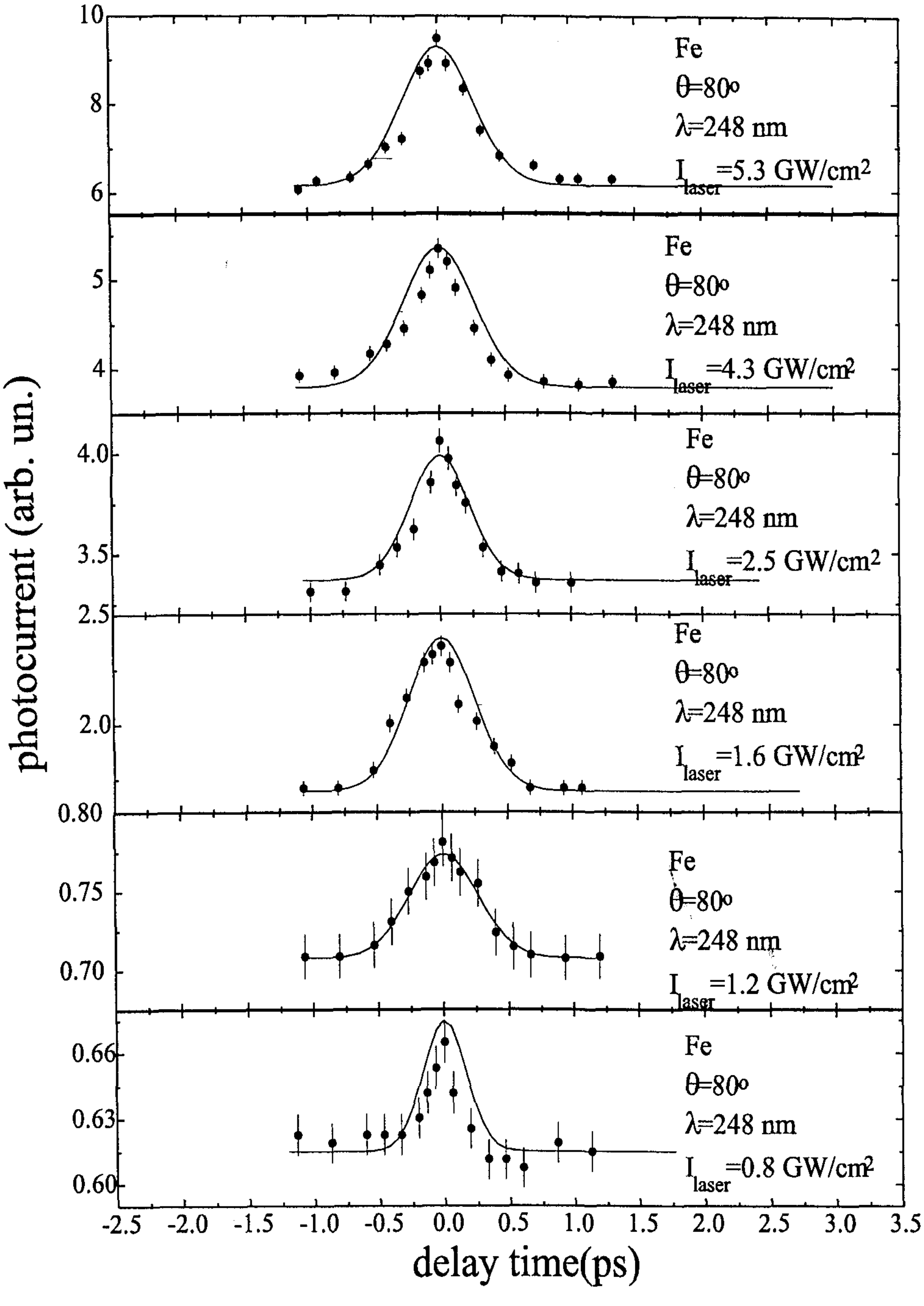

Figure 4.8: Same as Fig. 4.4 but for an iron surface.

linear function of the laser intensity. Thus, the autocorrelation curves must be flat because the measured photocurrent remains unchanged versus time delay between the laser pulses. The resulting photocurrent of the two laser pulses is a linear algebraic summation of the photocurrent of each laser pulse. The photocurrent signal in the linear case, is proportional to the laser intensity,

$$J \propto \int_{-\infty}^{\infty} |E(t) + E(t+\tau_d)|^2 dt \tag{4.3}$$

where the electric field is:

$$E(t) = \frac{1}{\sqrt{2}} |\epsilon(t)| e^{i(\omega t + \phi(t))} \tag{4.4}$$

Here, $\epsilon(t)$ is the temporal distribution of the amplitude of the electric field associated to the laser pulse, ω is the cyclic photon frequency, $\phi(t)$ is the phase of the electric field wave and τ_d the time delay between the two laser pulses of the interferometer. The coefficient $1/\sqrt{2}$ indicates that the initial laser beam is separated into two laser pulses of equal intensity. The cross terms in the integral of Eq. (4.3) contain rapidly varying phase factors these are proportional to $\cos(\omega\tau_d)$. To resolve these fast variations requires controlling the spatial variations on a scale of roughly 0.1 that of the wavelength involved [Sal80]. In practice only the slow terms are measured by this experiment. Thus the measured photocurrent is:

$$J \propto \int_{-\infty}^{\infty} |\epsilon(t)|^2 dt + \int_{-\infty}^{\infty} |\epsilon(t+\tau_d)|^2 dt. \tag{4.5}$$

Each integral in the above equation is proportional to the intensity of each laser pulse of the autocorrelator. The photocurrent J appears to be independent of τ_d. However, as we observed from the experiment, for intensities higher than a few 100 MW/cm^2, the experimental curves start to have a Gaussian-like shape. The origin of this non-linearity, was demonstrated to be the thermal non-equilibrium between the electron gas and the lattice induced by laser pulses on the metallic surfaces.

II. Calculation of electron and lattice temperatures

For the calculation of electron and lattice temperatures we follow the analysis presented in the chapter 2. As it was mentioned there, the unknown parameters are A and B. The laser pulse duration (450 fs) is relatively long compared to the electron-electron scattering time for typical electron temperatures (few thousands of Kelvin degrees). Thus, in the theoretical analysis we assumed that the electrons are always in thermal equilibrium, i.e., the electrons are rapidly thermalized in a Fermi-Dirac distribution after the laser pulse action and the refereed electron-electron and electron-phonon scattering times concern the thermal electrons.

On the other hand, in recent years several paper has been published which demonstrate the existence of non-thermalized electrons for several hundreds fs [Fan92a, Fan92, Sun93, Sun94, Lug94].

We follow the analysis of the reference [Fan92] for the non-thermalized electrons. The electron distribution function can be divided into a thermal and non-thermal part, $f = f_{th} + f_{nth}$. Energy is transferred from the nonthermal distribution to the thermal distribution by electron-electron scattering of the non-thermalized electrons, while electron-phonon and electron-electron scattering of the thermal electrons transfers the energy to the lattice. In this scheme, the direct transfer of energy from the non-thermalized electrons to the lattice is ignored. The thermal part is the Fermi-Dirac distribution and the non-thermal is governed by the equation [Fan92]:

$$\frac{df_{nth}}{dt} = -\frac{1}{\tau} f_{nth} + I^R(t) \tag{4.6}$$

Where τ is the scattering time of an excited electron, due to both elastic and inelastic collisions and $I^R(t)$ is the rate that the laser pulse generate the non-thermalized electrons. The scattering time of the non-thermalized electrons in the approximation $\delta E >> kT_e$, can be expressed as: $\tau = \tau_o (E_F/\delta E)^2$, where δE is the available energy space for the scattering and τ_o is a constant. The nascent distribution (f_0) is chosen as the initial condition for the non-thermal part and is expressed as:

$$f_o \approx f_{th}(E, T_e^o) + \xi f_{th}(E - \hbar\omega, T_e^o), \tag{4.7}$$

where E is the electron energy, T_e^o is the electron temperature in the maximum of the laser intensity and ξ is the probability of one photon being absorbed by one electron in a period equal to non-thermalized electron scattering time, τ, which is in the order of a few percent for the conditions used in our experiments.

In Fig 4.9 are shown the calculated electron distribution function of the electrons in a copper surface (τ_o=2 fs, E_F=7 eV, $\hbar\omega$ =5 eV) as a function of their energy and the time for the various laser intensities used in our experiment. We chose copper to perform this analysis for non-thermalized electrons because the experimental curves and the theory, without taking into account the non-thermalized electrons, have a satisfactory agreement in the whole range of the delay time, but have not so good agreement for times shorter than 100-200 fs (see Fig 4.5). This observation was systematic for the copper and thus we decide that it is interesting to perform calculations taking into account the non-thermalized electrons in order to find the origin of this disagreement.

The above calculations show clearly that the total electron thermalization time is between 50-150 fs in the conditions of the experiment for copper surface. The higher the intensity the faster the electron thermalization. The calculation is supported very well by the experiments. Concluding, one can say that to first approximation, the non-thermalized electrons which complicates the theoretical analysis, can be omitted.

III. Photocurrent calculations

The calculated electron temperature T_e by the Eqs. (2.12) was used in the Fowler-Dubridge Eq. (2.28) in order to determine the single- photon electron emission current. This equation explains the temperature dependence of photoemission near the work function threshold, with the assumption that the electrons in the metal obey the Fermi-Dirac statistics. An electron can escape from the metal, if the kinetic energy associated with its velocity normal to the surface, is greater than the potential energy barrier. For a single-photon electron emission the photocurrent is calculated by the equation:

$$J_1(t) = a_1(\frac{e}{\hbar\omega})(1-R)I(t)T_e^2F(\mu) \tag{4.8}$$

$$\mu = \frac{\hbar\omega - W}{k_BT_e(t)} \tag{4.9}$$

where a_1 is a constant proportional to the single-photon photoelectron cross-section, e is the electron charge, $\hbar\omega$ is the laser photon energy equal to 5 eV and $F(\mu)$ is the Fowler function which calculates the fraction of the electrons which are energetically allowed to escape from the metal surface absorbing a photon. The values of a_1 can be determined from experimental data.

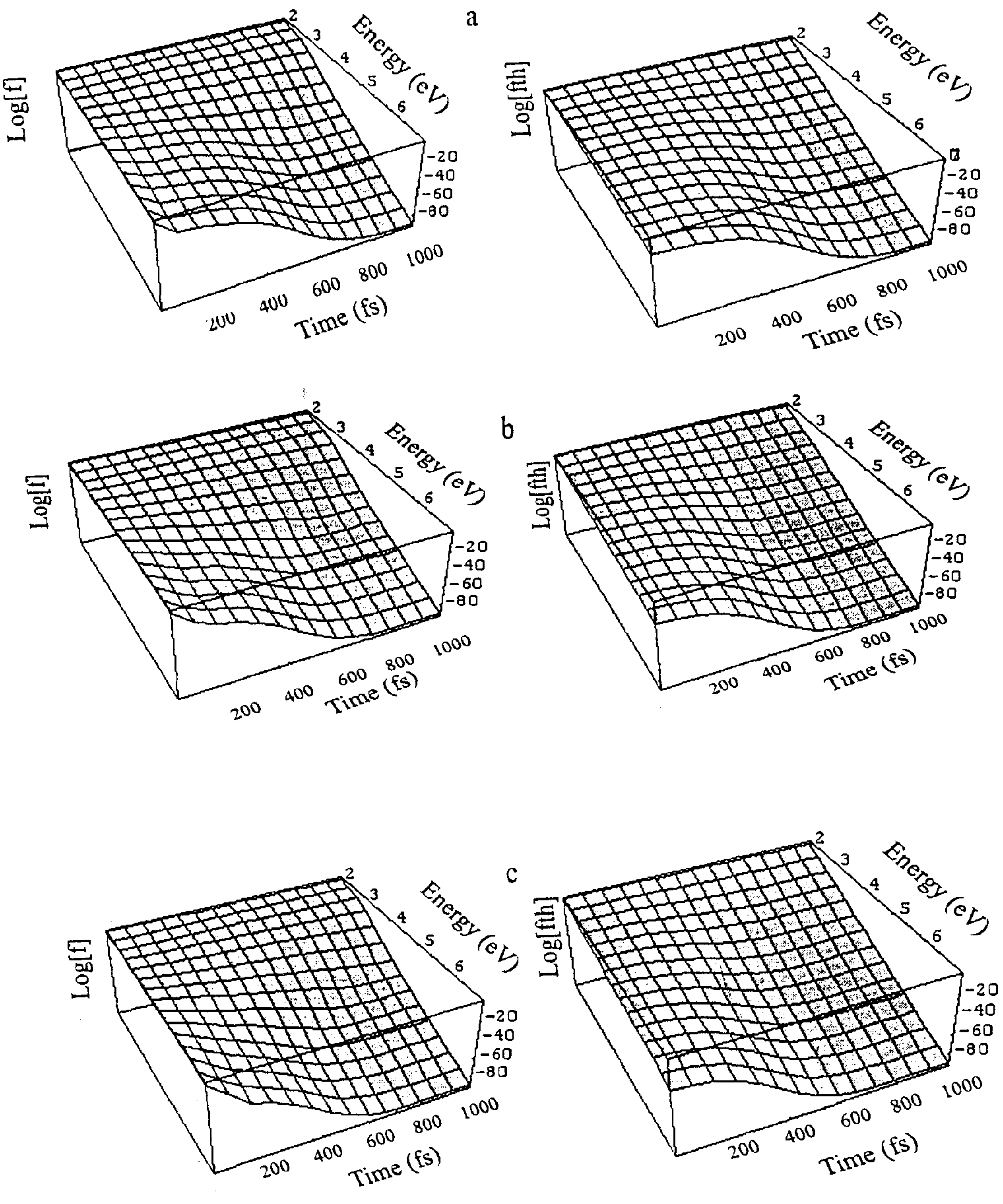

Figure 4.9: Right: Calculated electron distribution function ($f = f_{th} + f_{nth}$) for copper surface as a function of the initial electron energy (before the laser excitation) and versus time (the zero time is at laser pulse maximum) for laser intensity 6 GW/cm^2. Left: Same with the right part exept that only the f_{th} (Fermi-Dirac distribution) is plotted. The thermalization time is about 150 fs. b) Same with the (a) but for 3 GW/cm^2 laser intensity. The thermalization time is about 100 fs. c) Same as (a) but for 1 GW/cm^2 laser intensity. The thermalization time is about 50 fs.

In our experiments, all the electrons which escape from the metal were measured during the emission time, after the space-charge corrections. In order to compare with the model described earlier, we consider the total emitted charge density which is given by:

$$q = \int_{-\infty}^{\infty} J(t)dt \tag{4.10}$$

4.3.4 Results and Discussion

We have calculated from Eqs. (2.12) the electron and lattice temperatures for the different photocathodes at different intensities of the intensity of the Gaussian with 450 fs duration at FWHM laser pulses. The physical parameters for the different cathodes used, are presented in Table 4.1.

For the parameter A, the theoretical and experimental values are in the range of 10^6 to 10^7 $K^{-2}s^{-1}$ for most of the metals. The same order of magnitudes may be calculated from Eqs. (2.21). Similarly, the parameter B is calculated by Eqs. (2.21) to be in the order of 10^{11} $K^{-1}s^{-1}$ (λ_o=0.1-1). The best fit for A and B for the different photocathodes is presented in Table. 4.1. The time range from zero delay to the delay that the experimental autocorrelation curves become flat, is the electron cooling time. The experimental cooling times for the various metal vs the laser intensity are presented in Fig. 4.10.

It is shown that a hot electron gas (few thousands of Kelvin degrees) requires about 0.5-2 ps (is dependent on the experimental conditions) to relax again in its equilibrium state.

The cooling times of the different metals are in satisfactory agreement with the times observed by the mentioned works using the TTS technique. In reality the cooling times presented in this work is a slightly shorter than those presented in previous works of TTS. This behavior is explained because in our experiments we used thick (bout 1 mm) polycrystalline metals. As it was observed by H. E. Elsayed-Ali et. al. [Els91] the cooling time is inversely proportional to the metal thickness because faster diffusion into the phonon bath occurs in the case of thick metals. Also in the mentioned work it is shown that the electron cooling is faster in polycrystals than in monocrystals due to faster hot electron loss promoted by increased lattice imperfections.

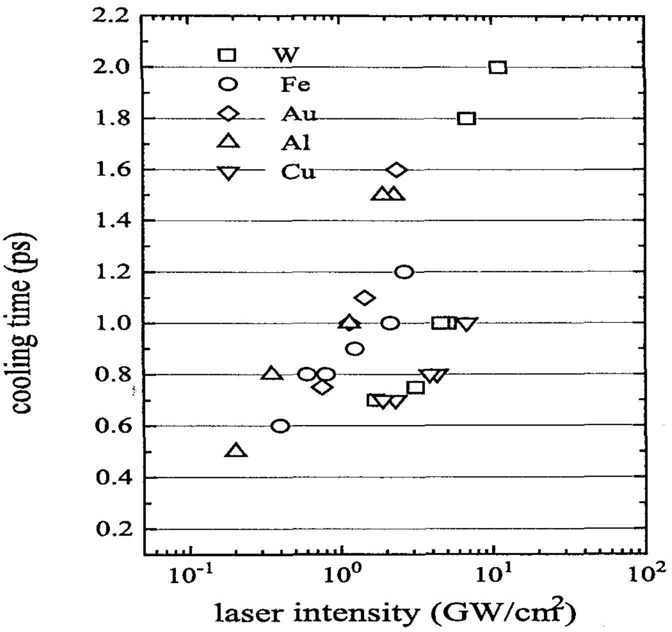

Figure 4.10: Experimental cooling times for various metals as a function of the laser intensity of the p-polarized UV (5 eV) laser pulse with 450 fs duration. The data are measured with the single-photon photocurrent autocorrelator method proposed in this thesis. Note that for all the metals the cooling times increases with the laser pulse intensity and have the values from 0.5 to 2 ps in the laser intensity range from 0.2 to 15 GW/cm^2.

Another important observation from Fig. 4.10 is that the cooling times for all the tested metals increase monotonically with pump laser intensity. The cooling time increases versus the laser intensity i.e., versus the electron temperature. This behavior can be explained in terms of collisional energy transfer from electrons to the lattice. A greater amount of electron energy requires more collisions to be transferred to the lattice. Similar behavior was partially observed by measurements in *W* [Fuj84].

The experimental autocorrelation data of the various metals, (Figs. 4.4, 4.5, 4.6, 4.7, 4.8) can be used to evaluate the electron-phonon scattering time as follows: For given values of A and B, we may compute the electron temperature, which is used in the Fowler-Dubrighe expression for photocurrent density (Eq. (2.28)) in order to calculate the total photocurrent J as a function of the delay time (τ_d) between the two laser pulses of the autocorrelator.

* * *	*Gold*	*Tungsten*	*Iron*	*Aluminum*	*Copper*
$\mathbf{n_R}$	1.484	3.400	1.298	0.190	1.470
$\mathbf{k_R}$	1.636	2.850	1.350	2.940	1.780
R	0.38	0.15	0.42	0.90	0.39
$\mathbf{n_o}(\times 10^{22} cm^{-3})$	5.90	37.93	17.00	18.10	8.47
$\mathbf{W}(eV)$	4.68	4.55	4.31	4.20	4.60
$\mathbf{E_F}(eV)$	5.51	18.08	11.1	11.7	7.0
$\mathbf{p}(grcm^{-3})$	19.7	19.3	7.9	2.7	8.9
$\mathbf{s}(msec^{-1})$	3240	5220	5950	6440	5010
$\mathbf{C_i}(Jgr^{-1}K^{-1})$	0.128	0.130	0.440	0.900	0.445
$\mathbf{a}(nm)$	25.7	10.1	15.0	14.6	20.1
$\mathbf{A}(\times 10^7 K^{-2} s^{-1})$	1.0 ± 0.2	2.0 ± 0.4	1.5 ± 0.3	4.0 ± 0.5	3.0 ± 0.7
$\mathbf{B}(\times 10^{10} K^{-1} s^{-1})$	10.0 ± 2.0	2.0 ± 0.3	3.0 ± 0.5	4.0 ± 0.5	1.0 ± 0.3

Table 4.1: Values of parameters used by the theoretical model in order to fit to experimental photocurrent autocorrelation curves for various metals. n_R and k_R are the real part and imaginary part respectively of the index of diffraction for the various metals at 248 nm [Pal85]. R is the reflectivity in the case of p-polarized at 80^o laser incidence calculated by the Eq. (1.30), for ($\phi = 0^o$, $\theta = 80^o$). n_o is th electron density [Ashb76]. W is the work function and E_F is the Fermi energy [Ash76]. p is the volume density. s is the transverse sound velocity [Crc88]. C_i is the lattice thermal capacity calculated by Dulong-Petit law. a is the penetration depth. A and B are estimated by the experiment parameters related to the electron-phonon and electron-electron collision times.

Varying the parameters A and B, the calculated photocurrent autocorrelation curves are fitted in the experimental autocorrelation data. The values of A and B used by theory in order to fit to the experimental data for the various metals are presented in Table 4.1. Both values A and B, are in the range of the expected order of magnitude.

Using the estimated (by fitting the theoretical model to experimental data) values of A and B, one can calculate the electron-phonon, τ_{e-ph} and electron-electron, τ_{e-e}, scattering time for any electron temperature. The electron-phonon scattering time τ_{e-ph}, for the various metals as a function of lattice temperature is shown in Fig. 4.11.

The observed cooling times are quite close for all the tested metals. Nethertheless, one can say that for a laser intensity of about 2 GW/cm^2 the cooling times of the different metals from the slower to the faster is for Au, Al, Fe, Cu, W respectively. This difference explains in part why the photoelectron emission yield (which are presented in chapter 2) of Au is higher than Cu, Al, Fe, W, even though the work-functions of Cu, Al, Fe, W are lower comparing to Au work-function, see Table. 4.1. Another physical parameter that reinforces

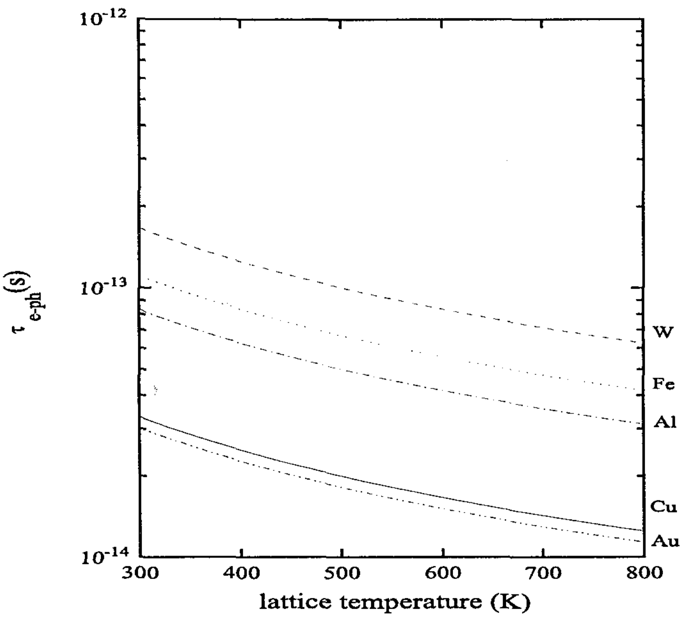

Figure 4.11: Electron-phonon scattering time as a function of lattice temperature for various metallic surfaces, estimated by the theoretical model (using parameters obtained by the experiment).

our measurements for the difference of the photocurrent yield is the penetration depth of the laser light (at 248 nm). As shown in Table. 4.1, the penetration depth of the p-polarized 248 nm laser photons vary proportionally to the observed photoelectric current yields of the various metals. A possible reason is that in a length equal to the penetration depth the electrons might absorb photons. Thus, the longer the penetration depth the more electrons may participate in photon absorption.

The calculated electron temperatures for the various metals in the range from 1 - 20 GW/cm^2 is presented in Fig. 4.12. As can be observed from this figure, the electron gas of Au acquires the highest temperature in this range. That is another reason for the high non-linearity that was observed in this metal as well as the high photocurrent yield.

Another point is that the electrons in the Al and Fe surfaces can not increase their temperature very much compared to the other tested metals, when they are illuminated by subpicosecond laser pulses in the intensity region of 1-50 GW/cm^2. This could explain partly the small value of the non-linearity observed in these metals as well as the smaller

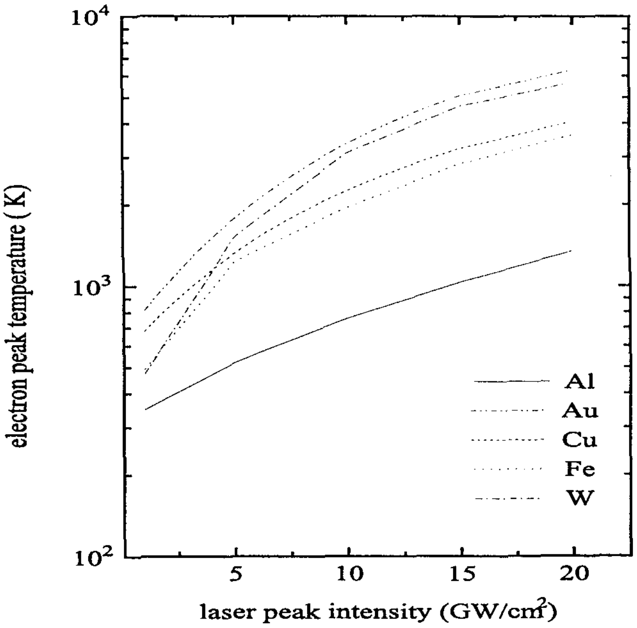

Figure 4.12: Electron peak temperatures for various metals calculated by the coupled thermal equations versus the laser intensity of the p-polarized at 248 nm laser pulses with duration 450 fs. The angle of laser incidence is 80°.

photocurrent yield in comparison with the Au. The electrons on a tungsten surface have a similar behavior with those of aluminium and iron for laser intensities up to 5 GW/cm^2. On the contrary when the laser intensity exceeds 5 GW/cm^2 the temperature of the electrons of tungsten increases very rapidly. This is the reason that the W does not acquire high non-linearity for low laser intensities (up to 5 GW/cm^2) but for higher laser intensities its non-linearity is very high.

Chapter 5

Short pulse measurements via multi-photon effects produced on metallic surfaces

5.1 Introduction

The time duration of very short pulses produced by picosecond or femtosecond laser cannot be measured by the common way of direct monitoring of photosensitive detectors (like photodiodes or photomultipliers or channel-plates), which have a response time, at best cases, of the order of a few nanosecond. In recent years there has been a growing interest in the development of solid state laser systems of ultrashort pulse duration [Spe91, Kel91, Spi95], thus leading to pulse durations below 100 fs, high laser peak intensities and broad frequency bandwidths. This fact gives rise to an imperative need for a precise characterization of these features of ultra-short laser pulses.

Since the late 1980's there has been a development of new autocorrelator techniques in order to achieve this goal. Although, it would be useful to develop a compact autocorrelator which could work independently from the wavelength, bandwidth and pulse duration of the laser and could provide both second and third order autocorrelation curves using the same experimental set-up and only one non-linear medium. Several techniques for ultra-short laser pulse characterization have been recently published [Nag89, Tre90, Bru91, Tre93, Kan94, Kav95, Kop95]. In former works, several techniques to provide pulse duration measurements (in most of the cases) or phase-sensitive studies of laser pulses have been presented. On the other hand, as far as we know, there is no work in simultaneously measuring pulse duration, amplitude and phase profile of ultra-short laser pulses. Additionally, most of the existing techniques are not applicable for the extended spectral range of existing laser systems, which in most of the cases, have a very broad spectrum.

The odd and even harmonics simultaneously generated on metallic surfaces, exhibit laser characteristics, continuous tunability and a slow decrease in the conversion efficiency concerning higher orders. Also, harmonics are unaffected by temperature relaxation phenomena occurred on the surface, when illuminated by femtosecond laser pulses having intensities of the order of a few GW/cm^2. All the above features led us to perform experiments for ultrashort laser pulse characterization based on harmonic generation from metallic surfaces.

The autocorrelator system is a Michelson type interferometer, in which the incidence laser beam is separated in two parts by a beam splitter. One of the two laser pulses is delayed or advanced in respect with the other, through an optical delay line, of a minimum resolution of 0.1 μm. The mixed pulses are used to induce a multi-photon nonlinear phenomenon. The yield of the non-linear phenomenon is measured for various overlaps and thus, one obtain the autocorrelation functions. Analyzing the autocorrelation functions, one can evaluate the temporal characteristics of fast laser pulses [Sal80].

5.2 Theoretical Analysis-Correlation Functions

5.2.1 nth-Order Cross Autocorrelation Functions

The general n^{th}-order fast autocorrelation function with background for n distinct light pulses having real electric field amplitudes

$$E_j(t) = \xi(t)cos[\omega_j t + \phi_j(t)], \tag{5.1}$$

(where $\xi(t)$ denotes the assumed pulse shape) is given by:

$$g_B^{(n)}(\tau_1, \tau_2, ..., \tau_n) = \frac{\int_{-\infty}^{\infty}[E_1(t) + E_2(t+\tau_1) + ... + E_n(t+\tau_{n-1})]^{2n}dt}{\int_{-\infty}^{\infty}[E_1^{2n}(t) + E_2^{2n}(t) + ... + E_n^{2n}(t)]dt}. \tag{5.2}$$

The denominator is chosen so as normalize the g_B^n to its background value [i.e., $g_B^{(n)}(\infty, \infty, ..., \infty)$ 1]. This correlation function is termed fast since it contains rapidly varying phase factors

$\propto cos(\omega_j, \tau_{j-1})$ in its various components.

Similarly, the nth-order zero background autocorrelation function is expressed as:

$$g_o^{(n)}(\tau_1, \tau_2, ..., \tau_n) = \frac{\int_{-\infty}^{\infty}[E_1(t)E_2(t+\tau_1)...E_n(t+\tau_{n-1})]^{2n}dt}{\int_{-\infty}^{\infty}[E_1(t)E_2(t)...E_n(t)]^{2n}dt} \tag{5.3}$$

The denominator has been choose to normalize again the function: $g_o^{(n)}(0,0,..,0) = 1$.

As explained in chapter 4, to resolve the fast variation inherent in the correlation functions defined above, it requires controlling the spatial variation on the scale of roughly 1/10 that of the shortest wavelength involved. The slow autocorrelation functions can be expressed as:

$$G_B^{(n)}(\tau_1, \tau_2, ..., \tau_{n-1}) =< g_B^n(\tau_1, \tau_2, \tau n - 1) >_{\tau,n} \tag{5.4}$$

$$G_o^{(n)}(\tau_1, \tau_2, ..., \tau_{n-1}) =< g_o^n(\tau_1, \tau_2, ..., \tau_{n-1}) >_{\tau,n} \tag{5.5}$$

The subscript B is for autocorrelation functions with background and the subscript o is for background-free autocorrelation curves.

Note that the slow autocorelation functions are solely determined by the time dependencies of the pulse envelopes $\xi_j(\tau_{j-1})$; all information regarding the phase perturbations $\phi_j(\tau_{j-1})$ is lost as a consequence of the failure of the slow correlation to resolve the much faster optical frequency variations $\propto cos(\omega_j \tau_{j-1})$. Usually, one mixes n replicas of a single pulse so that in the previous expressions one must replace the different pulses $E_n(t)$ with the same single pulse $E(t)$.

5.2.2 Second Order Autocorrelation Functions

In this subsection, we limit ourselves in the n=2 slow and fast autocorrelation functions, both with background and background-free which are express as:

$$g_o^{(2)} = \frac{\int_{-\infty}^{\infty} E^2(t)E^2(t+\tau)dt}{\int_{-\infty}^{\infty} E^4(t)dt} \tag{5.6}$$

$$g_B^{(2)} = 1 + \frac{2\int_{-\infty}^{\infty} E^3(t)E(t+\tau)dt + 2\int_{-\infty}^{\infty} E(t)E^3(t+\tau)dt + 3\int_{-\infty}^{\infty} E^2(t)E^2(t+\tau)dt}{\int_{-\infty}^{\infty} E^4(t)dt} \tag{5.7}$$

$$G_o^{(2)} = \frac{\int_{-\infty}^{\infty} \xi^2(t)\xi^2(t+\tau)dt}{\int_{-\infty}^{\infty} \xi^4(t)} \tag{5.8}$$

$$G_B^{(2)}(\tau) = 1 + 2\frac{\int_{-\infty}^{\infty} \xi^2(t)\xi^2(t+\tau)dt}{\int_{-\infty}^{\infty} \xi^4(t)dt} = 1 + 2\frac{\int_{-\infty}^{\infty} I(t)I(t+\tau)dt}{\int_{\infty}^{\infty} I^2(t)dt} = 2G_o^2 + 1 \tag{5.9}$$

where $I(t)$ is the optical pulse intensity. The contrast ratio for the slow second order correlation function with background, i.e., $G_B^{(2)}(0)/G_B^{(2)}(\infty)$, is 3:1.

A similar analysis for the peak to background ratios of the second order autocorrelation (slow) function is presented in this paragraph. The detected signal in a second order phenomenon (the yield of the phenomenon is proportional to the second power of the laser intensity) versus the delay between the two replicas of the laser pulse in the autocorrelation is expressed as:

$$D(\tau) = \int_{-\infty}^{\infty} [E(t) + E(t+\tau)]^4 dt \tag{5.10}$$

Using the Eq. (5.1) for the laser field the Eq. (5.10) takes the form:

$$\begin{aligned} D(\tau) = \int_{-\infty}^{\infty} |\xi(t)|^4 + \int_{-\infty}^{\infty} |\xi(t+\tau)|^4 + 4\int_{-\infty}^{\infty} |\xi(t)|^2|\xi(t+\tau)|^2 + \\ 4\int_{-\infty}^{\infty} [|\xi(t)|^2 + |\xi(t+\tau)|^2]|\xi(t)||\xi(t+\tau)|cos(\omega\tau + \phi(t) - \phi(t+\tau))dt \end{aligned} \tag{5.11}$$

The first two terms are the background signals produced by the two replicas separately ($\tau \rightarrow \infty$). The third term represents the slow background free autocorrelation function and the last term represents the fast background free autocorrelation function which can be measured, as explained from our set-up. It is again clear, that the contrast ratio for a slow autocorrelation function, the peak to background ratio is 3:1.

In the slow autocorrelation curves any asymmetry of the fundamental laser pulse is eliminated. The only information that one can extract is the pulse width. The initial pulse duration can be measured by the deconvoloution of the second order slow autocorrelation curve. In the Table 5.1 the autocorelation width (τ_p) as a function of the pulse width (τ_G) for various laser pulse shapes, is displayed.

Recall here (chapter 4), that the n=1 slow autocorrelation curve of the photocurrent

I(t)	ΔvΔt	$G_o^2(\tau)$	τ_p/τ_G
1. Square $I(t) = \begin{cases} 1 & \text{if } \lvert t\rvert \leq T/2 \\ 0 & \text{otherwise} \end{cases}$	0.8859	$= \begin{cases} 1 - \lvert\tau/T\rvert & \text{if } \lvert\tau\rvert \leq T \\ 0 & \text{otherwise} \end{cases}$	1
2. Diffraction function $I(t) = \frac{sin^2(t/T)}{(t/T)^2}$	0.8859	$\frac{3}{2(\tau/T)^2}[1 - \frac{sin(2\tau/T)}{2\tau/T}]$	0.7511
3. Gaussian $I(t) = e^{-(t/T)^2}$	0.4413	$e^{-(\tau/T)^2/2}$	0.7071
4. Hyperbolic sech $I(t) = sech^2(x)$	0.3148	$\frac{3}{sinh^2(\tau/T)}[(\tau/T)coth(\tau/T) - 1]$	0.6482
5. Lorentzian $I(t) = \frac{1}{1+(t/T)^2}$	0.2206	$\frac{1}{1+(\tau/(2T))^2}$	0.5000

Table 5.1: Second order autocorrelation functions; $G_o^2(t)$ and bandwidth products $(\Delta v\Delta t)$ for various pulseshape models (Ref. [Sal80]).

$(J(\tau))$, in the case that the photocurrent is a linear case ($J \propto I$) is expressed as:

$$J(\tau) \propto \int_{-\infty}^{\infty} [E(t) + E(t+\tau)]^2 dt = \int_{-\infty}^{\infty} |\xi(t)|^2 dt + \int_{-\infty}^{\infty} |\xi(t+\tau)|^2 dt + \\ 2\int_{-\infty}^{\infty} |\xi(t)||\xi(t+\tau)| cos(\omega\tau + \phi(t) - \phi(t+\tau)) dt \qquad (5.12)$$

The first two terms represent the current produced from each pulse separately (background signal). The third term is the slow background free autocorrelation function, which is not measured from our experimental set-up. Thus in the above case the curve $J(\tau)$ must be flat (see chapter 4).

5.3 Experiments

5.3.1 Experimental Review

The ultrashort pulse width measurements via autocorrelation is a technique known since 1966. The first work based on measurements of the second harmonic generation (SHG) on a doubling crystal for various delays of the overlapping replicas of the laser pulse [Mai66, Arm67]. After one year, a new method was reported, the two-photon fluorescence (TPF) [Gio67]. This method gives the advantage that it enables single-shot, single-pulse measurements, in contradiction with the SHG technique which requires several laser shots while varying path delays in order to produce a complete autocorrelation curve. In the following years a new method was proposed by D. C. Burnham [Bur70]. The non-linear photoelectric effect was used to measured picosecond light pulses by means the well known two-beam overlap technique.

There are many other reports on ultrashort pulse measurements. Most of the techniques are reported in the review invited paper of D. J. Bradley et al. [Bra74]. Most of the above measurements, as far we know, requires special conditions in order to be reliable. For example, the techniques of SHG by means of non-linear dielectric crystals are not directly applicable to ultraviolet lasers in the absence of suitable nonlinear media. The case of two-photon flourencence technique requires the use of a gas that has energy states close to the laser photon energy and/or the second harmonic of it, in order to enhance the flourencence signal.

Similar requirements appear in the case of multiphoton ionisation approach which on the other hand is the most applicable in the case of UV laser pulses [Ray82].

5.3.2 Experiments-Results

In this work a new method of ultrashort pulse temporal characterization based on the multi-harmonic generation and the multi-photon photoelectric emission produced on a gold surface.

For all our autocorrelation measurements the experimental set-up is the one described in previous chapters, in chapter 3 for harmonic generation and in chapter 4 for electron emission.

In the first experiment the laser used was the 450 fs, 496 nm dye laser. Thus, electron photoemission from gold is a two-photon effect like SHG. Second-order slow autocorrelation curves is investigated via measurements of the photocurrent emission signal or the reflected second harmonic signal from the Au surface. The effects are generated by the two equal light pulses as a function of the relative delay. The laser pulse is divided into parts by a 50-50 beam splitter. One of the two pulses is delayed or advanced with respect to the other by guiding it through an optical delay line with micrometric resolution. Both pulses are then collected into the scattering chamber in a quasi- collinear geometry and focused onto the same point of the target surface.

The tested pulses are the direct output of the excimer pumped dye laser system, which are of the order of 0.5 ps and by inserting an thin etalon in the dye laser arrangement it is modified to about 5 ps because of the multi- reflections of the fundamental pulse on both sides of an etalon plate. This is the reason why the produced by the etalon pulse is expected to have a multipeak structure.

As a first check, we perform laser pulse duration measurements using the SHG obtained from a dielectric doubling crystal (BBO). Following, we repeat pulse duration measurements via SHG or TPE obtained from the gold surface and then we compare the results with those obtained by BBO. The autocorrelation curves for both pulse durations obtained from the SHG in the BBO are shown in Fig. 5.1 and Fig. 5.2. The autocorrelation curve for the shorter pulse can be fitted to a Gaussian curve. The contrast ratio is 3:1 as is expected by a slow autocorrelation curve analysis of the previous section. The FWHM of the above autocorelation curve is τ_G=630 ± 20 fs. Then, according to the Table 5.1, the laser pulse duration is calculated to be τ_p=445 ± 14 fs.

The longer autocorrelation curve has a multi-peak structure with a Gaussian envelope which is expected because of the modification of temporal pulse profile by the etalon. It consists from several Gaussian-like peaks. Two of them are shown in Fig. 5.2. The FWHM of the Gaussian envelope of the whole autocorrelation curve is τ_G=6.4±0.3 ps, i.e., the respective laser pulse has duration τ_p=4.5±0.2 ps. The FWHM of the Gaussian-like peaks that consist the longer pulse are also Gaussian curves with a width equal to about 0.5 ps.

The next step is to measure the pulse width using SHG produce on the Au surface. The experimental conditions are the ones refereed in chapter 3; (p-polarization, grazing incidence). Figure 5.3 shows the autocorrelation curve for the shorter pulse. The curve fits to a Gaussian with a FWHM equal to τ_G=620±20 fs i.e., τ_p=438±14 fs which is in very good agreement with the autocorrelation curve measured by the classical way, i.e., with SHG on a BBO crystal. Similar results are obtained in the case of longer laser pulse. The

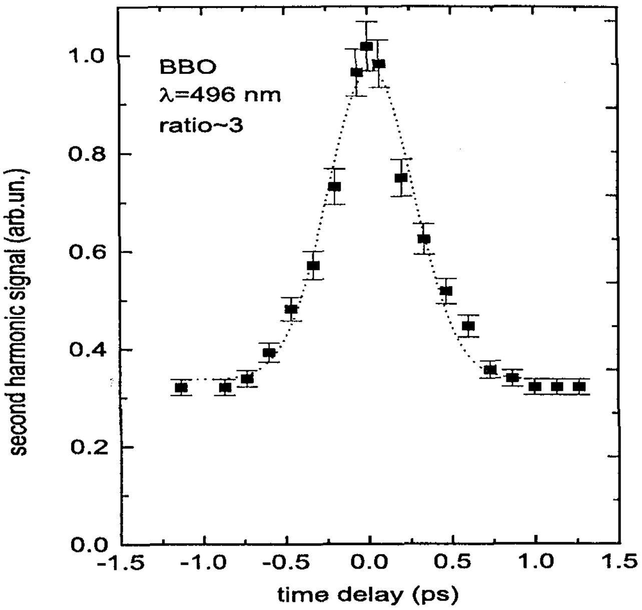

Figure 5.1: Second order autocorrelation curve, i.e., second harmonic generation on a BBO crystal, as a function of the relative delay of the two superimposed pulses. The FWHM of the laser pulse duration is 450 fs as derived by a Gaussian fitting. The peak to background ratio for the autocorrelation curve is 3:1.

autocorrelation curve obtained by SHG on Au using the longer pulse is presented in Fig. 5.4.

The structure of the autocorrelation curve using this method is similar to the BBO method. The FWHM of the Gaussian like envelope agrees with the one measured by the other method. The above measurements prove that the SHG on metals can be used in order to measure the pulse widths of femtosecond laser pulses.

It is important to recall here, that the tested laser pulse must have an intensity lower than the threshold of the extra non-linearity (higher than 2) observed by the experiment which is presented in chapter 3. Otherwise, the autocorrelation curve shape changes completely and the theoretical analysis presented in this chapter is not valid and another more complicated analysis is required in order to analyze the experimental autocorrelation curves. There are two easy techniques to check whether the laser intensity exceeds the previous threshold or not. The first is to verify that the contrast ratio is 3:1. The other is to measure the whole intensity dependence curve for the second harmonic generation from Au and to prove that

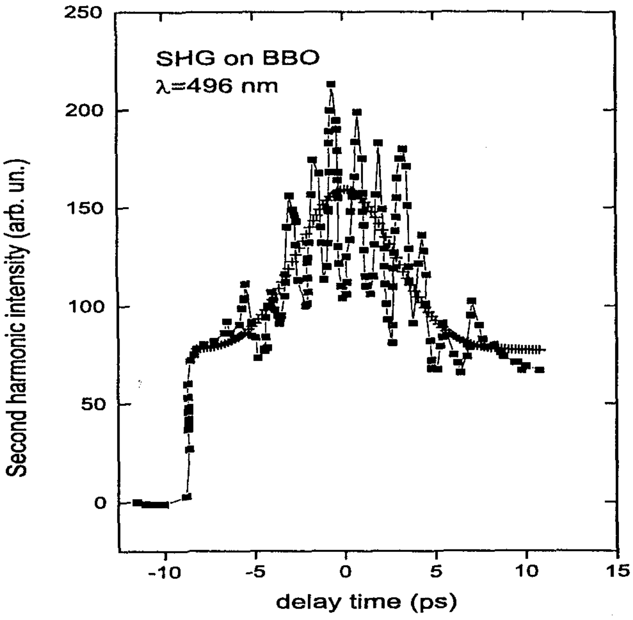

Figure 5.2: Similar to figure Fig. 5.1 except that the tested laser pulse has a multi-peak temporal profile with a Gaussian envelope having a FWHM at 4.5 ps duration.

the non-linearity is the one expected by the perturbation theory for the SHG, i.e., 2.

Since it was not possible to measure the third harmonic of the 496 nm dye laser pulse due to the wavelength limit of our detection system, third order autocorrelation curves were measured using the ≈800 nm wavelength of a Ti:sapphire laser. This laser is probably the most successful laser medium used in ultrafast laser pulse technology because of its broad gain bandwidth (about 200 nm) and excellent mechanical and thermal properties [Spi95].

The Ti:sapphire laser used in this work, provides pulses of duration of about 100 fs at 798 nm. The repetition rate of the system was 82 MHz. The non-linear medium was a 4-μm-thick polycrystalline mirror-like gold surface. The second harmonic signal was detected by a lock-in amplifier, that allows to measure signals as low as few μV.

Initially, we measured the laser pulse duration by the second order slow autocorrelation curve obtained from the second harmonic generation. Typical results are shown in Fig. 5.5. The peak-to-background ratio is 2.8:1 which is close enough to the expected ratio, 3:1, for slow second order autocorrelation curves. The small difference is due to the fact that the

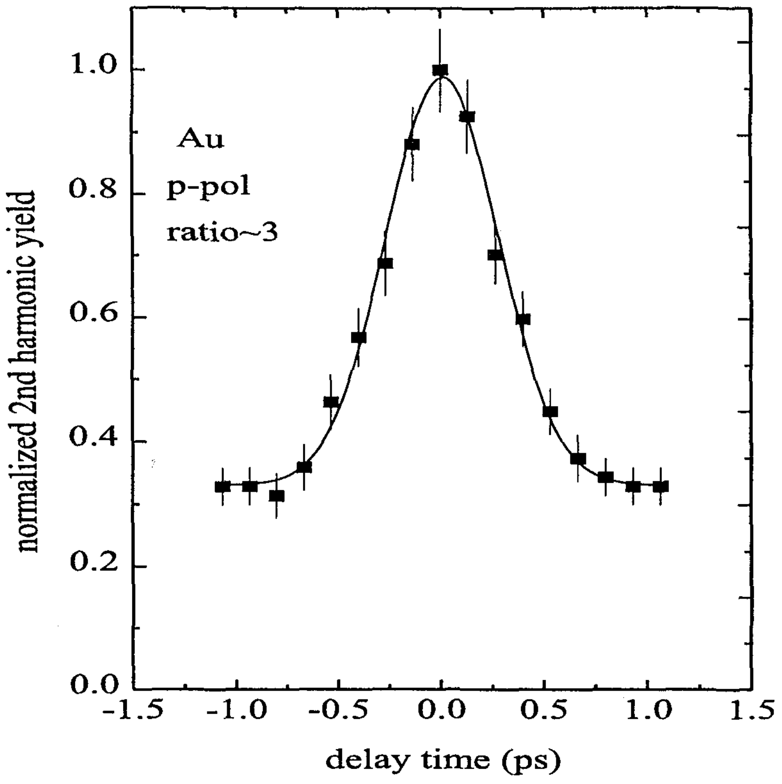

Figure 5.3: Second harmonic generation from a Gold surface vs relative time delay between the equal pulses of the autocorrelator. The laser intensity was 10 GW/cm^2. Superimposed is the best theoretical fitting curve for the purely second-order slow autocorrelation curve. The FWHM of the autocorrelation curve is τ_G=(639 ± 30) fs, i.e., τ_p=452 fs.

two pulses of the autocorrelator were not of exactly the same energy (energy ratio=8:10).

The experimental autocorrelation curves are fitted well both to a Gaussian curve and to the second order fast autocorrelation function for $sech^2(t/T)$ fundamental laser pulses, that is:

$$3\frac{(\tau/T)coth(\tau/T)-1}{sinh^2(\tau/T)}. \tag{5.13}$$

The laser pulse duration obtained by the autocorrelation curve is 100±2 fs for the Gaussian fitting and 91.5±2 fs for the $sech^2$ case [Sal80].

Simultaneously, we obtained the laser pulse spectrum which is presented in Fig. 5.6. The FWHM of the Gaussian-like spectrum is 7.6 nm. The product $\Delta\nu$ Δt is found to be 0.410 for the Gaussian case and 0.375 for the $sech^2$ case. $\Delta\nu$ is the FWHM of the laser spectrum, while Δt is the measured laser pulse duration. According to the calculation presented in Ref.[Sal80], assuming a Gaussian laser pulse temporal profile, the previous product should be 0.4413, while for the $sech^2$ case is 0.3148. Note that, for any other temporal profile type,

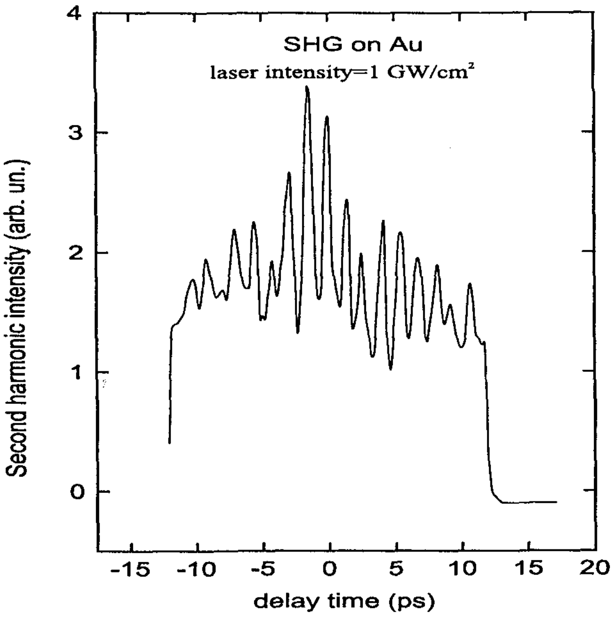

Figure 5.4: Similar to the Fig. 5.3 except that the laser pulse is the one described in Fig. 5.14.

the above product is much different [Sal80]. Thus, it is obvious to infer that the Ti:sapphire laser pulses have a duration of about 100 fs with a temporal profile between a Gaussian and a $sech^2$ function.

Similar results for the second order slow autocorrelation curves with background, were observed using the second harmonic generation in a BBO crystal. The results are plotted in Fig. 5.7. The laser pulse profile is again Gaussian with a FWHM of 101 fs. This confirms that the autocorrelation curves measured via harmonic generation on gold did not contain any relaxation phenomena that might destroy its shape and, consequently, the pulse width measurements.

The movable branch of the autocorrelator can move with a minimum step of 0.1 μm. Since the laser wavelength is 0.8 μm, we were able to measure fast autocorrelation curves which give additional information for the phase of the laser pulse and contain the rapid oscillations of the term $cos(\omega\tau)$. These curves (interferometric autocorrelation curves) can show the variations of the phase of the electric field. One of them is shown in Fig. 5.8a. The inset

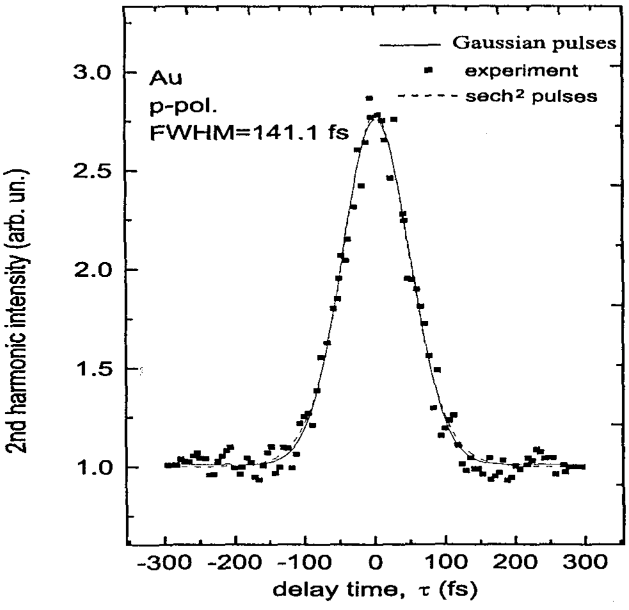

Figure 5.5: Slow second order autocorelation curve obtained by second harmonic generation on a gold surface by Ti:sapphire laser pulses. Both Gaussian and $sech^2(\tau)$ pulse function types are fitted well to the experimental data. According to the data, the FWHM of the fundamental pulses is 100±2 fs for the Gaussian and 91.5±2 fs for the $sech^2$ case.

of the latter figure displays the period of the amplitude variations of the electric field which is 2.7 fs. This value is in excellent agreement with the period of the 800 nm wavelength laser pulse, which is 2.67 fs. Figure 5.8b, shows the Fast Fourier Analysis (FFA) of the fast autocorrelation function. The phase of the electric field is constant with fluctuations around zero, but the main result of the FFA is that it confirms that in the fast oscillating autocorrelation function of Fig. 5.8a, the basic frequency is the one of the laser pulse, 3.75×10^{14} Hz. The FWHM of the amplitude of the FFA is 5×10^{12} Hz which is 10 nm in wavelength, roughly equal to the laser pulse bandwidth, see Fig. 5.6.

Similar results for the fast autocorrelation function were obtained using the second harmonic of the laser pulse from a BBO doubling crystal. These results confirm our measurements and our analysis of the fast second order autocorrelation function obtained from the gold surface. The BBO case is shown in Fig. 5.9.

Assuming a Gaussian temporal profile for the function $\xi(t)$ of the Eq. (5.1) and a linear

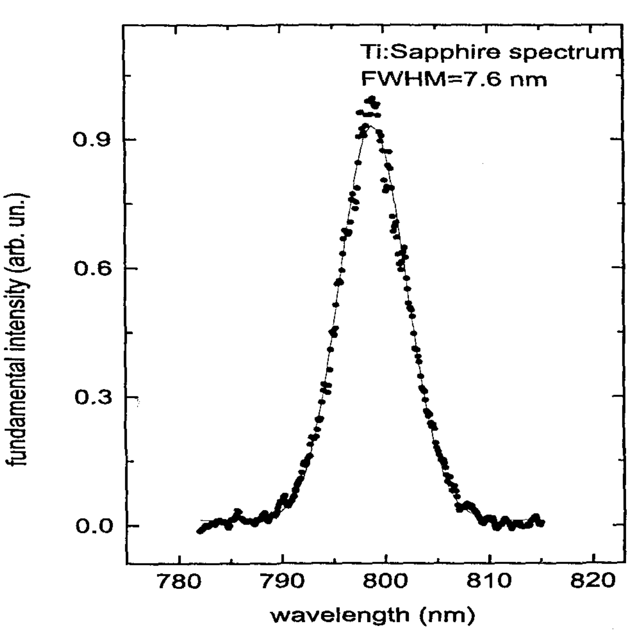

Figure 5.6: Spectrum of the Ti:sapphire laser pulses used for the autocorrelation function measurements. The profile is roughly Gaussian with 7.6 nm FWHM.

phase 'chirp' i.e., $\phi = at^2/T^2$ the corresponding second order fast autocorrelation curves for various a are shown in the Fig. 5.10. T is the characteristic time of the Gaussian $e^{-(t/T)^2}$.

The expression for the above fast autocorrelation function is:

$$g_B^2(\tau) = 1 + 4e^{-(3+4a^2)\tau^2/8T^2} cos(\omega t) cos[a^2\tau^2/2T^2] + \\ +e^{-(1+4a^2)\tau^2/2T^2} cos(2\omega\tau) + 2e^{-\tau^2/2T^2}. \quad (5.14)$$

In general, the theoretical curve for a=0 and the experimental fast autocorrelation curve are in satisfactory agreement. The main difference is that the experimental curve has a peak to background ratio equal to about 6:1 while the theoretical has 8:1. This difference is attributed to the fact that in the experiment the two autocorrelator pulses were not identical in energy. The one is 0.8 of the other. This is shown clearly in the signals of the second harmonic in Fig 5.8.

For the above experimental and theoretical fast second order autocorrelation curves is clear that our Ti:sapphire laser pulses are fully coherent, with no considerable phase chirp,

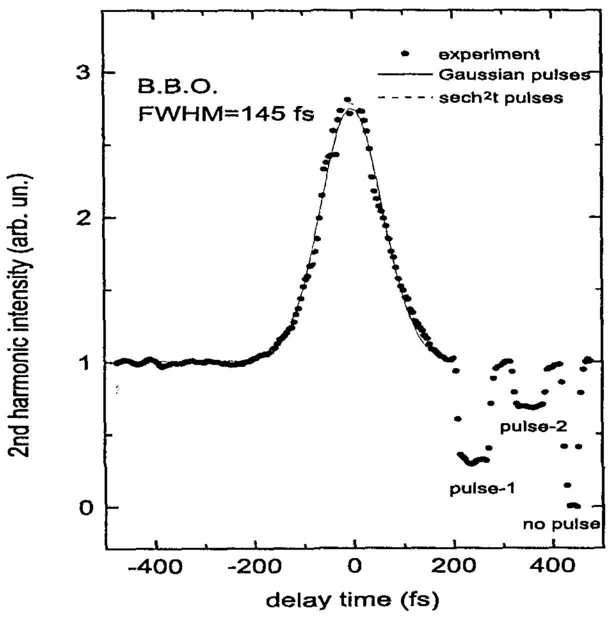

Figure 5.7: Slow second order autocorrelation curve obtained by the second harmonic generation in a BBO crystal. The FWHM autocorrelation curve is 145±3 fs i.e., for Gaussian laser pulse is 102.5±2 fs and for $sech^2$ is 94±2 fs.

having duration of 100 fs duration and with temporal profile between Gaussian and $sech^2$

Up to now, there is no information for a possible pulse temporal asymmetry. The second order autocorrelation function can not give any information for laser pulse asymmetry since it is fully symmetric in any case, even if the laser pulse has an asymmetric profile. The asymmetry of laser pulses can be deduced by third order autocorrelation measurements [Bau77].

Considering two laser pulses with intensity temporal profiles $I_1(t) = I(t)$, $I_2(t) = RI(t)$ where R is between 0 and 1, the third order slow autocorrelation curve (TOAC) is expressed as:

$$T^3_{slow}(\tau) \propto (1 + R^3) < I^3(t) > +9R < I^2(t)I(t + \tau) > +9R^2 < I(t)I^2(t + t) > \quad (5.15)$$

where <> denotes time average (t) and τ is the time delay between the two laser pulses. The peak to background ratio, r, of the slow third order autocorrelation function is given by

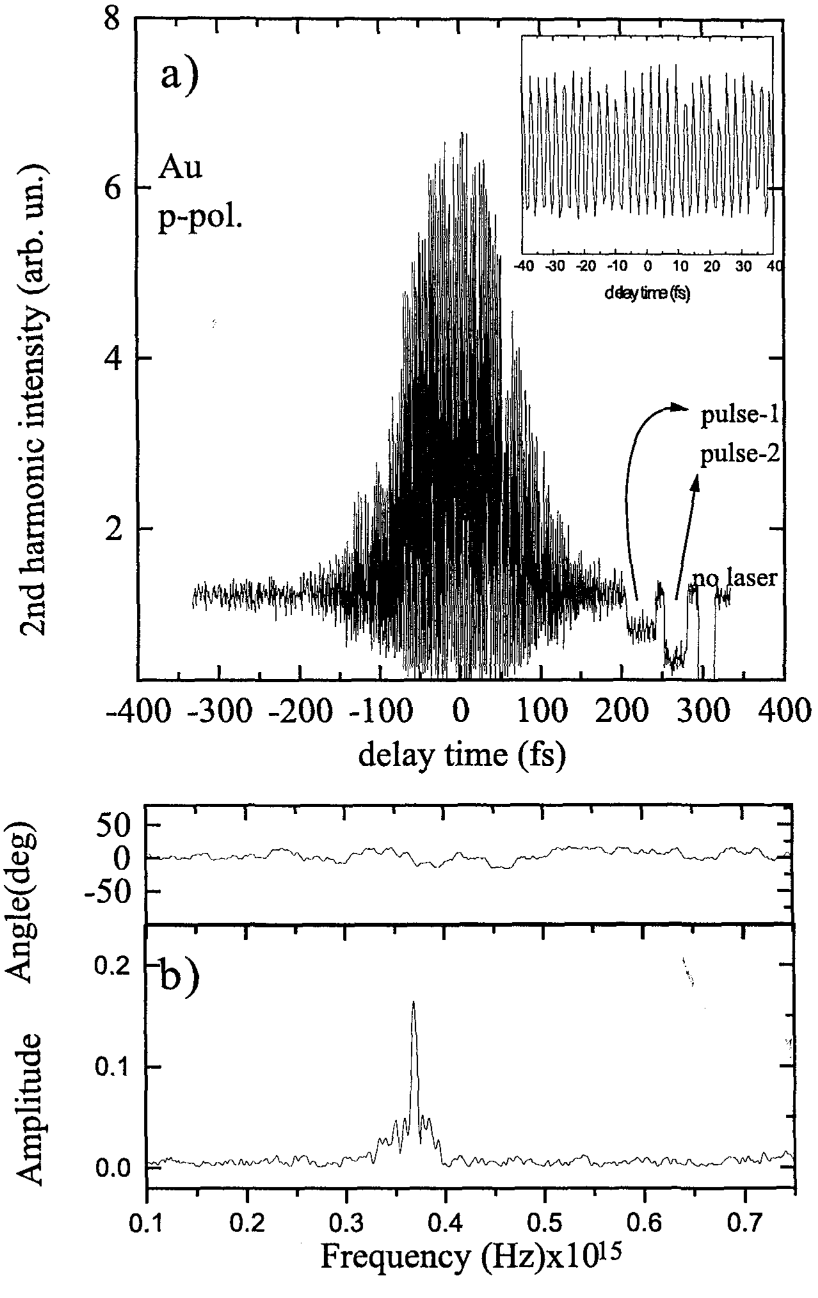

Figure 5.8: a) Fast second order autocorrelation curve for 100 fs Ti:Sapphire laser pulses obtained for second harmonic generation from a gold surface. Inset: Expand area from -40 fs to 40 fs delay time. The oscillations of electric field are observed; the period of these oscillations is 2.7 fs. b) Fast Fourier Analysis of the curve in (a). The phase has no considerable chirp and the amplitude is maximized at the frequency 3.7×10^{14} Hz. This is the frequency of the 800 nm laser pulses.

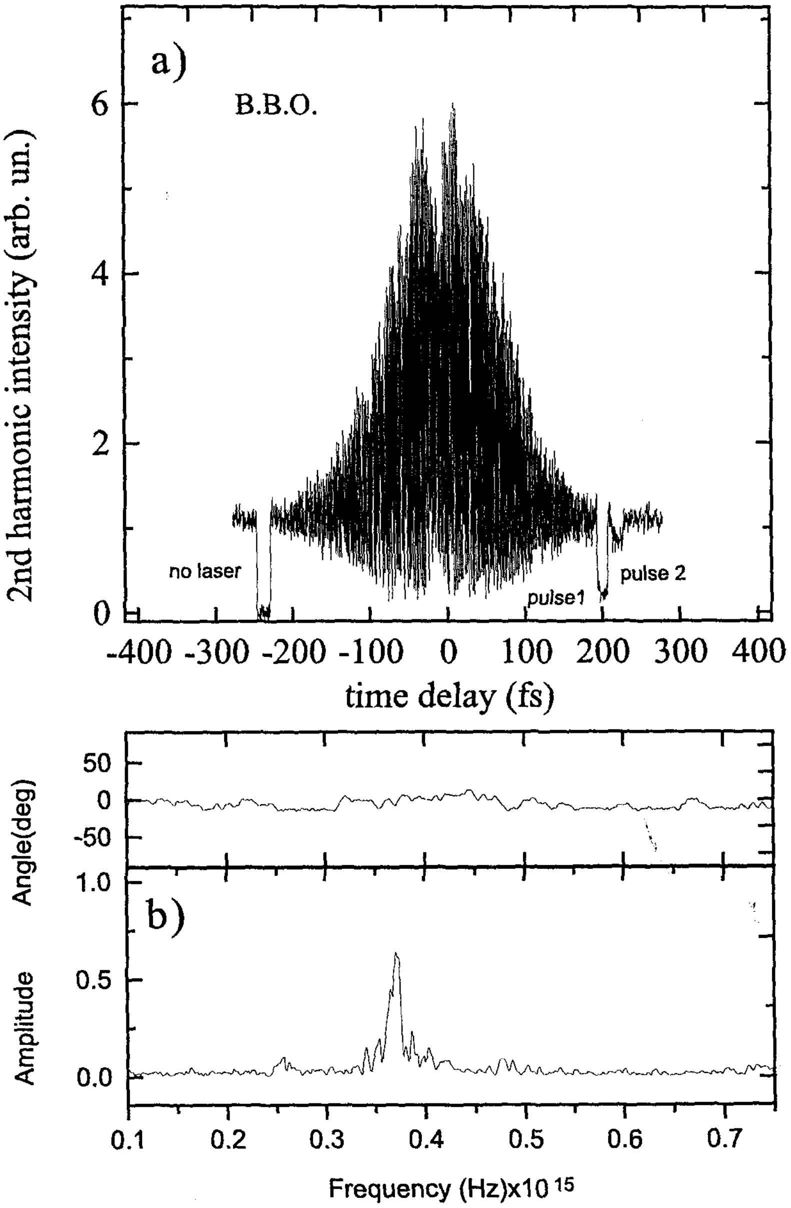

Figure 5.9: Similar with the Fig. 5.8 but the second harmonic is obtained from a BBO crystal.

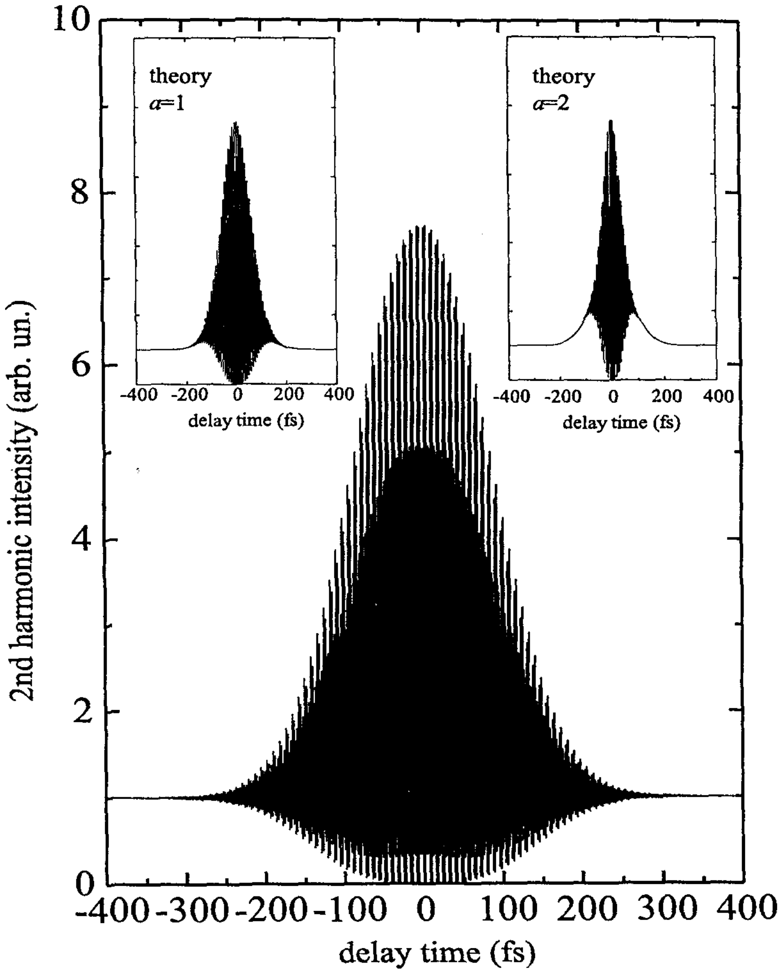

Figure 5.10: Theoretical calculations for the second order fast autocorrelation function for two identical Gaussian laser pulses. The FWHM of the slow varying envelope is set equal to 110 fs and wavelength 800 nm. The phase of the electric field is constant and equal to zero for the main figure and it has a linear chirp with different values for the parameter a for the two small insets.

the equation:

$$r = \frac{1 + R^3 + 9R + 9R^2}{1 + R^3} \tag{5.16}$$

For R=1 equal laser pulses the r=10.

Experimentally, the measurements of TOAC require a third order phenomenon in which its internal relaxation processes do not influence the TOAC measurements. In the past, for TOAC measurements the three photon fluoresence was proposed [Bau77]. Such measurements require a triangular configuration and a fluoresent media that exhibits resonance near 3ω, where ω is the laser photon frequency [Bau77]. Another method which was used in the past is the optical Kerr effect which is described by a third order polarization [Dah71]. By using the optical Kerr cell, ions can construct an optical gate, i.e., a Kerr cell in which the birefringence is caused by powerful laser pulses.

Both effects for TOAC measurements are limited by the internal relaxation phenomena so that these methods can not be applied for ultra-fast laser pulses of the order of 100 fs. On the other hand, we already proved [Pap96] that the harmonic generation from metals, for laser intensities lower than 10 GW/cm^2 in the femtosecond regime, is insensitive to relaxation phenomena which take place on metallic surfaces. This fact gives an advantage to the use of surface harmonic generation for ultrafast pulse measurements and especially for TOAC measurements, where the dielectric doubling crystal's method can not be applied.

Then, the same experimental configuration as for the second harmonic was used and thus, we measured the third order slow autocorelation curve using the third harmonic generation on the gold surface. Typical results are shown in Fig. 5.11. This curve shows clearly that the laser pulse was, in a good approximation, symmetric. Suppose a fundamental laser pulse of the form

$$\frac{1}{(e^{-t/T_1}+e^{+t/T_2})^2}. \tag{5.17}$$

Then the asymmetry of the laser pulse is described by the ratio T_2/T_1. In the case where T_1=T_2=T, the pulse is the $sech^2(t/T)$, which is fully symmetric. The ratio T_2/T_1 is 1.00±0.05 (T=51.9 fs) which shows that the Ti:sapphire laser pulse was symmetric in a very good approximation. Recall that the slow third order autocorrelation curve can be expressed as:

$$I_{3\omega}(\tau)=(1+R^3)+9R[G_0^3(\tau)+RG_0^3(-\tau)] \tag{5.18}$$

where

$$G_0^3(\pm\tau)=\frac{<I^2(t)I(t\pm\tau)>}{<I(t)>^3}. \tag{5.19}$$

For $I(t)=sech^2(t/T)$ the $G_0^3(\tau)$ is expressed as:

$$G_0^3(\tau)=\frac{15}{2sinh^2(\frac{\tau}{T})}[-\frac{2}{3}+ctnh^2(\frac{\tau}{T})-\frac{\tau}{T}\frac{ctnh(\frac{\tau}{T})}{sinh^2(\frac{\tau}{T})}]. \tag{5.20}$$

Using the smallest step of our stepper motor (0.1 μm), we also obtained fast third order autocorrelation curves. The results are plotted in Fig. 5.12. In this curve we simultaneously observe the rapid oscillations of the laser pulse electric field with a frequency of 3.7×10^{14} Hz, which is the laser photon frequency, as well as its temporal profile symmetry.

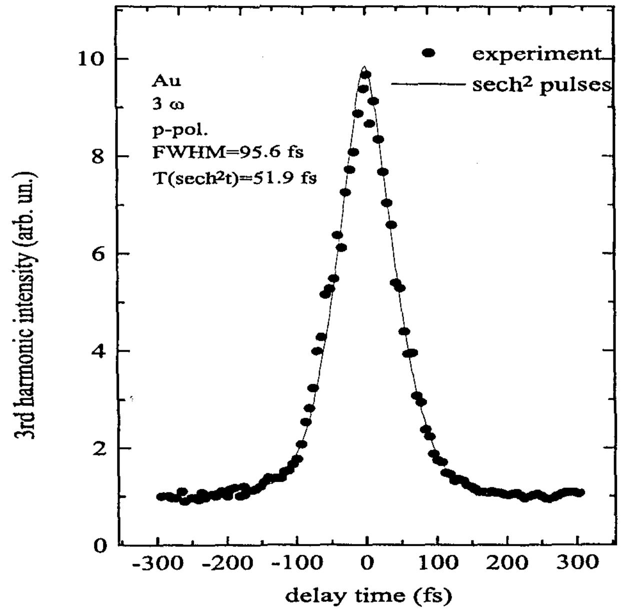

Figure 5.11: Third order slow autocorrelation curve measured by the third harmonic generation on gold surface (dots). The continuous line corresponds to the theoretical fitting (T=51.9 fs i.e.,$\tau_p(sech^2)$=91.5 fs). The laser pulse temporal profile is symmetric.

A second method for pulse width measurements of ultra-short lasers pulses proposed here is based on the two-photon photoelectric effects from a metallic surface. The experimental set-up is the same as in our previous experiments. Special care is taken to avoid the space charge effects mentioned in the experiments of chapter 2. Typical autocorrelation curves for the shorter and the longer pulse is present in Figs. 5.13, 5.14. The shape of both pulses are the same obtained from the SHG experiments on BBO and Au. The laser pulse widths measured by this method are 452 fs and 4.6 ps, respectively.

The results also prove that the two photon photoelectric effect in metallic surfaces can be used for pulse duration measurements. The notice for the extra-nonlinearity caused by the high electron temperature which is mentioned in the SHG case is again valid here. Nevertheless, in both methods the high laser intensity is not a serious problem. One can decrease the laser pulse intensity in the limits where the electrons temperature is close to 300 K where the laser pulse duration can be measured.

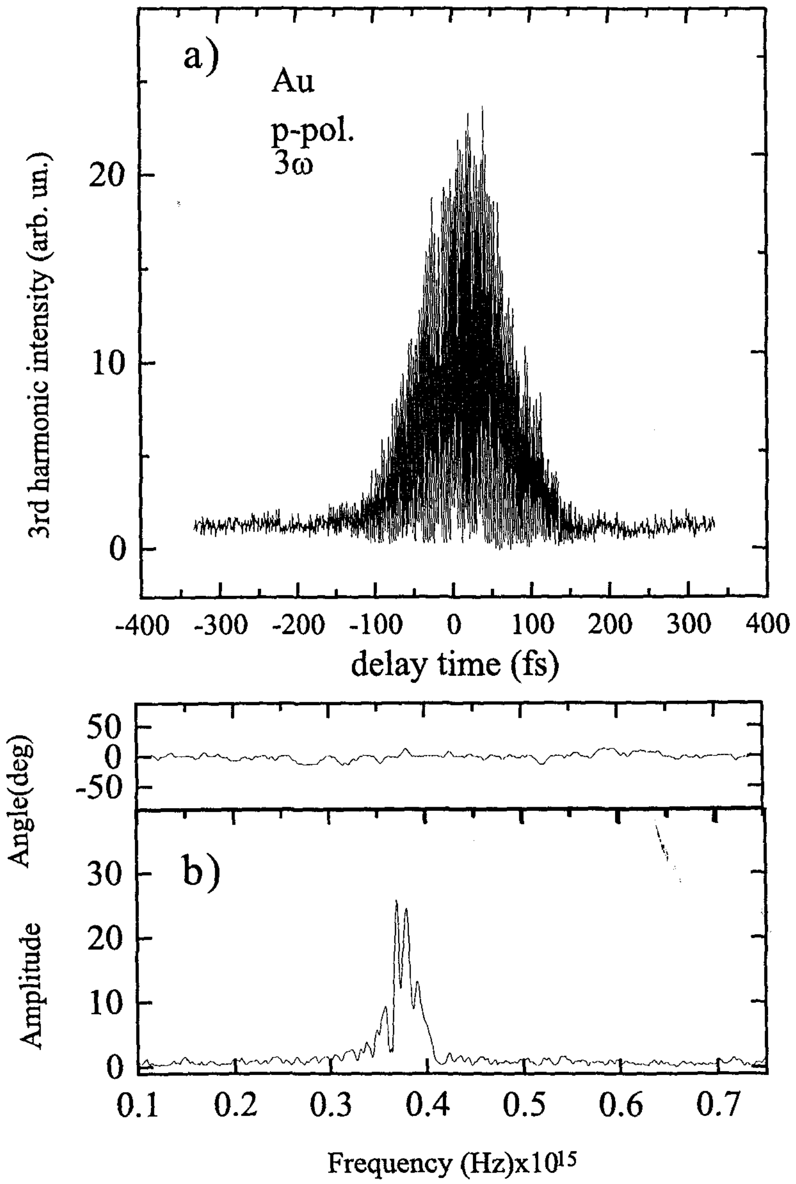

Figure 5.12: Third order fast autocorrelation curve obtained from the Au surface. The analysis is similar to Fig. 5.8.

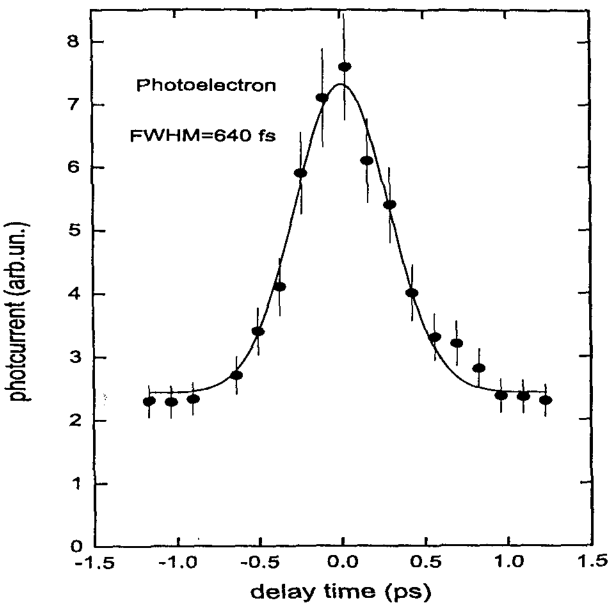

Figure 5.13: Two-photon photocurrent emitted from gold vs. relative time-delay between identical pulses for an intensity of 1.5 GW/cm^2. Superimposed is the the best theoretical fitting curve for purely second order autocorrelation. The FWHM of the above curve is (640 ± 30) fs and thus the FWHM of the laser pulse is 452 fs.

5.3.3 Conclusions

Concluding, one can say that the characterization of laser pulses using second and third harmonic generation produced on metallic surfaces has several advantages that make the method favorable for future use, especially for the ultrafast new generation solid state laser systems.

These advantages are:

a) In our previous studies we have shown that the tunability of the harmonic generation produced on metallic surfaces is from IR up to UV wavelengths. Consequently, the autocorrelation measurements based on harmonic generation on metallic surfaces are applicable over a wide spectral range. Especially for the ultrafast new generation solid state lasers having pulse durations as low as 10 fs and bandwidths of 100 nm, a favorable medium with such a tunability for nonlinear effects (harmonic generation) is the metals.

b) The electron relaxation phenomena do not influence the harmonic generation for intensities lower than 10 GW/cm^2, in the femtosecond regime. Hence, the measured second and third order autocorrelation functions contain only the amplitude and phase variations of the fundamental laser pulse and not other variations produced by relaxation phenomena on metallic surfaces. Thus, the time resolution in such measurements is not limited by the time duration of the pulse.

c) Another advantage of the method is the simplicity of the experimental set-up. The collinear geometry is easy to align and it is also easy to achieve zero delay. No special phase matching conditions are required for the metal surface harmonic generation, that could complicate the optical geometry. In fact, the harmonic yield depends on the sum of the refractive indexes of the two frequencies rather than their difference [She84]. Using exactly the same experimental set-up with just one non-linear medium (the metallic surface), one can obtain the fast and slow, second and third order autocorrelation functions and the fundamental spectrum as well as the spectrum of the second and third harmonic.

It should be noted that in the examples presented in this work, not all the possibilities of the method are used. For example, it is possible to perform online time-resolved measurements similar to those presented here.

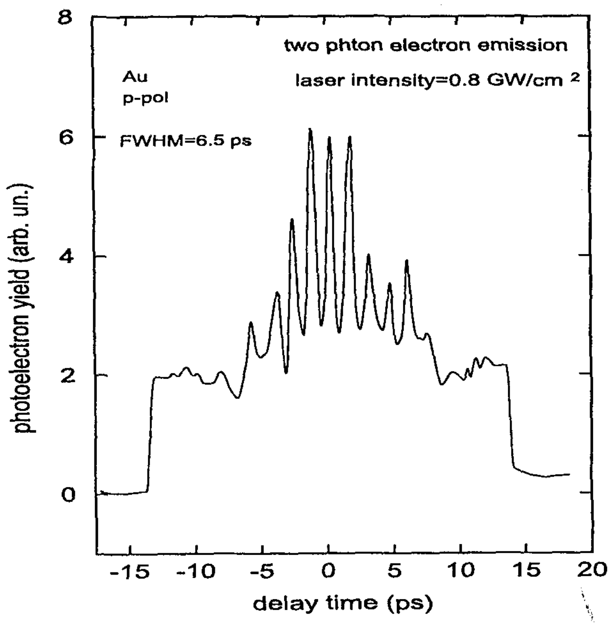

Figure 5.14: Similar to Fig. 5.13 except that the laser pulse has a multi-peak structure with a Gaussian envelope due to multi-reflections in the ethalon-air interfaces. The FWHM of the second order autocorrelation curve (envelope) is (6.5 ± 0.3) ps and thus the FWHM of the laser pulse is 4.6 ps.

Chapter 6

Summary, Applications and Prospects

In this work, we studied the effects which are appear when a fast and intense laser field interacts with metallic surfaces. The major phenomena that participate in the previous interaction are three. These are: the single- and multi-photon electron emission, the single- and multi-photon harmonic generation and finally the non-radiative decay of the excited electrons. The latter effect is connected with the thermal relaxation phenomena that take place on metallic surfaces which influence the harmonic generation and the photoemission.

6.1 Photoelectric Emission

High current electron beams up to several kA/cm^2 were produced when a metallic surface was illuminated by subpicosecond laser pulses. The metals were treated with a special way to produce a clean mirror-like metallic surface. Gold is inert with most of regants of air and the photocurrent density remained unchanged with the irradiation time. On the contrary, other metals like tungsten exhibited an irradiation time dependence of photocurrent and required about 90 minutes time in order to achieve the photocurrent saturation. The measurements of photocurrent from the metals were performed in the saturation area.

Photoemission takes place after multi-photon photon absorption by the surface electrons. This was proved by polarization measurements which showed the strong p-polarization dependence of the effect.

In the low laser intensity region, i.e., far for the intensity threshold of plasma creation, the photocurrent density depended on the n^{th} power of the laser intensity. Using various lasers the single-, second, third and fourth photoelectric emission from the gold surface was observed.

In the intensity region near the plasma creation threshold a positive deviation from the well known power low was observed. This deviation was attributed to thermionic emission for the case of normal heating, i.e., ns pulses, and to thermally assisted multi-photon photoemission due to high electron temperature produced by the subpicosecond laser pulses on the metallic surface (anomalous heating).

The photocurrent density value produced by the different orders of multiphoton photoemission was of the same order for subpicosecond laser pulse intensities of the order of a few GW/cm^2. An inversion of photoelectric sensitivities was observed when metallic surfaces are illuminated by subpicosecond laser pulses. These effects are not supported by the existing theories. A new theory [Geo95], of multiphoton photoelectric current densities for the low intensity region, that takes in account the electron-phonon momentum and energy relaxation phenomena, predicts current densities for the MPE that are in qualitative agreement with the experiment.

Tunneling electron emission is impossible to be observed by subpicosecond laser pulses because the required laser intensities are higher than the damage threshold and in any case the phenomenon is masked by the thermally assisted photoemission. The observed in the past negative deviation from the power low is attributed to the intense space-charge phenomena that appear in the high laser intensity region in which one has to work in order to observe field emission.

The photocurrent density was measured for various metallic photocathodes (Au, Cu, W, Al and Fe) illuminated by a laser pulse with duration 450 fs at 248 nm. The maximum single-photon photoelectric sensitivity was observed for Au and Cu. This may be attributed to different optical parameters of the various metallic surfaces as well as to different photoelectric emission cross-sections.

6.2 Harmonic Generation

Illuminating metallic surfaces with strong picosecond and subpicosecond laser pulses, we observed generation of both even and odd harmonics in the reflected direction. The intensity of the n-harmonic is proportional to the n^{th} power of the laser intensity. The observed decrease of the harmonic efficiencies with increasing the order of the harmonic was much weaker than predicted by perturbative theories. Two recent theories are used to partly explain our experimental results.

Multiple harmonic generation up to the fifth order was observed on a gold surface illuminated by the $\approx$ 35 ps Nd-YAG laser pulse at 1064 nm. The observed harmonics exhibit a strong p-polarization dependence on the incident laser field. The reflected harmonics were also p-polarized. Their efficiencies were between 10^{-10} for the second harmonic down to 10^{-13} for the fifth one.

Second and third harmonic was observed on gold surface illuminated by a 2 ps Nd-Glass laser at 1050 nm. The characteristics of the harmonic light are similar to these of the Nd-YAG laser case. It was shown that the harmonic efficiency is independent from the pressure in the vacuum cell in which the metal was kept. The second harmonic efficiency derived from copper and tungsten surfaces was measured. Gold was found to yield the higher second harmonic signal; three times higher than copper and more than one order of magnitude than W for a 1050 nm fundamental.

Second harmonic generation has been generated on a gold surface by means of a dye system capable of emitting pulses of 450 fs and 4.5 ps duration at a wavelength region between 490 to 520 nm. The laser intensity dependence of the second harmonic showed second order power law character; the form of polarization dependence followed the $\cos^4\phi$ law around the p-polarization direction. Wavelength tuning was possible for the second harmonic generation. The efficiency of the reflected second harmonic generation was higher in the case of 4.5 ps than at 450 fs in the intensity range of 0.1 to 20 GW/cm^2. The efficiency for second harmonic generation was found to depend strongly on the pulse duration of the laser beam. The observed change of the harmonic generation efficiency as a function of angle of incidence and pulse duration of the laser beam suggests that, due to coherence effects, the actual overlapping spatial dimension of the interaction region between the laser pulse and the electrons on the metallic surface plays an important role. Based on the detailed comparison of the obtained second harmonic efficiency value at various pulse durations and angles of incidence we concluded that for practical efficient harmonic generation from metallic surfaces one has to use short enough pulse duration to avoid plasma creation, but at the same time long enough pulses to have a sufficient coherent interaction area.

An unexpected non-linear enhancement in the efficiency of the second harmonic generation versus the laser intensity was observed, when the gold surface was illuminated by a powerful (few 10 GW/cm^2) subpicosecond excimer pumped dye laser at grazing incidence. The evidence of this effect was tested by time resolved autocorrelation measurements. This non-linearity is attributed to the thermal-nonequilibrium, between the electron gas and lattice temperatures, produced by the subpicosecond laser pulses on the metallic surface. The experimental results can be explained by a simple model of Fermi-Dirac distribution functions for various electron temperatures. The phenomenon is caused by the conduction electrons of the p-band of the gold metal. On the contrary, the interband transition from the top of d-band to the empty states around the Fermi energy in the conduction band produces a high electron temperature that affects the Fermi-Dirac distribution of the conduction-band electrons and consequently the harmonic generation efficiency. The latter effect was studied in details using energy-resolved experiments together with polarization or pump-probe experiments for various wavelengths of the laser beam. The polarization studies show that the harmonic generation is produced mainly by the conduction electrons. An asymmetric broadening of the spectrum of the second harmonic is observed in the low energy region of the spectrum at the high laser intensities; higher than 20 GW/cm^2. This may be caused by interband single-photon absorption which fills the empty states around the Fermi-level, as well as by relaxation of conduction electrons. This effects are not observed when the laser photon energy is smaller than the required for the interband transition on gold; i.e., 2.45 eV.

Second and third harmonic light is also generated on a gold surface by 100 fs Ti:sapphire laser pulses at 790 nm. Both show a strong p-polarization dependence. The nth-harmonic intensity is proportional to the n^{th} power of the laser intensity. The maximum laser intensity used in this case was 0.1 GW/cm^2. The harmonic generation efficiency was measured for various angles of incidence. The second harmonic generation efficiency was of the order of 10^{-11} to 10^{-10} depending on the angle of laser incidence according to second order non-linear Fresnel factors. The corresponding values for the third harmonic efficiency were about two orders of magnitude smaller. The spectrum of the second and third harmonic had the expected behavior for pure photodynamic non=-linear processes, contradicting to the case of dye laser where a broadening in the harmonic spectrum was observed. The reason for this difference may be the low intensity of the Ti:sapphire laser as well as its photon energy; 1.56 eV, which is much less than the interband transition threshold.

6.3 Relaxation Phenomena

In the case of laser pulse duration shorter than the electron-phonon energy relaxation time, namely a few picosecond or less, the electron temperature is initially much higher than the lattice temperature. There is no significant heating of the lattice as long as the laser intensity is typically lower than a few 10 GW/cm^2. From a microscopic stand-point, the energy in the light wave is transferred to the metal in the following sequence: photon energy is first transferred into electronic excitations, subsequently, these hot electrons come into thermal equilibrium with other electrons due to electron-electron scattering and finally the hot Fermi-Dirac electron gas comes in thermal equilibrium with the lattice due to electron-phonon collisions.

The electron energy relaxation time was measured via reflectivity thermomodulation measurements by other groups. In this thesis we used a new method based in the time-resolved single-photon non-linear photoelectric emission from metals. We are able to directly observe electron energy relaxation which is in the range of 0.5 to 2 ps for the tested polycrystalline metals, when irradiated by 450 fs, 248 nm laser pulses. Then a theoretical model fit to the experimental data and from the fitting parameters one can estimate the electron-phonon and electron-electron scattering relaxation time of the various metallic samples. The model is based on a coupled thermal equation for the electron gas and lattice subsystem. The electron-phonon collision rate depends on the lattice temperature. On the contrary, electron-electron collision rate depends on the square of the electron temperature and/or the available phase space between its energy and the occupied states near the Fermi energy. Then, the photocurrent density as a function of laser intensity is calculated by the Fowler-DuBrighe theory.

In the above model it is assumed that the electron-electron scattering time is much faster than the electron-phonon one, and consequently the electrons are very fast thermalized to a Fermi-Dirac distribution. This is not correct in any case since non-thermal electrons are generated in the initial times of excitation. For this reason we performed an analysis for the non-thermal electrons in copper using a Boltsmann-type equation. This analysis shows that for our experimental conditions it is not a good approximation to omit the non-thermal electrons.

6.4 Applications

As we have shown the results of interaction between lasers and metallic surfaces are electron and photons. In the next two subsections we discuss the use of the products.

6.4.1 Electrons

The production of pulsed, high current electron beams is one of the main requirements for the development of new electron accelerators, free electron lasers, x-ray sources and RF-linacs. At the same time Metallic photocathodes are valuable candidates, especially when irradiated by ultrashort laser pulses. They are suitable to work in ps and fs domains because the electron emission quantum efficiency increases non-linearly when the laser pulse intensities are higher than 0.1 GW/cm^2. Metals exhibit a high laser damage threshold in the femtosecond regime up to a few 100 GW/cm^2. They are capable of yielding peak current densities greater than a few 10 kA/cm^2 and hold up fields greater than 10^8 V/m without suffering electrical breakdown. Comparing with semiconductors the metals require minimum processing and emit electrons promptly with very low temporal spread over the irradiating laser pulse. In metals the delay for electron appearance in vacuum is only few femtoseconds.

A pulsed x-ray source was developed using a diode arrangement with an anode charged to 0 - 30 kV to draw off the photoelectrons emitted from a metallic photocathode. In a preliminary experiment the laser flux had been kept low enough to prevent plasma formation so that the resulting photon-electron pulse had about the same duration with the incident laser pulse. This excimer laser-driven photocathode is capable, as we showed, to produce electron currents densities of few 10 kA/cm^2. The resulting photoelectron pulse is accelerated onto a copper metallic anode yielding K_a emission at about 10 keV. The x-ray emission is investigated using filtered Si p-i-n diodes of a rise time of 5 ns.

6.4.2 Photons

The simultaneous emission of the second and third harmonic generation on a gold surface was used for the temporal characterization of a 100 fs Ti:Sapphire laser pulse and 450 fs excimer pumped dye laser system. For the first time a metallic surface was used in order to provide second and third order fast and slow autocorrelation functions for the amplitude, phase, temporal asymmetries and duration of pulsed laser electric fields. The continuous tunability of harmonic generation on metallic surfaces make their use favorable for U.V. laser pulses where dielectric doubling crystals are used, as well as for broadband laser systems where the continuous tunability is required. Finally, using exactly the same experimental set-up with only one non-linear medium the metallic surface, one can measure the various orders of autocorrelation functions as well as the spectrum of the fundamental and of the multi-harmonic lights.

As we have shown, the yield of harmonics followed the intensity of the fundamental laser beam for the different wavelengths of the tuning curve. These results show that one may effectively convert radiation from the visible to the UV and VUV wavelength regions, which might have practical importance from the point of view of UV and VUV laser spectroscopy.

6.5 Prospects

After the end of this work some questions remained with no clear answer and same new ones arise.

For example, what is the energy of the emitted photoelectrons from a metallic surface illuminated by high intensity femtosecond laser fields? Consequently is there ATI phenomena and/or non-thermal electrons? As we it was shown by Girardeau-Montaut et. al. [Gir89, Gir89a, Gir91], space charge effects affect the energy of the extracted electrons. A possible experimental set-up for measurements of photoelectron spectra should be free of electromagnetic fields. For example a special time of flight (TOF) spectrograph with magnetic and electric insulation system, which unfortunately was not available for our experiments. In fact, even for this type of spectrograph the space charge phenomena exist but one may do deconvolution of experimental data using numerical codes for space charge [Gir91] . A solution(?) may be to use lower laser intensities but at this case any ATI spectra might disappear.

Possible cut-off of the emitted harmonics from the metallic surfaces is still not answered. Cut-off phenomena have been observed in the harmonic generation from gaseous atoms. If E_{cutoff} is the cut-off energy, W_p the ionization potential of the material and U_p the pontero-motive potential of the light field, the cut-off energy can be expressed as:

$$E_{cutoff} = W_p + kU_p \tag{6.1}$$

where k is a constant range from 2 to 3.2. Analogous phenomena might be observed for the harmonic generation from metallic surfaces. For this purpose a fast and intense UV laser is required. The harmonics may be detected in a VUV monochromator. In the laser intensity range of a few GW/cm^2, for metals U_p is very small compared to W_p. Thus, one expects a cut-off of the harmonic at energy equal to W_p

Our experimental results on photoelectron emission and harmonic generation for laser intensities near the surface damage threshold show an influence of the high electron temperature in the yield of the phenomena as well as in the order of non-linearity. In the case of harmonic generation it is shown the generation of new wavelength, initially unexpected taking in account the spectral profile of fundamental. An experiment is in progress in order to measure the coherent and any incoherent component of the harmonics generated on a gold surface via quantum statistical analysis of the harmonic photons. Most the above effects are treated in this work by phenomenological models which contain the basic ideas for the physics below them. In any case, a detailed quantum mechanical optical theory is expected taking in account detailed phenomena as interband transitions, changes of the optical constants, non-thermal electrons, high electron temperatures, in order to provide further insight of these interesting phenomena.

New experiments must be perform in order to complete the characterization of the fast x-ray source produced by the ultra-short and high current electron pulses obtained when subpicosecond pulse illuminate metallic surfaces, i.e., conversion efficiency, pulse duration and angular distribution.

Finally, for the autocorrelator based on harmonic generation on metallic surfaces, the intention is to use this compact, low cost autocorrelator system as an on line laser beam diagnostic for ultrashort laser pulses.

Bibliography

[Abe72] Abeles F., *Optical Properties of Solids*, North-Holland Publishing Company-Amsterdam, London (1972) pp. 109-110

[Ago68] Agostini P., Barjot P., Bonnal G., Mainfray J. F., and Manus C., *IEEE J. Quant. Electr.* **QE-4**, 667 (1968)

[Agr79-80] Agranat et al., *JEPT Lett.* **30**, 168 (1979); *Sov. Phys. JEPT* **52**, 27 (1980)

[Alg87] Algatti M. A., Farkas Gy., Toth Cs., *Internal report of Central Institute for Physics*, **KFKI-1987-66/D.E.F.**, (1987)

[All66] Allen F. G., Gobeli G. W., *Phys. Rev.* **144**, b65, (1966) and references therein

[All87] Allen P. B., *Phys. Rev. Lett.* **59**, 1460, (1987)

[Ani74] Anisimov S. I., Kapeliovich B. L., and Perelman T. L., *Sov. Phys. JEPT* **39**, 375 (1974).

[Ani77] Anisimov S. I., Benderskii V. A., Farkas G., *Sov. Phys. Usp.* **20**, 467 (1977)

[Arm67] Armostrong J. A., *Appl. Phys. Lett.*, **10**, 16 (1967)

[Ash76] Ashcroft N. and Mermin C, *Solid State Physics*, Saunders Philadelphia (1976), (Chap. 2)

[Ash76a] Ashcroft N. and Mermin C, *Solid State Physics*, Saunders Philadelphia (1976), pp. 523-528

[Ashb76] Ashcroft N. and Mermin C, *Solid State Physics*, Saunders Philadelphia (1976), (Chap. 1)

[Ash76c] Ashcroft N. and Mermin C, *Solid State Physics*, Saunders Philadelphia (1976), pp. 346-351

[Ashn76] Ashcroft N. and Mermin C, *Solid State Physics*, Saunders Philadelphia (1976), pp. 323-324

[Bau77] Bauman Z., *IEEE J. Quant. Electr.* **QE-13**, 875 (1977)

[Bec75] Bechtel J. H., *J. Appl. Phys.* **1585**, (1975)

[Blo65] Bloembergen N., *Nonlinear Optics*, Benjamin, New York, (1965)

[Blo66] Bloembergen N., Chang R. K., Lee C. H., *Phys. Rev. Lett.* **16**, 986, (1966)

[Blo68] Bloembergen N., Chang R. K., Jha S. S., and Lee C. H., *Phys. Rev.* **174**, 813 (1968)

[Bow76] Bower J. R., *Phys. Rev. B* **14**, 2427, (1976)

[Bra74] Bradley D. J., Geofrey H., and New C., *Proceedings of the IEEE* **62**, 313 (1974)

[Bro65] Brown F., Parks R. E., Sleeper A. M., *Phys. Rev. Lett.* **14**, 1029 (1965)

[Bro66] Brown F. and Parks R. E., *Phys. Rev. Lett.* **16**, 507, (1966)

[Bro87] Bronson S. D., Fujimoto J. G., and Ippen E. P., *Phys. Rev. Lett.* **59**, 1962 (1987)

[Brod77] Brodsky A. M., *Phys. Stat. Sol. b* **83**, 331 (1977)

[Bru91] A. Brun, P. Georges, G. Le Saux, and F. Salin, J. Phys. D **24**, 1225, (1991)

[Bun65] Bunkin F. V., and Fedorov M. V., *Sov. Phys. JEPT* **21**, 896 (1965)

[Bur70] Burnaham D. C., *Appl. Phys. Lett.* **17**, 45 (1970)

[Bur71] Burns W. K., Bloembergen N., *Phys. Rev. B* **4**, 3437 (1971)

[Car69] Cardona M., *Modulation Spectroscopy* Academic, New York, (1969) (chap.5)

[Crc88] *CRC Handbook of Chemistry and Physics*, 69th edition, CRC Press, Inc. Boca Raton, Florida, (1988-1989)

[Dah71] Dahlstrom L., and Kallberg B., *Opt. Comm.* **4**, 285 (1971)

[Dan92] Daniele R., Ferrante G., Fiordilino E. and S. Varro, *J. Opt. Soc. Am.* **B9**, 1916, (1992)

[Die85] Diels J. C. M., Fontain J. J., McMichael I C., and Simoni F., *Appl. Opt.* **24**, 1270 (1984)

[Dub33] DuBridge L. A., *Phys. Rev.* **43**, 727 (1993)

[Ebe78] *Multiphoton Processes*, Eds. J. H. Eberly and P. Lambropoulos (Wiley, New York) (1978)

[Ees83] Eesley G. L., *Phys. Rev. Lett.* **51**, 2140, (1983)

[Ees86] Eesley G. L., *Phys. Rev. B* **33**, 2144 (1986)

[Els87] Elsayed-Ali H. E., Norris T. B., Pessot M. A., and Mourou G. A., *Phys. Rev. Lett.* **58**, 1212 (1987)

[Els91] Elsayed-Ali H. E., Juhasz T., Smith G. O., and Bron W. E., *Phys. Rev. B* **43**, 4418 (1991)

[Fan92] Fann W. S., Storz R., Tom H. W. K. and Bokor J., *Phys. Rev. B* **46**, 13592, (1992)

[Fan92a] Fann W. S., Stortz R., Tom H. W. K., and Bokor J., *Phys. Rev. Lett.* **68**, 2834 (1992)

[Far67] Farkas Gy., Naray Z. S., Varga P., *Phys. Rev. A* **24**, 134 (1967)

[Far72] Farkas Gy., Horvath Z. G., Kerstez I., *Phys. Lett.* **A39**, 231, (1972)

[Far74] Farkas Gy., and Horvath Z. G., *Opt. Comm.* **12**, 392 (1974)

[Far90] Farkas Gy., and Toth Cs., *Phys. Rev. A* **41**, 4123 (1990)

[Far92] Farkas Cy., Toth Cs., Moustaizis S. D., Papadogiannis N. A., and Fotakis C., *Phys. Rev. A.* **46**, R3605 (1992)

[Far94] Farkas Gy., Toth Cs., Kroo N., LeBlanc S. P., Zeng-Fen Q, Sanebrey R., and Tittel F. K., *5th European Quantum Electronic Conference (EQEC'94)* Proceedings, Amsterdam, The Netherland 28 August-2 Semptember 1994, paper QThG16 (IEEE catalog No. 94TH0615-5)

[Fer88] Ferray M., L'Huillier A., Li X. F., Lompre L. A., Mainfray G., and Manus C., *J. Phys. B* **21**, L31 (1988)

[Fow31] Fowler H., *Phys. Rev.* **38**, 45 (1931)

[Fuj84] Fujimoto J. G., Liu J. M., Ippen E. P., and Bloembergen N., *Phys. Rev. Lett.* **53**, 1837 (1984)

[Geo95] Georges A. T., *Phys. Rev. B* **51**, 13735 (1995)

[Geo96] Georges A. T., *Phys. Rev. A* **54**, (September issue) (1996)

[Gio67] Giordamaine J. A., Rentzepis P. M., Shapiro S. L., and Wecht K. W., *Appl. Phys. Lett.* **11**, 216 (1967)

[Gir89] Girardeau-Montaut J. P., Girardeau-Montaut C., *J. Appl. Phys.* **65**, 2889 (1989)

[Gir89a] Girardeau-Montaut C., Girardea-Montaut J. P., and Leboutet H., *Appl. Phys. Lett.* **55**, 2556 (1989)

[Gir91] C. Girardeau-Montaut and J. P. Girardeau-Montaut, *Phys. Rev. A* **44**, 1409 (1991)

[Gir93] Girardeau-Montaut J. P., Girardeau-Montaut C., Moustaizis S. D., Fotakis C., *Appl. Phys. Lett.* **62**, 426 (1993)

[Gir93a] Girardeau-Montaut J. P., Girardeau-Montaut C., Moustaizis S. D., and Fotakis C., *Appl. Phys. Lett.* **63**, 699 (1993)

[Gir94] Girardeau-Montaut J. P., Girardeau-Montaut C., and Moustaizis S. D., *J. Phys. D: Appl. Phys.* **27**, 848 (1994)

[Gir95] Girardeau-Montaut J. P. and Girardeau-Montaut C., *Phys. Rev. B* **51**, 13560 (1995)

[Gir96] Girardeau-Montaut J. P., Afif M., Moustaizis S. D., and Papadogiannis N. A, *Appl. Phys. A* **62**, 3, (199

[Gui91] Guifand Li, Seshardi S. R., *Phys. Rev. B* **44**, 1240 (1991)

[Har80] Harisson W. A., *Electronic Structure and Properties of Solids*, Freeman W. H. and Company, San-Francisco (1980)

[Hui91] L'Huillier A. L., Schafer K. J., Kulander K. C., *J. Mod. Opt.* **24**, 3315 (1991)

[Hui93] A. L.'Huillier and Ph. Balcou, *Phys. Rev. Lett.* **70**, 774 (1993)

[Jac75] Jackson J. D., *Classical Electrodynamics*, McGraw-Hill, New York (1975) 2nd ed. p.379

[Jha65] Jha S. S., *Phys. Rev. Lett.* **15**, 412 (1965)

[Jha65a] Jha S. S., *Phys. Rev. B* **140**, A2020 (1965)

[Jha66] Jha S. S., *Phys. Rev.* **145**, 500 (1966))

[Kag57] Kaganov M. I., Lifshitz I. M., and Tanatarov L. V., *Sov. Phys. JEPT* **4**, 173 (1957)

[Kan94] D. J. Kane A. J. Taylor, R. Trebino, and K. D. Delong, Opt. Lett. **19**, 1061 (1994)

[Kav84] Kaveh M., and Wiser N., *Adv. Phys.* **33**, 259, (1984)

[Kav95] V. Kavelka and A. V. Masalov Opt. Lett. **20**, 1301, (1995)

[Kel65] Keldysh F. V., *Sov. Phys. JEPT* **20**, 1307, (1965)

[Kel91] U. Keller et al., Opt. Lett. **16**, 1022 (1991).

[Kop95] Rik H. J. Kop and Rudolf Sprik, Rev. Sci. Instrum. **66**, 5459 (1995)

[Kre71] Kretschmann E., *Z. Phys.* **241**, 313 (1971)

[Lam72] Lambropoulos P., *Phys. Rev. Lett.* **28**, 585 (1972)

[Lam84] Lambropoulos P.and S. J. Smith *Multiphoton Processes*, Springer-Verlag, Berlin (1984)

[Lam87] Lambropoulos P., *Comments At. Mol. Phys.* **20**, 199 (1987)

[Lom90] Lompre L. A., L'Huillier A., Ferray M., Monot P., Mainfray G., Manus C., *J. Opt. Soc. Am.* **B7**, 754 (1990)

[Lor91] Lorincz A., Bozoki Z. and Miklos A., *J. Appl. Phys.* **70**, 941 (1991)

[Lu94] Lu Y. F., Takai M., Komuro S., Shiokawa T., and Aoyagi Y., *Appl. Phys. A* **59**, 281, (1994)

[Lug94] Lugoskoy A. V., Usmanov T., and Zinoviev A. V., *J. Phys. D: Appl. Phys.* **27**, 628 (1994)

[Mac67] MacMillan W. L., *Phys. Rev.* **133** (1967)

[Mac80] MacDonald A. H., *Phys. Rev. Lett.* **44**, 489 (1980)

[Mai66] Maier M., Kaiser W., and Giordamaine J. A., *Phys. Rev. Lett.* **17**, 1275 (1966)

[Mak51] Makinson R. E. B., Buckingham M. J., *Proc. Phys. Soc. London* Sect. **A 64**, 135 (1951)

[Mat75] J. P. Mathieu, *Optics* Pergamon Press, Oxford (1975)

[Mik88] Miklos A., and Lorintz A., *J. Appl. Phys.* **63**, 2391 (1988)

[Mis91] Mishra A., Gersten J. I., *Phys. Rev. B* **43**, 1883, (1991)

[Mit36] Mitchell K., *Proc. Roy. Soc. London* **A146**, 442 (1934) and **A153**, 513 (1936)

[Mou95] Moustaizis S. D., Papadogiannis N. A., Fotakis C., Farkas C., Toth. C., *Appl. Phys. Lett.* **67**, 3239 (1995)

[Nag89] K. Naganuma, K. Mogi and H. Yamada, Appl. Phys. Lett. **54**, 1201, (1989)

[Orl95] Orlande H.-R., Ozicik M. N., and Tzou D. Y., *J. Appl. Phys.* **78**, 1843 (1995)

[Pal85] *Hanbook of Optical Constants of Solids*, edited by E. D. Palik, Academic Press, Orlando Florida, (1985)

[Pap96] N. A. Papadogiannis, S. D. Moustaizis and C. Fotakis, Submitted for publication (1996)

[Ray82] Rayner D. M., Hackett P. A., and Willis C., *Rev. Sci. Instr.* **53**, 537 (1982)

[Rea65] Ready J. F., *Phys. Rev.* **A620**, (1965) [Rog90] Rongier H. M. Groenveld, Rudolf Sprik, and Ad Lagendijk, *Phys. Rev. Lett.* **64**, 784 (1990)

[Ros72] Rosei R. and Lynch D. W., *Phys. Rev. B* **5**, 3883 (1972)

[Ros73] Rosei R., Antonangeli F., and Grassano U. M., *Surf. Scien.* **689** (1973)

[Ros74] Rosei R., Culp C. H., and Weaver J. H. *Phys. Rev. B* **10**, 484 (1974)

[Sac89] Sacks R. A., and Szoke A., *Phys. Rev. A* **40**, 5614 (1989)

[Sac91] Sacks R. A., and Szoke A., *J. Opt. Soc. Am. B* **8**, 1987 (1991)

[Sal80] Sala K. L., Kenney-Wallace G. A., and Hall G. E., *IEEE J. Quant. Electr.* **QE-16**, 990 (1980)

[Sch87] Schoenlein R. W., Lin W. Z., Fujimoto J. G., and Eesley G. L., *Phys. Rev. Lett.* **58**, 1680 (1987)

[Sco67] Scouler W. L., *Phys. Rev. Lett.* **18**, 445 (1967)

[She84] Shen Y. R., *The Principles of Nonlinear Optics*, John Willey and Sons, New York (1984)

[She89] Sherman N. K., Brunel F., Corkum P. B., and Hegmann F. A., *Opt. Eng.* **28**, 1114 (1989)

[Sil71] Silin A. P., *Sov. Phys.-Sol.Stat.* **12**, 2886 (1971)

[Smi62] Smith R., *Phys. Rev.* **128**, 2225 (1962)

[Smi71] Smith N. V., *Phys. Rev. B* **3**, 1862 (1971)

[Son79] Sonnerberg H., and Heffner H., *J. Opt. Soc. Am.* **69**, 116, (1979)

[Spe91] D. E. Spence, P. N. Kean, and W. Sibbet, Opt. Lett. **16**, 32 (1991).

[Spi72] Spicer W. E., *Optical Properties of Solids*, edited by Abeles F., North-Holland Publishing Company-Amsterdam, London (1972) pp. 796-801

[Spi72a] Spicer W. E., *Optical Properties of Solids*, edited by Abeles F., North-Holland Publishing Company-Amsterdam, London (1972) pp. 791-795

[Spi72b] Spicer W. E., *Optical Properties of Solids*, edited by Abeles F., North-Holland Publishing Company-Amsterdam, London (1972) p. 775

[Spi95] Spielmann Ch., Lenzuer M., Krausz F., Szipocs R., and Ferencz K., *Laser Focus World* December (1995) p.55

[Sri91] Srinivasan-Rao T., Fisher J. and Tsang T., *J. Appl. Phys.* **69**, 3291 (1991)

[Sun93] Sun C. K., Vallee F., Acioli L., Ippen E. P., and Fujimoto J., *Phys. Rev. B* **48**, 12365 (1993)

[Sun94] Sun C. K., Vallee F., Acioli L., Ippen E. P., and Fujimoto J., *Phys. Rev. B* **50**, 15337 (1994)

[Sza88] Szatmari S., and Schafer F. P. *Appl. Phys. B* **46**, 305 (1988)

[Tei64] Teich M. C., Schroeer J. M., and Wolga G. J., *Phys. Rev. Lett.* **13**, 611 (1964)

[Tre90] R. Trebino, C. Hayden, A. M. Johnson, W. M. Simpson, and A. M. Levine, Opt. Lett. **15**, 1079 (1990)

[Tre93] R. Trebino and D. J. Kane, J. Opt. Soc. Am. A **10**, 1011 (1993)

[Urb92] Urbach L. E., Percival K. L., Hicks J. M., Plummer E. W., and Dai H.-L., *Phys. Rev. B* **45**, 3769, (1992)

[Var94] Varro S., Ehlotzky F., *Phys. Rev. A* **49**, 3106 (1994)

[Vor66] Voronov Cs., and Delone N. B., *Sov. Phys. JEPT* **23**, 54 (1966)

[Wan94] Wang X. Y., Riffe D. M., Lee Y.-L., and Downer M. C., *Phys. Rev. B* **50**, 8016 (1994)

[Yen80] Yen R., Liu J., and Bloembergen N., *Opt. Comm.* **35**, 277 (1980)

[Yen82] Yen R., Liu J., Bloembergen N., Yee J. K., Fujimoto J. G. and Salour M. M. *Appl. Phys. Lett.* **40**, 185, (1982)